The development of an electric-powered subsea robotic crawler for dredging.

by

Mike Oluwaseun Ojumu

Thesis submitted in fulfillment of the requirement for the Degree

Master of Engineering: Mechanical Engineering

In the Faculty of Engineering and the Built Environment at the Cape Peninsula University of Technology.

Supervisor: A/Prof Atanda Kamoru Raji.

Co-supervisor: A/Prof. Oscar Philander.

Bellville campus

October 2022

DECLARATION

I**, MIKE OLUWASEUN OJUMU**, declare that the contents of this dissertation/thesis represent own unaided work, and the dissertation/thesis has not previously been submitted for academic examination towards any qualification. Furthermore, it represents my own opinions and not necessarily those of the Cape Peninsula University of Technology.

04/10/2022

Signed **Date**

ABSTRACTS

The current rising global demand for ocean based recoverable minerals and natural resources is inspiring research and growing interests in the field of ocean dredging. However, current hydraulic powered dredging crawlers are prone to causing ocean pollution as a result of hydraulic leakages, heavy vibrations and noise. These underwater crawlers also consume relatively high power because of their mass. Hence, in this thesis we have modelled, designed, and manufactured a scaled-down electric powered subsea robotic crawler for underwater mining/dredging applications. The prototype is designed to compete with a scaled-down version of a real-world hydraulic powered Remotely Operated Subsea Tractor MK3 (ROST). This research also highlights the possibilities of eliminating sea pollution caused by hydraulic leakages in hydraulic-powered subsea crawlers by replacing them with electric powered ones. Furthermore, this research shows that electric powered crawlers will be lighter than hydraulic powered equivalents; hence, they will consume less energy during operation.

A detailed literature review based on related research was first carried out to identify and outline the key characteristics of subsea crawlers/tractors, such as their operating principles, mechanisms, and structural design parameters. Afterward, the scaled-down prototype was modelled and assembled to meet the scaled-down basic specifications of the ROST MK3. The model comprises of a robot-driving base, a 2DOF robotic arm with nozzles at the end effector, and 2 pumps for loosening and dredging the seafloor respectively. Two DC motors connected to tank-tread chain links were used to propel the driving base as a differential drive robot. The control system was implemented using LabVIEW programming language to create a Graphical User Interface for various controls. To choose the right material for designing this model, a FEA simulation will be performed on different material. Additionally, the capacity of the forces operating on the model's structural elements will be ascertained through this simulation. The prototype is electrically powered by a 12V Nickel Metal Hydride battery with a 3000mah capacity. The NI-myRIO is used as the main microprocessor to control and interact with the necessary DC motors, servo motors, cameras, pumps, lights, and sensors.

The prototype underwent land testing at the Adaptronics Advanced Manufacturing Technology Laboratory (AMTL). The drive characteristics (torque, velocity, and efficiency) of the model were tested at different angles of inclined planes which includes: 0^0, 15^0, 20^0 25^0 and 30^0.

This research will further contribute to an alternative method of extraction using an electric powered robotic subsea crawler for ocean dredging and other applications. The crawler will be assembled and programmed to improve the quality and capabilities of its mode of operation under different ocean floor

conditions, and finally, it will create a solution to the limitations of current hydraulic dredging crawler technology and a new approach to the utilization of robotic subsea crawlers for different applications.

KEYWORDS: Subsea Tractor, Subsea crawler, remotely operated, hydraulic powered, electric powered, mining dredging, angle of inclination, driving system, controllers, and user interface.

I want to thank:

- My parents and family, for their relentless support towards the success of my educational pursuits and career.

- To my supervisor A/Prof Oscar Philander, I say a very big thank you for your patience, absolute support, and mentorship during this research.

- To my co-supervisor A/Prof. Atanda Kamoru Raji, I say a very big thank you for your kind support, continuous follow-ups and, assistance towards this research.

- To Mr. Inyeni Amakuro Showers, I say thank you for your encouragement, I deeply appreciate you.

Thanks to Cape Peninsula University of Technology, for their bursary scholarship as financial assistance towards my master's program. I would also love to appreciate the Adaptronics Advanced Manufacturing Technology Laboratory (AMTL), for providing the research funding and equipment for building the physical scaled-down model for this research. Opinions expressed in this thesis and the conclusions arrived at, are those of the authors; however, they are not necessarily to be attributed to the National Research Foundation.

DEDICATION

This work is dedicated to the almighty God who is the custodian of wisdom, knowledge, understanding, and inspiration.

TABLE OF CONTENTS

TABLE OF FIGURES

LIST OF TABLES

GLOSSARY

Abbreviations	Definitions
EPRSDC	Electric Powered Robotic Subsea Dredging Crawler.
ASV	Automotive Sea vehicles
AMTL	Adaptronics Advance Manufacturing Technology Laboratory
SC	Subsea Crawler
GUI	Graphical User Interface
AUV	Autonomous Underwater Vehicle
UUV	Unmanned Underwater Vehicle
SDE	Seabed Dredger Excavator
ROV	Remote Operated Vehicle
DC	Direct Current
AC	Alternating Current
MCU	Motor Controller Unit
PSC	Power Supply Centre
kW	Kilowatt
W	Watts
PTs	Potential Transformers
CTs	Current Transformers
PIDC	Proportional-Integral-Derivative Controller
API	Application programming Interface
CPU	Control Processing Units
NiMH	Nickel Metal Hydride
LT	Ladder Tendier
PDTS	Post-Detection Telemetry Subsystem
LVDT	Linear Variable Differential Transformer
RTD	Resistance Temperature Detectors
LPDV	Load Pressure Distribution Valve
SCFU	Subsea Crushing Feeding Unit
HMS	Horizontal Mining System
VMS	Vertical Mining Systems

DTHD	Down-The-Hold drill
PWM	Pulse Width Modulation
USBL	Ultra-Short Base Line
EKF	Extended Kalman Filter
EPPRV	Electro-Proportional Pressure Reducing Valves
NFC	Negative Flow Control
SVWDP	Speed-Variable Witched Differential Pumps
SR	Switched Reluctance
MBD	Multi-Body Dynamic
TMS	Tether Management System
HCFDV	Hybrid Crawler-Flyer Underwater Vehicle
FLC	Fuzzy Logic Controllers
VB	Visual Basic
CCU	Control Command Unit
CU	Controller Unit
NiMH	Nickel Metal Hydride
USV	Unmanned Surface Vehicles
GA	Genetic Algorithms
HCA	Hill-Climbing Algorithms
AC	Auxiliary Cutter
BC	Bulk Cutter
CM	Collection Machine
EPA	Environmental Protection Agency
NPL	National Priorities List

CHAPTER ONE: INTRODUCTION

This chapter presents the problem statement, aim, and objectives of this thesis. Furthermore, the background of the research problem is discussed. To provide more details, the concept of the electric-powered robotic subsea dredging crawler is presented. Some contemporary challenges regarding the hydraulic system in ocean extraction are also mentioned. After which some anticipated applications of the EPRSDC for mining systems are stated and discussed, along with the delineation, significance, and contribution of the research.

1.1 Problem Statement

Ocean-crawling extractors' are best known for their unpredictable operational failures, which contribute to hydraulic oil pollution in the ocean mining sector. This research covers the development of an electric-powered Remote Operated Subsea Tractor (ROST), which is also known as an Autonomous Underwater Vehicle (AUV), Unmanned Underwater Vehicle (UUV), Remote Operated Vehicle (ROV), or Seabed Dredger Excavator (SBDE). The above-mentioned vehicle is designed to function on the floor of a body of water. It is classified as a wired, remotely operated vehicle because it is tethered. This class of vehicles are increasingly being used in operations such as ocean dredging, ocean inspection, ocean data collection, ocean photography, as well as oil pipeline laying. This is because they are more environmentally friendly compared to their hydraulic-powered counterparts. They are also more suitable for rapid natural extraction of natural resources in both small and large-scale mines. Recent research on this subject has been focused on the protection of ocean environments while extracting natural resources from the ocean floor. Electric-powered ROSTs are typically lighter than their hydraulic counterparts, hence they utilize less power for their basic operations.

Electronic components such as DC/AC electric motors, servo motors, and microcontrollers have greatly reduced the complexity involved in designing and controlling electrical equipment. In the future, as more designs and programs are developed for heavy duty mining operations, there will be greater demand for environmentally friendly equipment, for both land and sea applications. The (AMTL), and the Technology Innovation Agency (TIA), located at the Cape Peninsula University of Technology, are making remarkable efforts at developing a small-scale prototype of the electric-powered ROST. This robotic crawler is projected to have the following features: offshore dredging capabilities, autonomous navigation, obstacle evasion, sub-crawlers with ROV landings, a self-extractor, and advanced positioning systems. These features were selected to make the crawler and robust, flexible for offshore extraction operations.

(IMDH Group, 2016), and (technology, 2018) currently make use of hydraulic tractor MK3 ROST for their ocean floor extraction activities and research-based projects. Although this vehicle has been successfully used for many years in ocean intervention for dredging and mining operations, it has certain notable limitations. These limitations include hydraulic ocean pollution and high-energy consumption because of its large mass. These limitations can be reduced by substituting hydraulic-powered ocean crawlers with electric-powered ones. Some details of the problems associated with hydraulic-powered crawlers are as follows:

1.1.1 Hydraulic Ocean Pollution

(Roman Mikhailiuk et al., 2021) stated that ocean pollution is caused by the introduction of toxic materials and harmful pollutants such as agricultural and industrial waste, chemicals, oil spills, and plastic litter into the ocean water. Sea pollution can occur in different ways, which include vibrations and noise caused by hydraulic excavation at sea, hydraulic fluid leakages, hydraulic pipe explosions, hydraulic cylinder leakages, and hydraulic pump malfunctions.

Figure 1.1: harmful materials to the ocean (Roman Mikhailiuk et al., 2021)

As shown in figure 1.1, Hydraulic Ocean pollution occurs when hydraulic fluid is introduced to the ocean. Hydraulic fluid is a mineral oil made of dewaxed paraffin-based crude oils that are blended with additives to formulate an appropriate compound for the specific use (Newton 199; papay 1989, 1991; Wills 1980). Dewaxed paraffin oil is gotten from separation of wax from base oil, and it is chemically harmful to ocean aquatic creatures.

Figure 1.2: hydraulic workover rig expulsion (Toyin Akinosho & Africa oil +gas, 2020)

Figure 1.2 shows the explosion caused by the hydraulic work over rig Grace-1 HWU as reported by (Toyin Akinosho & Africa oil +gas, 2020) on May 6, 2020. This working rig was reported to be in operation for the Nigerian Independent Guarantee Petroleum when it burst into flames over the weekend during a re-entry operation on the Ororo-1 well in shallow water Oil Mining Lease (OML) 95. It was reported that the technicians had put the well under control, after it had released hydraulic fluid to the surface through a malfunctioned Blowout Preventer (BOP) on the rig, owned by Jo Eny Holdings Limited. "While the system was stable, the pressure of the gas leak was at the same level with the BOP which was closed-in, thus causing the explosion."

Figure 1.3: hydraulic leakage fire explosion (CNN Correspondent Mary, 2010)

Figure 1.3 shows (CNN Correspondent Mary, 2010) who narrated the catastrophic explosion on the Deepwater Horizons. She reported that the control unit's blowout preventer was already leaking hydraulic fluid before the fire. It is also said that this explosion unleashed the worst oil pollution on ocean in U.S history. This incident was investigated by Ronald Sepluvado, who was one of the site leaders' company men in the rig jargon. He stated that there were "on and off" problems with hydraulic valves that directed hydraulic fluid inside the mechanism.

Roger Billingham - Deputy Chief Inspector of Mines (Metal) (Roger Billingham & Department of Natural Resources, 2004) also talked about high-pressure hydraulic hoses which are subject to flexing and exposure to mechanical damage. A hose failure can result in hydraulic oil being sprayed around the machine, creating a fire risk and in some cases an explosion risk. Hotspots such as the turbo chargers on diesel engines can ignite hydrocarbons, increasing the likelihood of a fire and/or explosion occurring. A few major fires have occurred on excavators while the machines were operating.

1.1.2 Power/Energy consumption by the hydraulic powered subsea crawlers

Dredging ocean crawlers are heavy-duty machines that utilize many high-power consuming components. (Poomphochana et al., 2013) discussed the hydraulic power consumption of propelled machines. Hydraulic systems waste much of their power when the fluid circulates at a constant pressure, regardless of the amount of work carried out. In engineering management design, the higher the consumption of power, the higher the maintenance cost. The higher the number of parts used for building and designing a machine, the higher the production cost, and the greater the time taken to maintain the machine. This crawler is said to operate with a high-power consumption due to its numerous drive systems. The MK3 ROST has a dredging pump of 2.4 MW power, a 500kW hydraulic power pack, and a 500kW jet-water system. All these multi-functional parts are driven by a generator and converter in order to deliver sufficient power for the crawler's performance.

The International Maritime Organization (IMO) regulatory bodies and authorities are putting a lot of efforts in up scaling their laws to ensure that offshore mining is done in the right way, to reduce ocean pollution. Considering their law, it is evident that smart crawlers with artificial intelligence will be the new normal in the nearing future. (Minerals and Energy Laws Amendment Act, 2013) analysed and discussed the mineral petroleum resources development and are setting out laws that regulate the mine ACT NO. 28 OF 2002. These laws are to regulate the effects of heavy-duty machines in the human environment that are used for extractions. Some of these laws are based on noise pollution, ocean pollution, and the destruction of the seabed due to the heaviness of this equipment. They are imposing both ocean and inland mines to

develop a remote-control system for mining equipment, control and use equipment that stop or reduce the rate of vibration in the mine industries. With these developments, It is foreseeable that in the future, robotic electronic systems will be fully adapted into subsea mining operations as they have many features that protect the environment. These robots will largely reduce noise pollution to the ocean environment, and they can be operated using electronic systems with simple user interfaces. Moreover, they seem to be ocean friendly and have no significant negative impact on the seabed. This project being carried out at AMTL is focused on building a crawler that eliminates hydraulic ocean pollution and reduces power consumption. When fully develop, this technology could reduce the production costs of ocean dredging machines, while still performing its specific task at relatively affordable maintenance costs.

1.2 Aims of this research

1. To develop a scaled-down model of an electric powered robotic subsea crawler with similar characteristics and specifications to the MK3 ROST hydraulic dredging crawler.

2. To determine the characteristics and specifications of the scaled-down model of the electric robotic subsea crawler.

3. To scale-up the characteristics and specifications of the model and compare to MK3 ROST hydraulic dredging crawler.

4. To determine if the scaled-up model of the electric powered robotic crawler could reduce sea pollution and power consumption for ocean mining applications.

1.3 Objectives of this research

The primary objective of this research is to develop a scaled-down concept of an electric-powered robotics subsea dredging crawler for ocean mining and exploration. In this case, the MK 3 ROST hydraulic crawler was used as a research study making sure that our scaled-down model is able to compete with the hydraulic MK 3 ROST. In order to achieve this primary objective, sub-objectives were formulated and presented below: Design and build a model of an electric-powered subsea robotic crawler for dredging applications.

1. To investigate through a literature review of current hydraulic crawlers, application of ocean dredging crawlers, their dynamic driving system, and inverse kinematics dredging arms.
2. To design and model the electric-powered robotics crawler using the SOLIDWORKS student version.

3. To manufacture and build a model of an electric-powered subsea robotic crawler for dredging applications.
    i. Identifying necessary hardware components for developing the robot framework, dynamic drive system, and robotic arm.
    ii. Using an engineering system in modelling the concept for applicability and integration into the crawler frame by assembling individual components.
    iii. Developing the required robot dredging arm and integrating it into the dredging pump.
4. To develop a software algorithm using LABVIEW to implement the following:
    i. To develop a human interface control system for our crawler.
    ii. Developing a driving algorithm for forward and backward driving systems, clockwise and contraclockwise directional movement.
    iii. To develop a program algorithm for the dredging arm inverse kinematics.
    iv. To develop a controller platform that identifies all control systems which includes the camera view system, pump control switch, light switch, motor controller, and servo motor controller.
5. Develop a ramp for the practical experiment of the crawler's climbing inclination.
    i. Estimated driving length distance 1.8 meters and width of 0.6 meters
    ii. Inclinational ramps angles of inclination: 0^0, 15^0, 20^0, 25^0, 30^0
    iii. SOLIDWORKS design using engineering mathematical modelling
    iv. Manufacturing and ramp testing of different angular inclination
6. To develop a practical concept to demonstrate the crawler's climbing inclination for five different angles such as
    i. Maximum velocity versus different angles of inclination
    ii. Torque versus velocity at 0^0 angle of inclination
    iii. Torque versus velocity at 20^0 angle of inclination
    iv. Minimum Torque versus different angles of inclination
    v. Efficiency versus torque at 0^0 and Efficiency versus torque at 20^0
    vi. To develop a software platform using python to graphically discuss the tabulated results and formulas.
7. To develop a 3-Dimensional solid model frame of the scaled-down electric-powered robotic subsea crawler using the SOLIDWORKS2020 academic version.
    i. To determine if 1050 aircraft-grade aluminium can be used for developing future robotic dredging crawlers
    ii. Using finite element analysis to demonstrate a simulated compressional test.

8. Develop tabulated characteristics and specifications of the electric subsea crawler model.
9. Develop a scaled-up model concept of an electric-powered robotic subsea crawler that is comparable with the MK3 ROST, which will be used for recommendation.

1.4 Background of research problem

A subsea ocean dredging crawler is an exploration and recovery machine. As seen in figure 1.4 below, it is designed to sink to the bottom of a body of water, mostly used in deep-sea exploration (mining), where it moves about using traction against the bottom of the seabed with wheels or tracks. It is usually tethered to a surface ship by cables providing power, control, video, and lifting capabilities, which enable its effective function. Extraction in the mining industry is the procedure of excavation and recuperation of minerals and associated waste rocks called undersea gravels. These undersea gravels are a long-time composition of complex mixtures of 96.5 percent water, 2.5 percent salts, and a smaller number of other substances including dissolved inorganic and organic materials, particulates, and a few atmospheric gases.

Figure 1.4: MK3 ROST Ocean dredging crawler under operation (IMDH Group, 2016)

As shown in figure 1.4, Ocean dredgers have become one of the most fast-growing offshore excavation tools in the world (De Beer Group, 2017). (IMDH Group, 2016) stated that there is a remarkable rise in the demand for metals which is stimulating interests in deep-sea exploration and commercial mining. Dredging crawlers are finding useful applications not just in the mining environments, but also in other applications like tank cleaning operations, pipeline inspections and firefighting. Furthermore, it can be used for watering agricultural farms, subsea photography, pipeline support and many other applications. (Lloyd-Smith & Immig BAppSc, 2018) analyzed a concept design of a dredging robot with a small vacuum

head which interacted with a seabed. It has a diving depth range of 1- 50m, and it made use of waterproof cables. The robot could move forward/backwards and turn clockwise/counterclockwise. The research focused on the suction sludge recovery device, which sucks the sludge through the suction pump and discharges the sludge by the sewage pump. The sludge further travels in a durable sludge pipeline, which functions under high pressure. The underwater robot was first used by the U.S Navy in the early 1960's (seascape BV, 2017) the analysis of this robot's classification was developed to help utilize the operation of submarine oil and gas industry. In 1980 the system was adopted by oil and gas commercial industries and companies for their ocean environment investigations, and to further perform underwater inspections of facilities in power stations, on shore sewer pipelines, dam and water-tank inspection for evidence recovery, aquaculture, and drowning-victims. (Gafurov & Klochkov, 2015) investigated the history of AUV's, which were first developed in 1957 in the USA applied physics laboratory, in the University of Washington and named the Special Purpose Underwater Research Vehicle (SPURV). The SPURV was made of aluminum and had a torpedo like shape. It was driven by a crew and had a hydrodynamic shape. This system was used in oceanographic research until 1979. The AUV was controlled using an acoustic communication system. This vehicle was designed to conduct research in the Arctic water (Arctic water is the smallest of the five major ocean worlds and it spans an area of approximately 1 406 000km^2).

(Gafurov & Klochkov, 2015) discussed briefly on histories, analyzing of robot concepts and fundamentals of ocean robots. In 1989, Professor Tamaki Ura from the University of Tokyo's Institute of Industrial Science manufactured his first ever existing underwater robot called the PTEROA 150. The purpose of creating the PTEROA 150 was to make an underwater robot that would cause a breakthrough in the field of underwater exploration. Professor Ura realized that an unmanned robot without cables could have a greater freedom of movement and will reduce costs. The research was completed in 1989.

(Pawlus et al., 2016) analyzed oil conversion systems, which is known as hydraulic exploration today. This has moved into more extreme environments, forcing technological advancements to cater for converting hydraulic extractions into electrical extractions. (CPV Manufacturing, 2015) Discussed about crawlers' traction system that autonomously use pumps to push hydraulic fluid through the system to create fluid power. This fluid passes through the valve and flows through the cylinder, where the hydraulic energy is converted back into mechanical energy. These valves help to direct the flow of the liquid and relieve pressure when needed. The operation uses hydraulic fluid to control and operate mechanical energy. These methods of operations have limitations of which some are mentioned in my statement of research. According to Andy Arendt, (2020) the increased use of hydraulic machines in today's market has caused a substantial rise of hydraulic problems which include ocean pollution, ocean noise pollution, air pollution, elevated temperatures, and slow/erratic operations. Andy Arendt further stated that a leak in hydraulic

systems that operate in hot areas might result in a fire outbreak. In addition, Arendt stated that the burst of hydraulic lines as well as excessive exposure to hydraulic fluids lead to serious injuries and health issues. The MK3 ROST hydraulic tractors used in ocean exploration are classified as a liquefied system of hydraulic machines, which are sensitive to temperature changes during operation. Poor resistance of the working fluid occurs when the working fluid is in operation and becomes overloaded with pressure. Therefore, it poses a much-hidden danger of leakage if traction is overpowered. The MK3 hydraulic tractors are notorious for being difficult and costly to manufacture. It is also known that their power is not suitable for long-distance transmissions thus, requiring more electrical power to operate in such conditions.

The electric powered robotic subsea dredging crawler developed in this research is developed based on three fundamental analyses, with are the tank traction system dynamics, communication systems, and its boom arm dredging system kinematics. This crawler is not operated or controlled using hydraulic fluids or oil, it is a scaled down model that can be powered using 12-volt battery with 3000mAh capacity as shown in the functional model. All the electronic components are sourced off the shelve and the frame is made of 1050 aircraft grade aluminum.

The AMTL has successfully used the Tetrix Max kits to build different differential drive robots, of which one can be seen in figure 5 below. They have also developed a system for an electric tank drive tracking system and an electronic boom arm, which is controlled through a wireless user interface. This system can drive the tracked system required using DC motors to move the entire model**.**

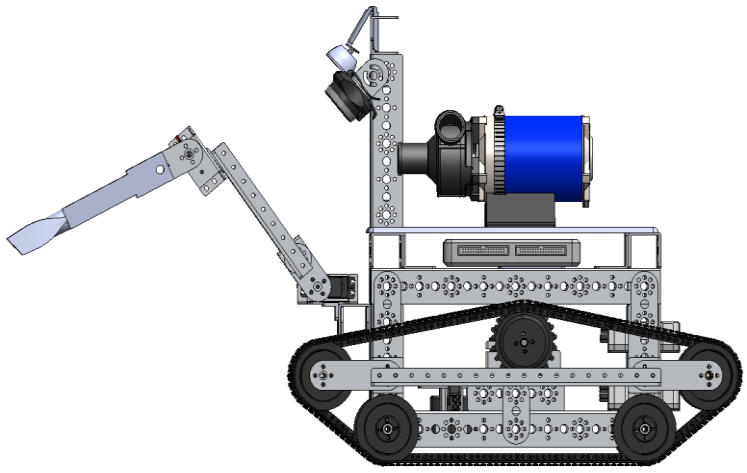

Figure 1.5: track Bot for drive system of an electric powered robotic crawler

Daanen, (2017) who presented the development of a robot model that describes the interaction between a track drive system and the seabed. He presented it together with the governing aerometers and processes in a report. Based on the model, an analytical tool qualifying and quantifying the impact of these aerometers was developed. This entails that analytical tool can be developed to analyses the interaction between a track drive system and the seabed.

With the use of the LabVIEW as a programming language and NI MyRIO as a micro controller, the EPRSDC can move autonomously or use control inputs from a user. It is controlled by an umbilical cord or Wi-Fi. According to (Christensen et al., (2010)), Global Navigation Satellite Systems (GNSS, e.g., GPS), Wi-Fi does not work underwater since higher frequency radio signals become unusable once the sensor is submerged, due to the water's strong attenuation.

1.4.1 Fire Fighting robot

In February 2021, the AMTL designed and modelled a firefighting robot with a drive system that can rotate 360° in a fixed position, using the Tetrix robotic kits. The Omni-Directional wheels allowed the robot to move in any direction without turning. The Omni-Directional Wheels are manufactured from Glass-filled Nylon with high-traction rubber rollers.

Figure 6 shows the firefighting robot built at AMTL with a detection unit which detects fire and sends a signal wirelessly to the mobile firefighting robot. The mobile firefighting robot would then autonomously navigate its surroundings using sensors to detect the location of the fire and extinguish it. Once the robot has successfully extinguished the fire, it returns to its original position. The system was programmed using LabVIEW. The system is very similar to the underwater electrically powered robotic crawler.

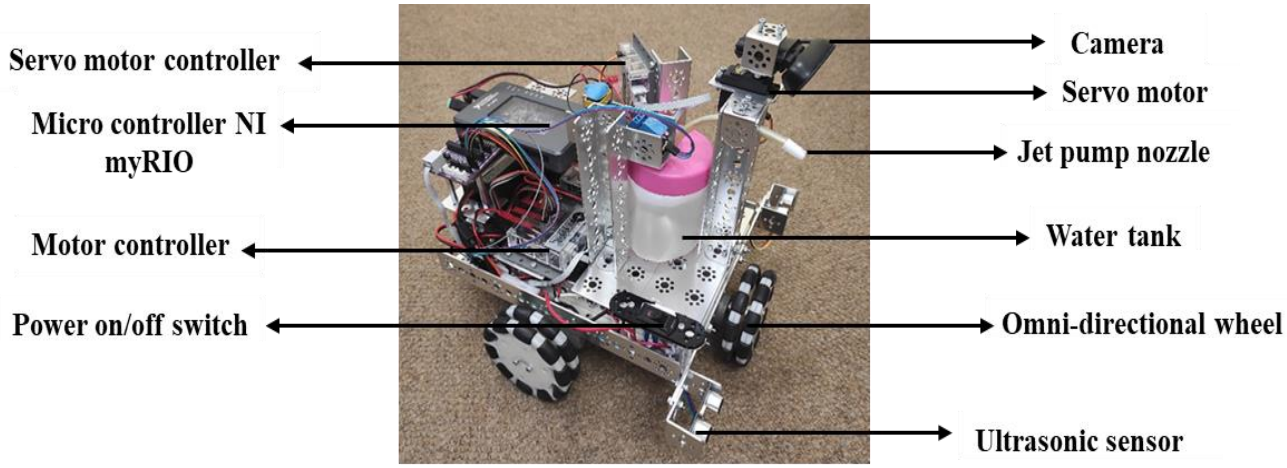

Figure 1.6: AMTL mobile fire-fighting robot

A s seen in figure 1.6, Using the Tetrix robotic kits, the AMTL was able to develop the structural design and electrical system seen in the above figure 1.6. The firefighting system was developed with the following objectives:

Autonomous fire detection, Identification of location of the detected fire, Autonomous navigation of a mobile firefighting robot to the location of the fire, Autonomous fire extinguishing (by spraying a liquid at the fire), Autonomous navigation of the mobile firefighting robot back to its initial position

The firefighting robot system comprised of two different units.

1. Fire detection unit.
2. Mobile firefighting robot

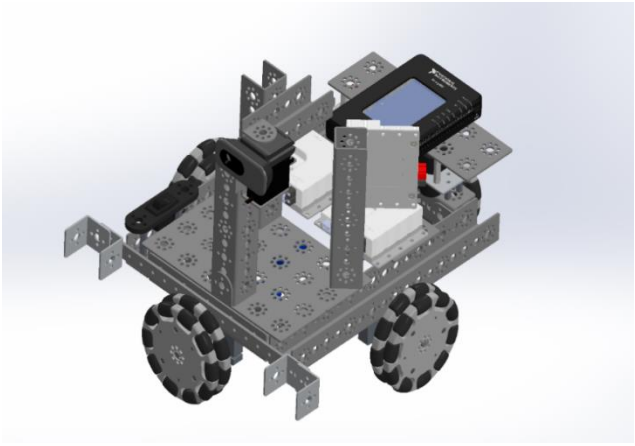

Figure 1.7: 3D AMTL mobile firefighting robot

Figure 1.7 illustrates a firefighting robot system that uses structural components from Pitsco Education Tetrix robotics kits. Water was used as the firefighting liquid for the robot model. National Instruments' NI myRIO was used as a micro controller for controlling the system. A Logitech webcam was used to run the machines vision algorithms that would detect the fire. The robot could detect and avoid obstacles during its navigation process by using two ultrasonic sensors. A small centrifugal pump was also inserted into the water tank to pump water through the nozzle when the robot is in position to put out the fire. The details of the robot's functionalities are as follows:

1.4.1.1 Autonomous Fire detection

The camera in the fire detection unit detects the fire. The system has been trained to accurately identify fire using a variety of sample fire images. After detecting the fire, a signal will be sent to the mobile firefighting robot.

1.4.1.2 Identification of location of the detected fire

This is done by the fire-fighting robot as it receives the signal from the fire detection unit.

1.4.1.3 Autonomous navigation of a mobile fire-fighting robot towards the location of the fire

The mobile fire-fighting robot autonomously navigates the location of the fire using the ultrasonic sensors to avoid obstacles on its way. The Omni-directional wheels help the robot to move in almost any direction.

1.4.1.4 Autonomous fire extinguishing (by spraying a liquid at the fire)

The mobile firefighting robot is equipped with a camera that has been trained with many sample pictures of fire to detect fire. When the robot reaches the location of the fire, it identifies the fire and positions the nozzle in the direction of the fire, using the webcam vision. The pumps are then activated until the fire is put out.

1.4.1.5 Autonomous navigation of the mobile firefighting robot back to its initial position

The robot navigates back to its original position while also avoiding obstacles on its way back.

In 2018 and 2019, An autonomous airborne docking and undocking system for micro drones to a mother drone was developed at AMTL using the Tetrix max. The docking system was designed using the DC gear motor and the 4" Omni-directional wheel, also known as poly-wheels, pack from the Tetrix kit. The docking system utilized a differential drive-based robot. Again, the omni-directional wheel were used and the performance was decent. It is very important to identify what type of drive system will be needed in any robotic system. Using the Tetrix kits at the AMTL has helped a number of researchers in identifying different drive systems. The below robot in figure 8 was powered using a DC motor with different track drive systems.

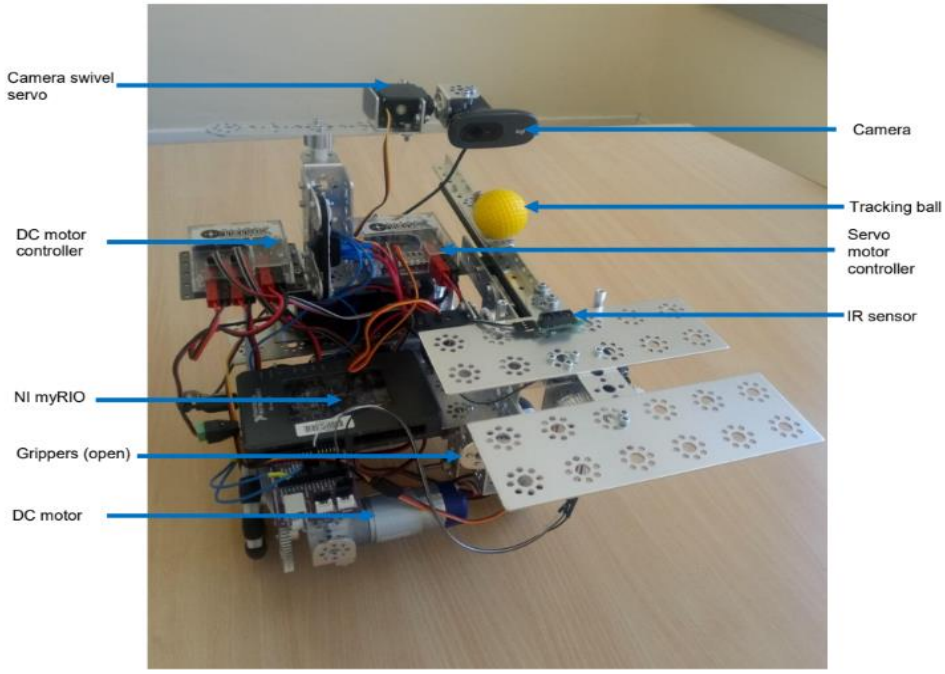

Figure 1.8: Docking and undocking system ground station

As seen in figure 1.8, the docking and undocking system of the autonomous micro drone to the mother drone required a multifunctional drive system. The driving system allowed the structural frame to perform the necessary multi-directional movement.

1.4.2 Hydraulic systems, fundamental basic principle of hydraulics, and basic formulae

A hydraulic drive system within a subsea transport extraction system refers to the method of providing movement for the tank drive system and the hydraulic boom arm. These two systems use a special hydraulic fluid, usually oil-based, that gets transferred to various rotational pumps, arm joints, the telescoping sector, and to the end effector. The hydraulic power drive and arm consist of a power supply, one or more motors depending on the production specification, a set of pistons, valves and a feedback loop. (Airline, 2019) analyzed the hydraulic power drive system which incorporates other hydraulic principles both on crawling, airline and other hydraulically propelled arms and drive systems, which are mathematically expressed using some basic principles in table 1.1.

Table 1.1: Basic Hydraulic Formulae (Sphaera training system, 2021)

Formula for name	Equation world formulas	Letter formulas
Fluid pressure in pounds/square inch	$p = \frac{\text{force(Newton/pounds)}}{\text{unit area (square meters/square inches)}}$	$p = \frac{f}{A}$ or PSIG $= \frac{f}{A}$
Fluid flow rate in gallons/minutes	$\text{flow rate} = \frac{\text{VOLUME } (m^3/\text{gallons})}{\text{UNIT TIME (S/minutes)}}$	$Q = \frac{V}{T}$
Fluid power in horsepower	$\text{horsepower} = \frac{\text{pressure (psig)x flow(gpm)}}{1714}$	$HP = \frac{PQ}{1714}$
Velocity through piping in feet/seconds velocity	$\text{velocity} = \frac{0.3208 \text{ x flow rate though i. d (gpm)}}{\text{internal area (square inches)}}$	$VA = \frac{.3208Q}{A}$
Compressibility of oil in feet/second velocity	$\text{added volume} = \frac{\text{pressure(psig) x volume of oil undr pressure}}{250{,}000 \text{ (pprox)}}$	$v_A = \frac{PV}{250{,}000}$
Compressibility of a fluid	$\text{compressibility} = \frac{1}{\text{bulk modulus of the fluid}}$	$C = \frac{1}{BM}$
Specific gravity of a fluid	$\text{specific gravity} = \frac{\text{weight of cubic foot of fluid}}{\text{weight of one cubic foot of water}}$	$SG = \frac{W}{62 \cdot 4282}$

1.4.3 Hydraulic principles

1.4.3.1 Pascal's law:

Blaise Pascal, who was a French philosopher, mathematician, scientist, inventor, and theologian comprised and combined a principle that he formulated in the year 1647 that incorporates the basic principle of hydraulics

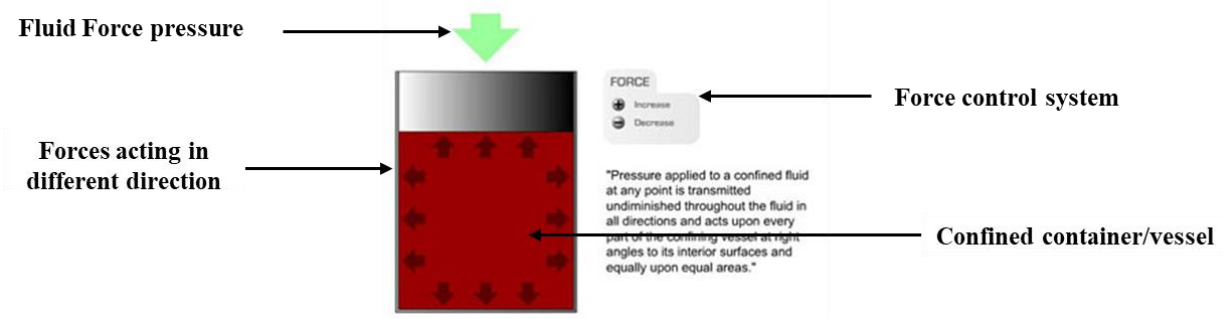

Figure 1.9: basics of hydraulic principles (Sphaera training system, 2021)

Figure 1.9 shows the expression of forces and pressure acting in a confined fluid. This well-structured diagram demonstrates hydraulic fluid in a container surrounded by high applied pressure.

In simple terms, Pascal's law states that:

A change (or changes) in pressure at any point on an enclosed fluid at rest is (are) transmitted undiminished to all points in the fluid.

Pascal's law implies that pressure applied anywhere on a body of fluid causes a force to be transmitted equally in all directions, with the force acting at right angles to any surface in contact with the fluid. This principle is derived based on the high or low pressure of fluid applied to a confined enclosed space at any point which is transmitted undiminished throughout the fluid in all directions and acts upon every part of the confining area of the vessel at right angles to its interior surfaces and equally upon equal areas.

1.4.3.2 Hydraulic pressure and force

The pressure exerted by a hydraulic fluid is the force per unit area exerted on a surface, in other words the force divided by the area of that surface.

Pressure = force/surface Area. In summary, hydraulic force is the force per unite area exerted by a fluid on the surface within the container.

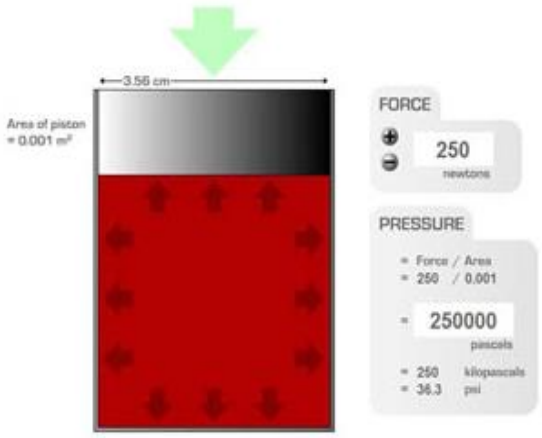

Figure 1.10: hydraulic pressure and forces (Sphaera training system, 2021)

Figure 1.10 shows an expression of Pascal's mathematical equation. On this hydraulic pressure test, the area of the piston = $0.001m^2$, force in newtons = 250,

Using the $P = \frac{\text{force(pounds)}}{\text{unit area (square inches)}} = \frac{250}{0.00\text{Im}}$ = 250,000 pascals.

1.4.3.3 Simple concepts for hydraulic systems (Bramah Press 1795)

Basic hydraulic systems are formulated within a jack and consist of two fundamental different design sized cylinders which are connected by a distribution pipe.

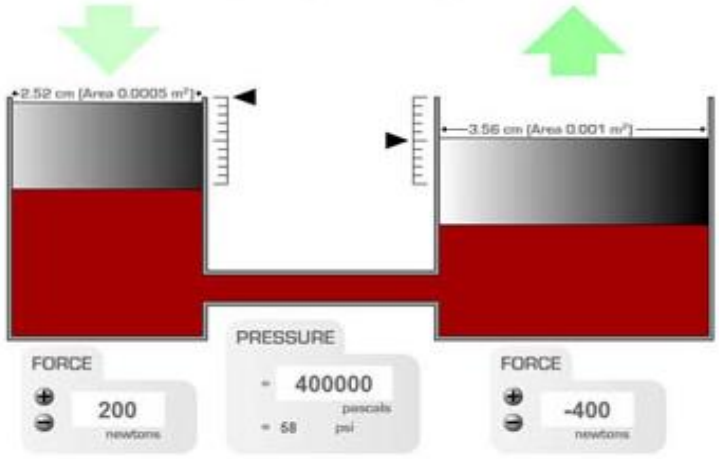

Figure 1.11: A simple diagram of a hydraulic system (Sphaera training system, 2021)

Figure 1.11 exhibits a demonstration of a simple diagram of how a hydraulic system works. The buttons, represented by a positive (+) and negative (-), provide a clear image of a full control system for the amount

of force applied. The pressure and force are clearly indicated both numerically and with the use of color. The systems of different piston ratios are available within the image.

In respect to Pascal's law of hydraulic systems, the force of pressure exerted on a smaller piston is transmitted through the fluid to act on the internal surface of the larger piston of any working device. Pressure in this system is a property of its own system (not the pistons) and is therefore experienced equally by each piston. Since each piston has a different surface area, the force exerted on each piston will be different, regardless of having the same pressure.
If the larger piston is twice the area of the smaller piston, then the force on the larger piston will be twice as great. In order to create that extra force, the smaller piston has to be moved by twice the distance.

1.4.3.4 Hydraulic brakes on drive systems

In a hydraulic system, the braking system is of great importance. The slave piston has a larger area compared to the cylinder, as represented in the arm control boom of a hydraulic crawler. In the mathematical expression, the pressure force applied to the master cylinder is multiplied as the fluid exerts the resultant pressure on a greater surface area in a cylinder.

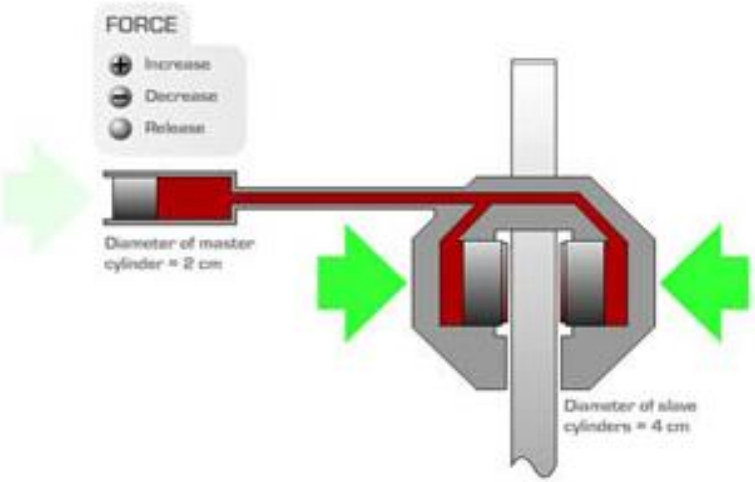

Figure 1.12: hydraulic brake system that represent drive systems (Sphaera training system, 2021)

Figure 1.12 shows a simple hydraulic brake drive system. The transfer of hydraulic energy is used to control the movement of a rotating axle. The system has just two cylinders and a disc brake. This cylinder could be connected through tubes, with a piston inside the cylinders. These cylinders are filled with incompressible oil (hydraulic fluid).

1.4.3.5 Basic principle of Hydraulic non-return valves

Non-return valves also called check valves are directional control valves used to direct hydraulic fluids which are used in hydraulic drive systems. These valves can be used as a prefill valve, bypass valve or pre-tensioning valve, for the protection of hydraulic components against pressure surges in an operational driving hydraulic system.

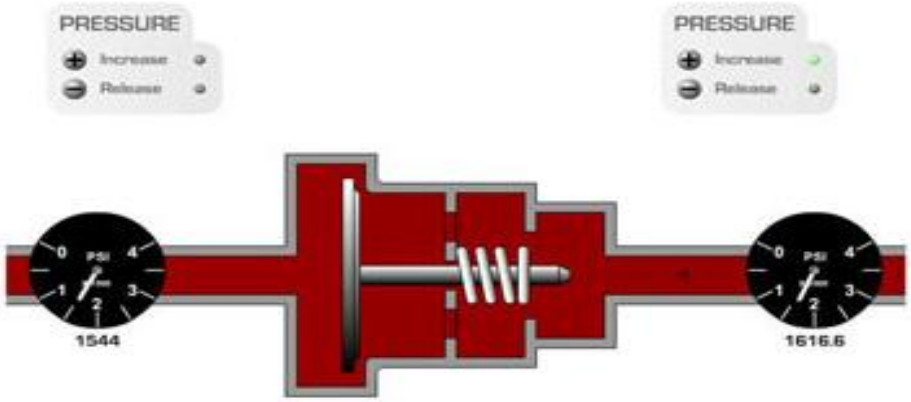

Figure 1.13: A simple diagram of a hydraulic non-return valve or check valve (Sphaera training system, 2021).

These non-return valves are systems installed within hydraulic systems in order to stop the return of fluids in the opposite direction to which they are pumped from. The non-return valve is illustrated in figure 1.13. The pressure exiting from each end of the non-return valve can be controlled in order to demonstrate or observe the valve's ability to open and close depending on the changing pressure.

1.4.4 Electric drive system

Electric drive systems refer to a variety of drive mechanisms which use controllers to regulate the speed, torque, power, and direction of electric motors. Different types of electric motor drives exist today using different methods of motor controllers and motor control. For our electric powered robotic subsea dredging crawler, the electric motor drive system receives power from the motor controller unit (MCU). The MCU, receives power from the main distribution centre called the power supply centre (PSC) which is our 12V 3000 mAh battery. The MCU and PSC are controlled using the NI myRIO which is the main micro controller for our model.

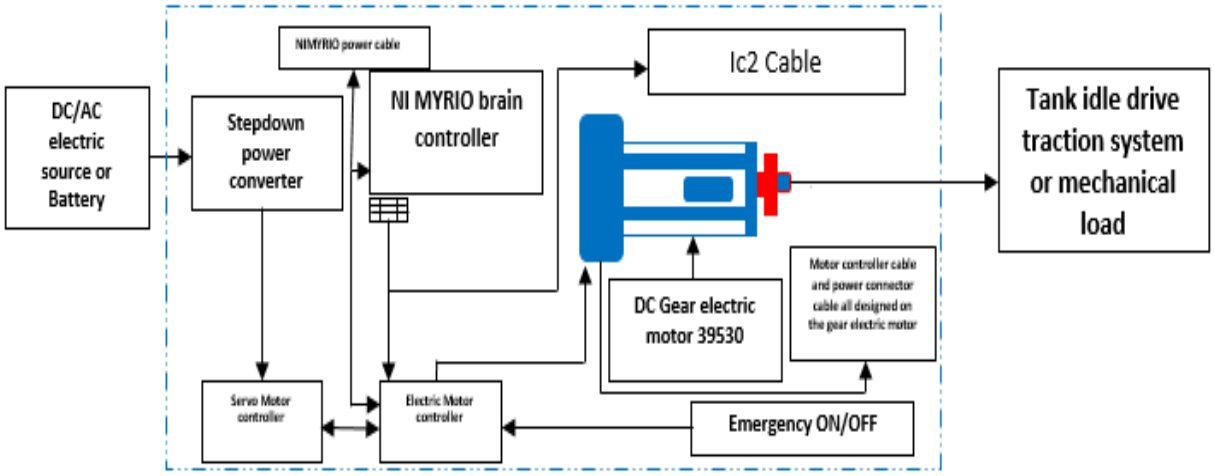

Figure 1.14: A simple block diagram of the EPRSDC motor drive system

Figure 1.14 illustrates the concept of our EPRSDC. The motors have inbuilt sensors(encoders) which measure the rotations of the shaft. The measured rotations are sent as signals to the microcontrollers. The NI myRIO controller is responsible for processing the necessary feedback and controls for the functioning of the motors.

1.4.5 Electric motor drive classification

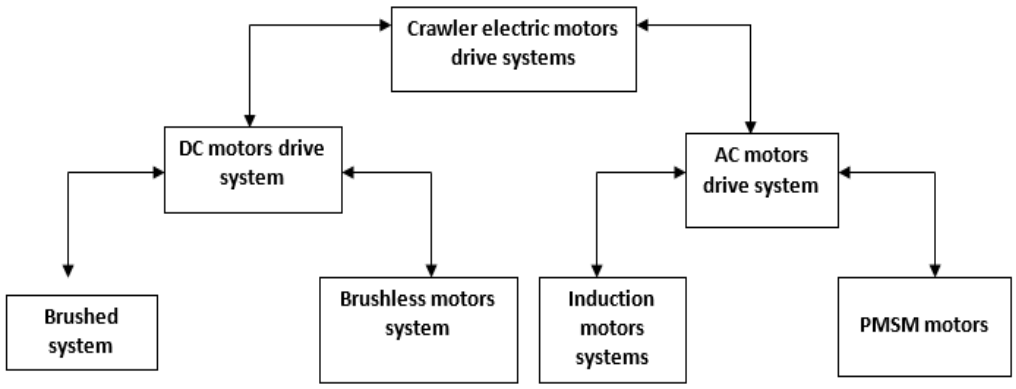

Figure 1.15: simple block diagram of a classification of an AC/DC motor permanent magnet synchronous motors drive systems

Diagram 1.15 shows a quick overview of how motor drive systems are classified. Table 1.2 classified where AC (induction) and DC (brushed and brushless) motor are applied in terms of voltage and power levels in our crawler drive system, along with the pros and cons of each.

The table below further shows more information on electric motor drive systems.

Table 1.2: Comparative Analysis of Electric Drive Motors

Drive motor type	Classified voltage level	Power level of system	Application of system	Advantage of system	Disadvantage of system
Brushed DC gear motor drive.	<100 volts.	<100 volts.	Crawler tank track drive system, servo motor boom arm drive control system.	High torque, low power consumption, easy to maintain and replace.	Brushes wear out inefficient.
Brushless DC	< 600 volts.	Up to a few kW	Model dredging pump, and jet pressure pump for soil breaking	This motor has high power efficiency, long life and very reliable	High cost due to subsea application, complicated control system
AC induction for scaled up model	< 600 volts.	< 750 W.	Scaled up motor crawler motor drive design	Low cost, less maintenance, rugged, reliable in wide power range	Not readily available

In the selection of a motor drive system for our electric powered robotic subsea dredging crawler, we are required to look at the power voltage level while addressing questions that depend on the application. An example could be the electric motor starting torque, load inertia, power, and pattern of operation, environmental conditions, or motor's suitability for ocean application.

Electric motors are classified as electromechanical machines that convert electrical energy into mechanical energy. The crawler converts it electric motor energy into mechanical energy by driving the entire dredging body frame system.

Power is work performed over a specific amount of time. In an electric motor, power is delivered by converting electric energy into another form (kinetic energy). This brings us to some further definitions related to power.

Power = $P = \frac{w}{\Delta t}$
where p = power, w = work done, Δt = elapsed time

Some other related fundamental concepts include:

a) Voltage: is the force required to move electronics

b) Current: is the rate of flow of charge per seconds through a material with a specific voltage application.

$P = V \times I$

Where (p) watts, voltage (v) is in volts and current (I) is in amperes.

Watt (W) is the unit for power, and this is defined as one joule per second.

1.5 Other applications of the EPRSDC

Our design could find other areas of application outside mining. we have listed three possible areas.

1.5.1 Pipeline inspection, and tank cleaning:

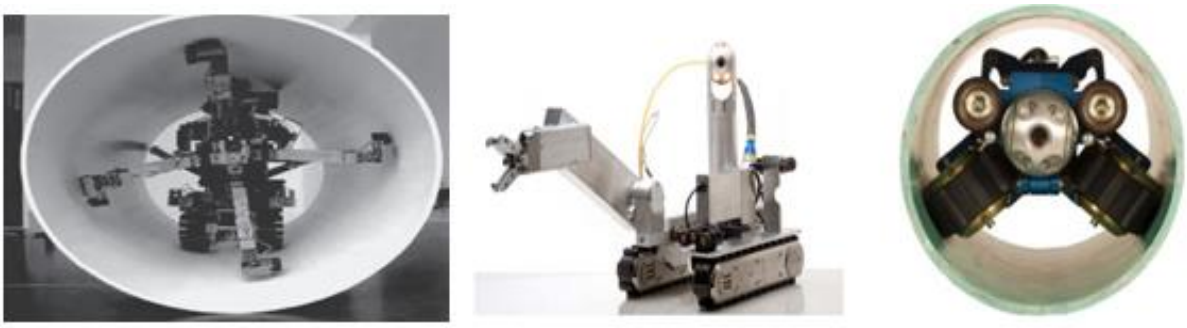

Figure 1.16: Pipeline cleaning, inspection, and tank cleaning robot (Bogue, 2011) and (Deepak et al., 2016)

A scaled down robotic crawler can be used for pipeline imaging operation and tank cleaning. Deepak et al., (2016) presented some research on the development of various robotic sensors used in performing pipe inspection, operation and cleaning, and determination of flaw/crack, corrosion-affected areas, blocks, and coated paint thickness. He stated that these systems can be controlled with various actuators such as DC motor, servo motors and pneumatics. He also stated that electric robots can be used for offshore operations such as pipeline inspection and cleaning. This will reduce the already high cost of maintenance.

1.5.2 Firefighting

Figure 1.17: Crawling Firefighting robot (Cervantes et al., 2018)

As shown in figure 1.17 Firefighting robots are mainly used in various firefighting rescues such as oil, gas, gas leaks, explosions, tunnels and subway collapses (Jia et al., (2019)). (Cervantes et al., 2018) presented the design of a firefighting robot. In his presentation, the jet pump nozzles were said to be designed for high pressure water discharge. The paper focuses more on the obstacle-surmounting problem of small crawler fire-fighting robots. The drive track concept was discussed with regards to independent spring suspension systems with good damping. The robot was designed with an automatic lifting platform, which is more conducive to information collection on a fire scene.

1.5.3 Electric robotic crawler in agriculture farming, irrigation, and plantation system

Figure 1.18: electric crawlers used for farm operations (Adam Stager, 2019)

Adam Stager, (2019), a doctoral student from the University of Delaware designed an agricultural electric crawling robot. He reported that the aim of this research was to combat the range of challenges in agriculture. This implies improving agricultural yields and planting resiliency, increasing pest resistance, addressing nutrient insufficiency, and improving more scientific research that relates to this robot. He

further discussed algorithms and electrical circuit designs for the testing of robot machinery at the University of Newark.

1.6 Delineations of Research

i. The study will not include propelling the crawler wirelessly.
ii. The study will not include designing of crawler control circuit boards and electronic components
iii. We shall not consider the hydraulic powering control system
iv. The focus will be more on the analysis of the electric powered robotic subsea dredging crawler design mechanism, drive proposition and the programming algorithms

1.7 Significance of Research

In this digital era, rapid advancements in robotic mining extraction technologies are at the forefront of the mining industry. The electric-powered robotic subsea dredging crawler is a concept with the potential to revolutionize underwater mining exploration.

1.8 Anticipated Outcomes of the Research

i. Conversion and comparison of the electric powered subsea robotic dredging crawler into the hydraulic powered crawler MK3 ROST.
ii. Publication in the Aeronautical Aerospace and Mechanical Engineering conference 2022.
iii. Presentation of paper during the Aeronautical Aerospace and Mechanical Engineering conference 2022.
iv. Thesis for the fulfilment of Master of Engineering in 2022.
v. Master of Engineering (MENG) degree in Mechanical Engineering.

1.9 Contributions of the Research

The major contributions of this research work are:

i. The scale-down model will aid in choosing the component that will be most useful in defending the idea when the crawler is scaled up for industrial applications. This can be done by creating a scaled-down concept, which will also be less expensive.
ii. Development of an electric powered robotic subsea crawler for ocean dredging and other application.
iii. Assembling and programming of the electric powered robotic subsea crawler for dredging.
iv. Improving the quality and capabilities of its mode of operation under different Ocean floor condition.

v. A solution to the limitation of current hydraulic dredging crawler technology.
vi. A new approach to the utilisation of robotic subsea crawler for different application.

1.10 Outline of the Thesis

This thesis consists of seven chapters:

Chapter 1: This chapter presents the problem statement, aim, and objectives of this thesis. Furthermore, the background of the research problem is discussed. To provide more details, the concept of the electric-powered robotic subsea dredging crawler is presented. Some contemporary challenges regarding the hydraulic system in ocean extraction are also mentioned. After which some anticipated applications of the EPRSDC for mining systems are stated and discussed, along with the delineation, significance, and contribution of the research.

Chapter 2: This chapter begins with a brief introduction to ocean mining and its history. We further discuss more on hydraulic subsea tractors for mining, brief history of hydraulic drive systems and its application to ocean exploration, hydraulic subsea tractors features (parts and their functions). The next section focuses on mathematical formulations for robotic vehicle dynamics and kinematics on an ocean floor. The chapter ends with discussions on homogenous clear conversions, transformations, FEA simulations for EPRSDCs and a brief review of ocean hydrodynamics effects on underwater vehicles using CFD tools.

Chapter 3: This chapter started by presenting the undercarriage system of the EPRSDC. After which the electronic components were discussed with respect to their specifications and functions. The next section covers the design and manufacturing of the venturi dredging nozzle. Following that, the software used was mentioned. In the subsequent sections the test environment, final design, waterproofing concepts for future design and the test ramp were presented respectively.

Chapter 4: This chapter starts with presenting the CAD model and physical model of the EPRSDC. Afterwards, the User Interface (UI) was presented. The next section covers the drive test carried out and the corresponding control program used to handle mechanical errors in the driving system. After which the dredging test is discussed. The next section covers the drive experiments performed for 5 different angles of inclinations. FEA simulations on the EPRSDC preliminary design is presented next. The chapter concludes with some discussions on the specification of the final design.

Chapter 5: This chapter briefly presents discussions on results shown in chapter four. The results are presented in data tables, graphs and corresponding correlations represented with quadratic functions.

Chapter 6: This chapter briefly presents the research conclusions, applications and future prospects for the EPRSDC.

Chapter 7: This chapter briefly presents recommendations for the EPRSDC design, waterproofing, driving system, CFD simulations and FEA simulations.

CHAPTER TWO: LITERATURE REVIEW

This chapter begins with a brief introduction to ocean mining and its history. We further discuss more on hydraulic subsea tractors for mining, brief history of hydraulic drive systems and its application to ocean exploration, hydraulic subsea tractors features (parts and their functions). The next section focuses on mathematical formulations for robotic vehicle dynamics and kinematics on an ocean floor. The chapter ends with discussions on homogenous clear conversions, transformations, FEA simulations for EPRSDCs and a brief review of ocean hydrodynamics effects on underwater vehicles using CFD tools.

The major oceanic and coastal mineral resources are found in the following countries: Australia, China, U.S, Russia, and Chile, Peru, South Africa, Congo, New Caledonia, Chad, and others. In South Africa, three aggregated mining economic sectors have created employment for South Africans from 1970 till date (Fedderke & Pirouz, 2002). Gold, diamond and uranium mining have made an excellent impact in contributing to the economic growth of the labour market from the 1990s. Mining companies in South Africa have identified methods and tools that can be used for ocean extraction operations. IMDH Group, (2016) still use the MK3 ROST hydraulic tractor mother dredging crawler as their main tool for ocean hydraulic extractions in South African and Namibian oceans. The modified hydraulic tractor is equipped with a dredging pump system of 2.4MW power, a 500kW hydraulic power pack and 500kW jet water system. It is also said to be their best underwater mining tool yet. The MK3 ROST is powered by an electrical 3.3kW motor with a variable speed drive (VSD) supplied from the vessel through a special custom-made umbilical cord. It contains two main parts namely:

1. The tank traction drive system
2. 2 DOF boom arm suction system

These systems are controlled and automated by a hydraulic system.

(Erin Sparks et al., 2019) stated three important steps in ocean mining of manganese nodules and they are:

1. Underwater sediment excavation and removal from the ocean bed
2. The sediment lifting and sampling treatment

3. The on boarding treatment.

These three steps were built into features for a self-propelled seafloor mining robot. This system was designed as a hydraulic experiment for mining operations. The self-propelled mining robot performed velocity control using a PIC, Proportional Integral Controller, from gain tuning formula based on the model identification. Khan A. Arbab et al., (2015) stated that rapidly growing mining activities carried out on terrestrial areas can lead to a massive diminishing of minerals over time. Hence, the discovery of marine minerals brought a relief with regards to the threat of depleting natural resources in terrestrial domains. There were however further discussions with regards to the large amounts of mineral deposits discovered in ocean floors. One of the discussions included the fact that these vast resources have potential for large economic benefit. Thus, Government authorities still maintain the rights to these resources. One of the critical issues surrounding ocean exploration is discovering the right equipment to use for the dredging of these minerals from the ocean floor. Khan A. Arbab et al., (2015), further elaborated on the classifications of marine mineral resources. This was broadly classified into two categories which include:

2.1 Marine mineral deposits from terrestrial source

These originate from chemical and mechanical disintegration of rocks on land. After this disintegration, the eroded rock debris is transported to the ocean by rivers, where they are sorted by the waves based on their density. Furthermore, the marine mineral deposits combine with terrestrial and deep ocean resources.

2.2 Marine minerals from ocean basins

These marine deposits include those that originate from the depths of the ocean and are driven from the disintegrated rock deposits and mineral precipitation inside the ocean bed.

2.3 History of hydraulic powered systems and mining in South Africa

Aggressive hydraulics & fluidpower, (2021) stated that in 1648, a French physicist named Blaise Pascal discovered that pressure transmitted an equal force in all directions on a confined fluid and that these forces could be harnessed. It was not until 1738, when Daniel Bernoulli put this to use by pressurizing water in a pump and mill using the Bernoulli principle.

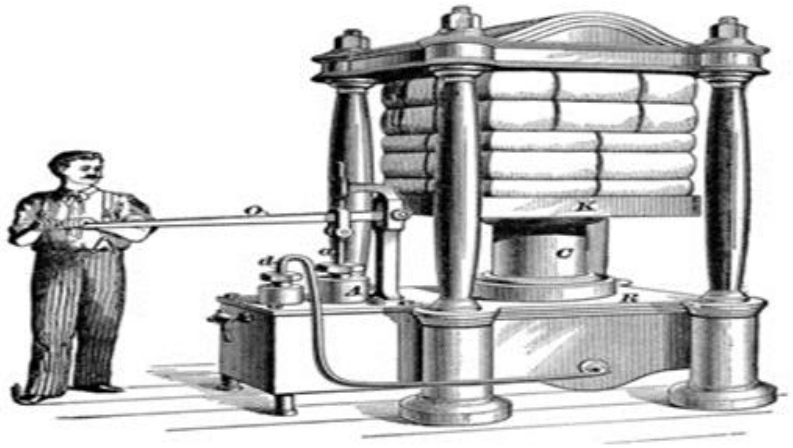

Figure 2.1: hydraulic press using Pascal's principle (Joseph Bramah, 2020)

Figure 2.1 shows the first hydraulic system produced 60 years later in 1795 which was patented by Joseph Bramah. He built a hydraulic press in England, paving the way for the industrial revolution to automate things from printing presses to cranes, to machines for cutting and stamping, and thus automating the manufacturing process. Over time it was discovered that water was not the best material for hydraulic pumps and motors, and a non-corrosive oil was implemented as a better fluid for hydraulic applications. The use of oil served many purposes aside from its non-corrosive properties; it was denser and could handle higher loads, it was resistant to evaporation, it remained cooler under the high pressure of hydraulic forces. As the use of fluid power evolved, so did hydraulic cylinders with materials, applications, mounting configurations, and internal designs developed even further. Major advancements in the last 75 years have seen where hydraulic cylinders are at work on cranes, moving heavy objects, building skyscrapers, aircraft control surfaces and landing gear, controlling ships at sea, drilling, mining, and factories controlling machines for manufacturing. Fluid power can provide up to 10 times the power of an electric motor, making it ideal for heavy pushing, pulling, and lifting applications. According to Naidoo, (2013), mining of natural resources has played an important role in the economic growth of South Africa. From the history of the European labour to the migrant labour system that was characterised as apartheid, South Africa's mineral resources have moulded confined standards in the political, social, and economic paradigm for the last 140 years in the history of this great country. This mining has not only shaped the early development of legislation of South Africa to protect the health of mine and public workers in the 1900s. It has also laid out an excellent platform for both South African and international researchers to produce ground-breaking research tools for both in-ocean floor and on land mining. This further increased the amount of health researchers that investigated mining-related respiratory diseases throughout the last century. The history of the introduction of mining in South Africa is dated back to the late nineteenth century, which is synonymous with silica exposure, silicosis, and tuberculosis in the mining environment. Due to the rapid

increase in the spread of these diseases, the Mine Health & Safety Acts, the Leon Commission of Inquiry, revised legislation, national and international courts challenges are addressing the concerns of work-acquired respiratory diseases. The increase in ocean mining activities with the use of protective equipment is reducing the risk of respiratory diseases common with land mining. John E. Flipse, (1985) advocated for the reduction of inland and ocean mining activities based on the negative effects on the environment observed within 1965 to 1980. The US government, academic organisations, and industrial programs collaborated to sponsor research aimed at reducing the negative effect of mining activities on the environment. In his research, academic institutions, the US Government, and metal industrial organizations research-based solutions which were implemented through several consortia that undertook model designs, pilot plants and prototypes, research tests that demonstrated technical feasibility of non-destructive ocean mining and processing in the deep ocean floor. After many practical concepts, investigations and model testing with several years of decreasing investments on mining within 1977-1978, the projects were successfully completed. (Van Bloois et al., 2009), discussed critical historical developments in dredging and mining technology. He mentioned that in recent years, increasing dredging activities has instigated improvement in the technology used for seafloor extraction. With conventional dredging equipment, a depth of 300m towards the ocean floor for excavation is now possible compared to decades ago, due to the nature of technology back then. Hydraulically powered ocean dredging crawlers that are currently in use have unique fundamental features, parts, and functions. According to Tondolo, (2012), leaks in hydraulic systems are the major causes of hydraulic failures. Internal and external hydraulic leakages reduce the efficiency of the system. The detrimental external leakages are not easily identified or visible since there are no visual indicators to warn operators or technicians of the problem until system performance has been substantially impacted. Internal leakages are highly common in hydraulic ocean crawlers. They are caused by the system wearing away during operation. This contributes to the increase of pollution due to ocean contamination and cavitation. Cavities in hydraulic ocean crawlers are created by soluble gas solutions, fluid dips, and rapid pressure increases that collapse on hydraulic oil bubbles.

In engineering, the term hydraulic systems refer to the energy-transmitting assemblies that use pressured liquid as a fluid to transfer energy from an energy-generating source to a useful work point.

2.4 Parts and functions of hydraulic extractors

2.4.1 Hydraulic Pump and motors

These are used to pump hydraulic fluid in order to rotate a valve through electrical energy (motors). (Kim et al., 2005) discussed the performance of Switched Reluctance (SR) drive for hydraulic pumps. The SR drives are constant capacity pumps that are employed with maximum drive speed and torque. SR drives

are designed to maintain a predetermined oil pressure by controlling a particular amount of power during operation. This research presents a conservational concept that reduces power consumption of hydraulic pumps. The combined signals of hydraulic pump power and oil pressure are fed back to the digital signal processors and the SR drive controller, which controls the speed of the Switched Reluctance Motor (SRM). According to Ehsan et al., (2000), load digital displacement pump-motors are hybrid devices that are coupled to hydraulic pump systems with microprocessors and have high performance integrated abilities of variable flow of power. The hydraulic pump system in this thesis is based on a traditional hydraulic piston pump with a poppet valve controller for each cylinder. The hydraulic pump works on a stroke-to-stroke sequence. The modeling of this hydraulic pump was performed under variable-demand, operational condition and variable-speed for different control systems. Ehsan et al., (2000) contributed to the response of speed control for hydraulic propelled machines and their inherited energy efficiency. According to Zhu et al., (2020), electronic hydraulic pumps (EHP) are integrated high performing electrical to mechanical machines with strong working efficiencies. For the purpose of the high booming arm for the Remotely Operated Subsea Tractor (ROST) MK3, an axial piston pump based EHP is used to enhance the working performance.

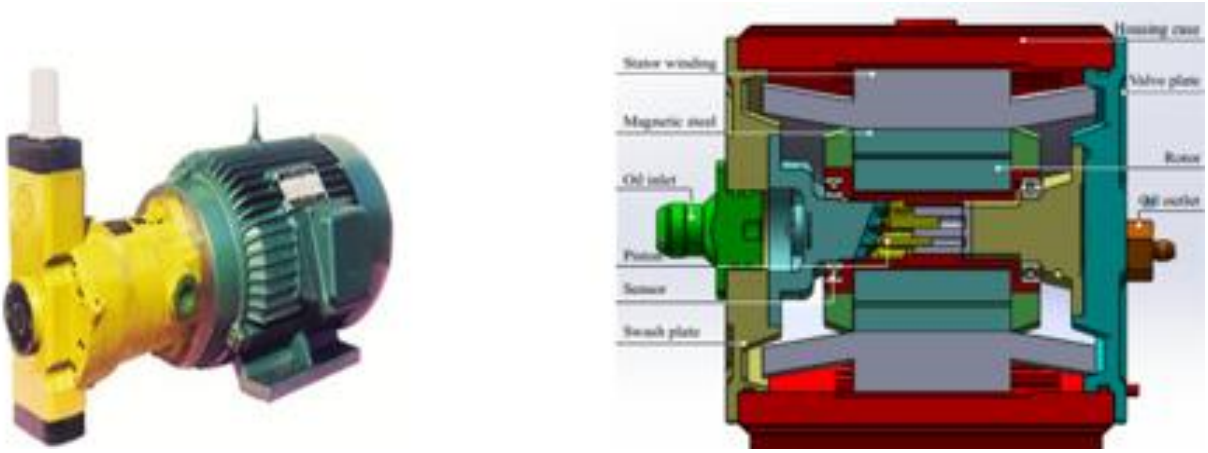

Figure 2.2: hydraulic pump unit with labeled structure of axial piston EHP (Zhu et al., 2020)

Figure 2.2 presents a fundamental unit of hydraulic pumps driven by an electrical motor. This research approached a design that improves the integration, the performance of different schemes and components which are fundamental to hydraulic pumps. The author discussed the key working elements which include the shaft rotor and electric motor, hydraulic pump, and one shared housing case. The pumps outreach shaft and dynamic sealing parts were eliminated before mounting the pump. The EHP is sometimes considered as a brushless DC driven motor. Hydraulic pumps are designed to suck hydraulic fluid with a certain force to mechanically operate a drive system called the load. The structural axle piston is composed of stator windings, rotors, main axis, regulating elements and sensing elements. Electronic hydraulic pump torque

is transmitted from a magnetic steel rotor to the piston slipper and finally to the center axis. Following the rotation of the electric motor, the hydraulic piston is fastened inside the rotor. The springs inside the pump are installed and reloaded in the axis ahead of time. The hydraulic pump forms a regulating force that causes a push and pull movement that results in a reciprocating piston motion. This system works with a swash plate and valve plates. The hydraulic oil from the tank is collected and discharged proportionally to the area containing the moving fluid during the procedure. The study presented the concept of fluid flow in hydraulic pumps, in which the tank oil input to the absorbing chamber is directed to heated fluids produced during the working process and subsequently withdrawn. The EHP hydraulic system generates energy, which is then converted to mechanical energy and then to hydraulic power. Electrical energy is converted in the electromagnetic drive which is used to generate a rotational torque rotates the pumps' rotors. Mechanical transmitters were used to enhance the pistons' drive. The reciprocal motion was produced by the rotor, while the fluid dynamics were developed by the piston reciprocating and the rotor rotating. The functional swash plates and valve plates were used for fluid absorption and ejection.

2.4.2 Hydraulic cylinders

(Pro-hydrp, 2016) stated that hydraulic cylinders are used to create a force in a single direction through a single stroke in same direction.

Figure 2.3: hydraulic cylinder and the direction of flow (Pro-hydro, 2016)

Hydraulic cylinders, as seen in figure 2.3, are used to provide a powerful force for heavy-duty applications such as construction equipment, offshore operations, ocean dredging, inland mining, and manufacturing machinery. According to Pro-hydrp, (2016), oil is a pressurized fluid that provides hydraulic cylinders with the strength to move upward or downward. The cylinder is made out of a cylinder barrel in which a piston is moved back and forth by the piston rod, creating pressure behind the hydraulic fluid. The manner in which the hydraulic cylinder is installed on the ROST MK3's boom arm has a significant impact on the cylinder's performance and lifespan. The cylinder should be mounted in an alignment position for elevating

the arm. According to Schmidt et al., (2017), hydraulic cylinders can be analyzed and controlled with a strategic format to direct hydraulic fluid, which drives the cylinder for certain application. According to this study, linear hydraulic drives and cylinders are normally implemented by proportional valves, which are supplied by variable displacement pumps that run at constant shaft speed and aim at a constant pressure level. When approaching this system from the opposite direction, the hydraulic cylinder eliminates the throttle-driven main flow.

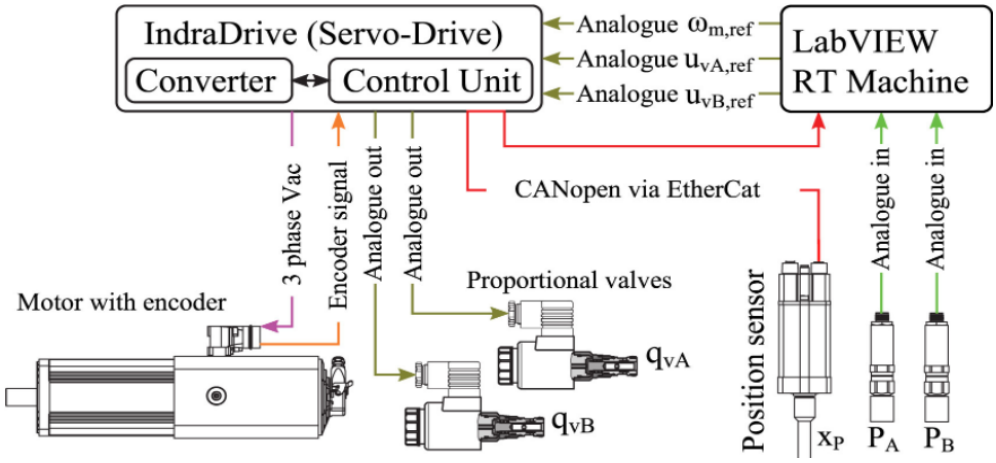

Figure 2.4: Speed-variable Switched Differential Pump (SVSDP) for Hydraulic cylinders (Aalborg University, Denmark)

Figure 2.4 shows a test bench communicating prototype of a hydraulic drive cylinder system. LabVIEW was used to drive the servo motor, the analogue out from the proportional valve QVB and to directly communicate with the control units. Furthermore, position sensors were used to get a feedback signal from the control units. The test bench consists of two opposing identical cylinders, driven by the speed-variable switched differential pumps (SVSDP), the main cylinder, and a conventional valve setup (load cylinder). (Zhao et al., 2015) highlighted how hydraulic cylinders work as actuators and discussed how system failure can have a big impact on hydraulic systems. The difficulty encountered in the application of ocean dredging tractors is the leakage of hydraulic cylinders, which, as previously indicated, are difficult to diagnose in their early stages. The author discussed the pressurized input and outflow of hydraulic signals displaced by a hydraulic cylinder's operating piston rod, which he obtained through a specifically designed test bed. A simulation was performed for varying amounts of hydraulic cylinder leakages. Their research presented the result shown by the faults extracted by wavelet packet analysis distinguished by different levels of the hydraulic cylinder leakages. (Feng et al., 2017) discussed some major difficulties encountered by mechanical driven hydraulic cylinders. Mechanical hydraulic cylinders characterize the fundamental dynamic systems, which are modified by stiffness during operation. The author provided us with a basic understanding of the impact of various factors that contribute to cylinder stiffness, such as oil bulk modulus,

formulated air in hydraulic fluid, operational deformation of the piston rod, degrees of expansion barrel for hydraulic press systems, and hose flexibility to metal expansion. The research incorporated some theoretical analysis into the experimentation of obtaining the results. The force factor was computed for each portion of the system, and the hydraulic cylinder stiffness was established. Using a hydraulic cylinder as an example, the results of the inquiry were produced and used to examine the stiffness; it was shown that the verified comparison result of the model's approximated stiffness was improved by more than 15%.

2.4.3 Hydraulic Tank

FlowFit, (2019) suggested that hydraulic tanks are places where hydraulic fluids are stored. Tič & Lovrec,(2012) discussed about how irrespective of the advancements in hydraulic-driven machines in recent years, which have provided great efficiency and structural component durability, hydraulic tanks are sometimes overlooked during hydraulic equipment improvements. A CFD simulation of the hydraulic oil tank was performed to calculate the oil flow inside the tank, and this article offered us the full design of a 400-liter hydraulic tank. The CFE was also utilized to investigate how to reduce oil whirling and increase flow stability in different channels.

Figure 2.5: conveys a hydraulic tank according to third model (Tič & Lovrec, 2012)

According to the author and figure 2.5, for streamline cutting and modeling, third-generation model design, modeling, and simulation software tools were employed. As a simple and inexpensive measure of the intensively direct and stabilized oil flow, the velocity vector and turbulent kinetic energy were adjusted to construct partition walls. There were two to three partitions in the hydraulic tank, which raised the level of the oil flow rate. The dividers were longitudinal, which gave better calming for the oil. More stationary fluids were utilized, resulting in an unfavorable outcome; hydraulic oil swirl was reduced, resulting in increased stability and fluid flow. The result of this simulation shows that a 400-liter hydraulic tank can be

further used for oil flow analysis in more complex simulations. Hydraulic tanks have several basic purposes, including cooling hydraulic fluids, removing air, removing condensate, and removing contaminants.

2.4.4 Control Valve

Dr Thomas Peacock, (2015) stated that hydraulic safety valves are pressure controllers used to regulate the fluid pressure passing through hydraulic systems, to maintain the desired pressure levels. (Kim et al., 2009) stated that the NFC (Negative Flow Control) is used by pumps to control hydro-mechanical systems. The research discussed electro-hydraulic control valves for intelligent excavators. Given that ocean hydraulic crawlers have the same functions as the intelligent excavators, they are constructed with similar working characteristics as the excavators. The NFC is responsible for the control flow rate of fluid pressure at the orifice center-bypass line in the main control valve. This NFC has notable limitations which includes low fuel efficiency and bad controllability. Algorithms were implemented for position control and remote-control systems were used to control the robotic system.

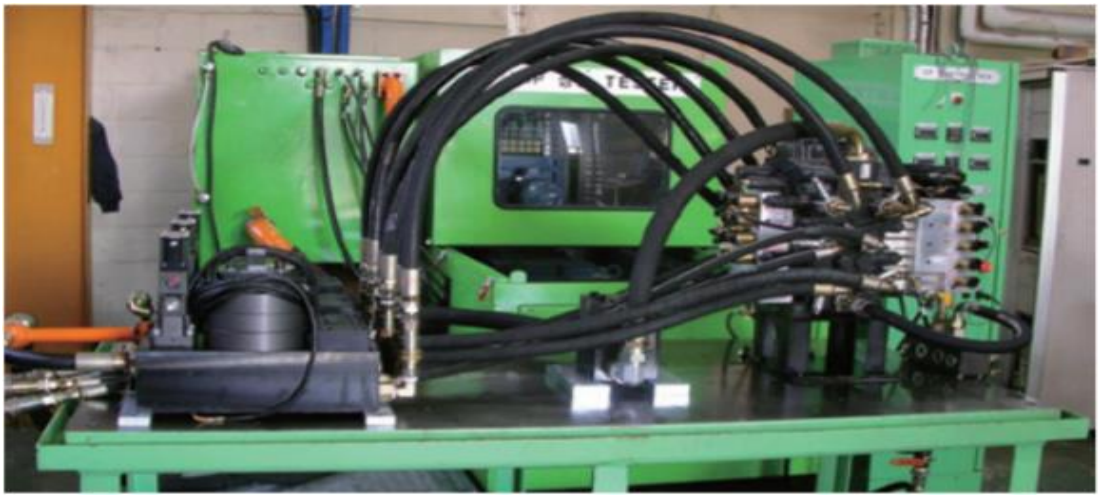

Figure 2.6: electro-hydraulic control valve system for robotic excavators (Kim et al., 2009)

The test system for the electro-hydraulic control valve, which can be controlled through wires or wirelessly, is shown in Figure 2.6. This mechanism can be operated in a variety of ways, including the use of an electric servo system to control joysticks and pedals directly, and employing numerous blocks of Electro-Proportional Pressure Reducing Valves (EPPRV) to provide a pilot pressure for the valve spool control. The E-MCV system was put to several tests in this study. These tests included features of the loading and unloading conditions. The system behavior was determined for the spool(s) operating under specific conditions, and statistical characteristics for the dynamic control valve system. The input signals to the control pumps were changing, which had a negative impact on the fuel efficiency and manipulation. As a

result, the pump's discharge flow rate was calculated in the simulation and then turned on the test bench, which enhanced the flow efficiency.

2.4.5 Safety Valve

According to Vijay & Site, (2019) the flow system of safety valve, which energizes fluid, provide a flow path for a flow of hydraulic fluid from its source to the hydraulic system. When de-energized, the valve blocks flow from the hydraulic energy source and vents the hydraulic system into the tank. On his research, he stated that hydraulic controlled valve consists of the main vale unit and hydro-cylinders. It was further discussed that hydraulic safety valves have some notable disturbing issues during conducting air link test in re-heating circuit performance for boilers-I. Air was forced through the safety valve and the circuit could not hold the working pressure during the pressure test. The valves need to be in close loop/gagged during conduction of the hydro test of the Langmuir probe LP. (Yi-Cun, 2020) discussed hydraulic safety valve as a component that ensures support for overload protection which supports the structure of hydraulic flow. It was further discussed that pressure on roof caused by large drops at low-speed flow (0.005-0.05m/min), can cause cavity on the hydraulic control arm in the closed loop. The paper demonstrated a practical relief for closed pressure holding fluid. Hydraulic oil flowing in specific direction holds for some time after the pressure drops, the reflection opens and closes for the flow of the liquid. A test system for the high pressure and low flow test system for safety valve was designed. A unique technical approach using straight line drive was used to push the safety valve plungers' cylinder to realize high pressure and low flow rate of liquid supply. AMESim simulation was used to develop a virtual prototype for the test system, further simulation and analysis were carried out to determine the main parameters and influencing rules of the rigidity of the liquid supply velocity.

2.4.6 Hydraulic Hosepipe and fittings

Hose assembly tips, (2019) described hydraulic hose pipes as synthetic rubber tubes surrounded by some sort of flexible strength enhancing winding such as metal or fiber, which are finally converted into another rubber carcass. In other words, they are interlinking channels that are used to pass and direct hydraulic fluids. Hydraulic fitting are used to fasting the pipelines to the hydraulic system. (Hyvärinen et al., 2020) stated that the failure of hydraulic hose for mining and other industrial operation are mainly caused by violent vibration, which increase the cost of maintenance. This research aimed at the dynamic behavior of hydraulic hoses. The paper further discussed the fundamental elements in obtaining fluid-elastic analysis for pressurized hose with conveying fluids. Experiments were performed to determine possible numerical methods for analyzing hydraulic hoses. The hose was pressurized and monitored with in-hose-development to test cell loads. The result was linked to a complex coupling system. The internal pressure observed when

the hose is deformed resulted in increased pressure during the operation of the ocean crawler. It was further discussed that different parameters tend to influence dynamic hoses; this includes the end point stiffness with larger influence on the balancing pressure on the dynamic behavior. Su & Bao, (2012) demonstrated a concept for large deformation of hydraulic hose pipe diameters infused by pressure. This paper investigated the fundamentals parameters of physical pipe walls, which concentrated on the mathematical modelling of hoses by their lumped parameter. To achieve the aim of the research, oil under constant pressure was passed through a pipe and the flow valve was simulated using Simulink software. The impact of the pressure was shown during the simulation to determine the changing pipe diameter and length. The result obtained from the simulation was used to establish the hose model and references for another related research.

2.4.7 Hydraulic boom arms

This arm operates by forcing a cylinder to move, using high fluid pressure generated by a pump. The fluid is permitted to enter the cylinder when the direction valve is opened allowing directional flow to occur, thus forcing the fluid to travel either up or down, depending on the optimized level of control. According to Haga et al., (2001), the main three parts of the hydraulic ROST excavator are:

a) The undercarriage,
b) The upper structure
c) The front attachment.

It was explained that the upper structure is responsible for the rotation of the undercarriage. The backhoe front attachment of the hydraulic ROST ocean excavator consists of three major components: boom, arm, and bucket.

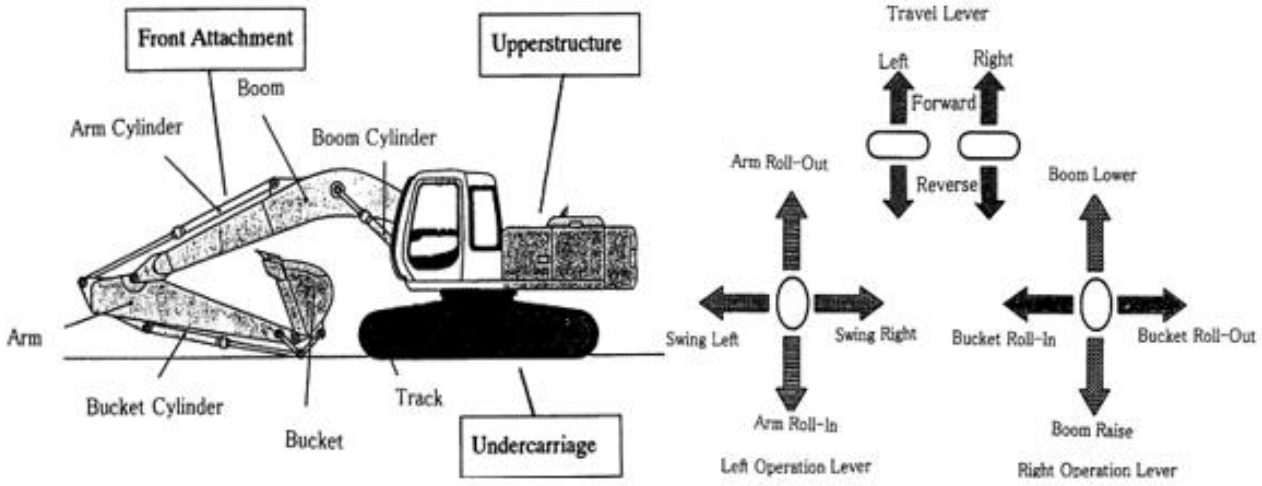

Figure 2.7: hydraulic ROST excavator with fundamental part and hydraulic leveler control pattern. (Haga et al., 2001)

Figure 2.7 shows the ROST excavator's operational control system and its structural configuration. According to the author, the leveler was fitted as the operating cab in order to automate the operational system and enable it to boom to specific degrees, arm control, bucket, swing, and travel. The bucket teeth tips are to be positioned to a depth of 30 cm, and the standard boom height auto control method is used. The hydraulic machine was meant to transition from a manual to an automatic operation, yet this system might be inconvenient and unpleasant during operation.

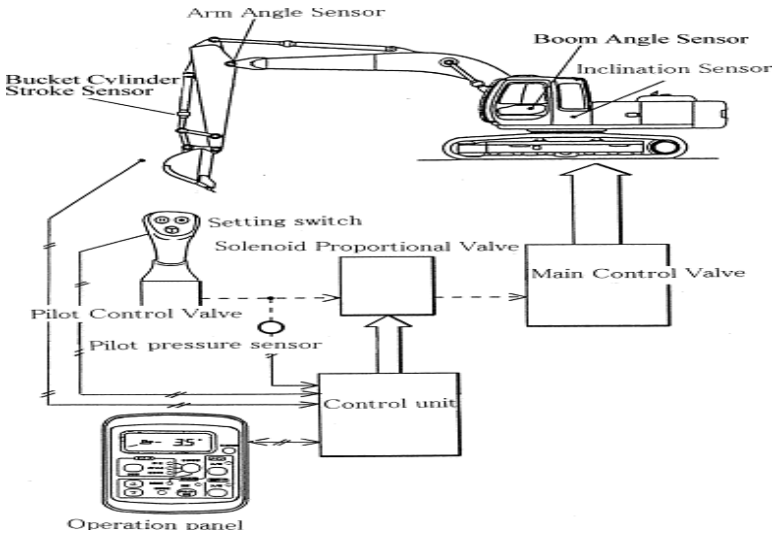

Figure 2.8: hydraulic excavator control system (Haga et al., 2001)

Figure 2.8 shows the hydraulic excavator's operation control system, which uses boom arm sensors to determine the boom arm's mathematical angle to the upper structure. It was discovered that the aim angle sensors on crawling excavators are mostly utilized to determine the angle of the arm to the boom. The bucket cylinder sensors are employed to determine the crawler arm's stroke length, which is controlled by the pilot pressure sensor that monitors operating signals. A sensor was installed to detect the upper structure tile for back-and-forth motions, estimating the angle of inclination. It was reported that the operational panel, setting switch, and a solenoid propositional valve was attached to reverse pilot pressure in this research.

2.4.8 Hydraulic Camshaft

According to Ray Bohacz & successful farming, (2019), camshafts in hydraulic systems are responsible for the timing, lifting, and duration of valve stays that are opened or closed. It does so by using the intermediate component of the valve lifters' pushing and rocking arms in the cam block. The systematic mechanism of a camshaft valve lifter was explained by (Venter & Sabunet, 2017). According to the article, hydraulic valves are made to have minimal but ideal clearance between the valve stem and the cam follower.

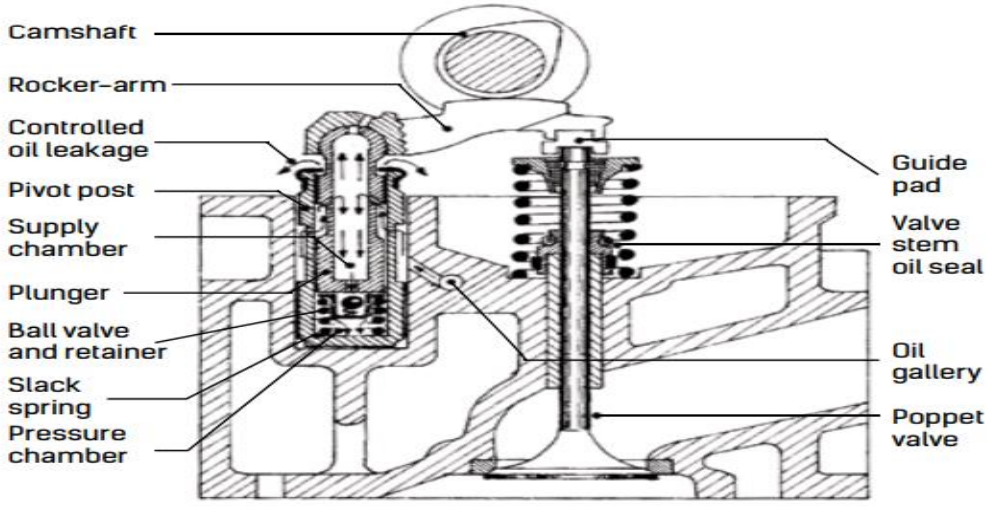

Figure 2.9: engine valve assembly (Venter & Sabunet, 2017)

The basic operation of the engine valve is explained in Figure 2.9. It was discovered that for camshaft engines, it is necessary to change the shim that is used to adjust valves on a regular basis. For the correct shim thickness, the valve was experimented with and documented. The valve spring of a hydraulic engine valve tends to return a reverse driven piston upward when the valve is closed. According to the description, the pressure was generated to open the ball valve, allowing fresh oil into the chamber beneath the piston. The camshaft has a tendency to apply pressure to the ball valves, preventing the oil from exiting. Since oil is incompressible, during operation, lifters are utilized as solids to transfer motion in hydraulic valves. According to the author, this system has several fundamental issues, including late circulation of hydraulic oil from the under-piston due to feed blockages or low pressure, wear out of valve lifters due to lifting, and tiny holes that are too small to feed in dirt. These tend to cause hydraulic pistons to seize up channels, resulting in blockages.

Table 2.1: problems pertaining availability, utilization, and installation of mining plans

tasks	Details for performing tasks
Identify the ocean floor adaptability and condition using remote operated vehicles or any available tools for observation.	Observable ocean floor conditions include profile of the ocean bed, rock characteristics to be mining using ocean dredging crawlers, setting up the excavation process, distribution of minerals, calculation and consideration of water depth, ocean environment and sustainability.
Using considerable technology in the Utilization and high availability of systems.	Maintenance of current mining equipment used or to be used in the mining operation, accurate preparation of the mining environment and observation of geological conditions, visibility of the current production rate using high-tech mapping and observation equipment, and product rate reliability for continued extraction and distribution.
Material handling on board vessels and further transportation for processing on land-based installation.	Using hydraulic subsea crawler for extraction as current technology state, process monitoring and separation techniques, ore conservation.

According to Yoon et al., (2012), there are three key ocean bottom mining operations: crawler collection of products or sucking minerals; lifting using dredging pumps; and finally aboard treatment, which includes separation and processing. These processes can be carried out with self-propelled seafloor mining tools that are connected to flexible conduct and buffers, lifting pumps, pipes, and finally, mining platforms that include various operations such as a control room, pilot plant, geological mapping and operations, pump control, electrical system plant operation, and product collection. In this paper, the distinguished researchers talked about their self-propelled dredging robot, whose tracking mining path was a key accomplishment for mining continuity. Further discussions highlighted the track velocity control in a remotely operated mining robot. The velocity system for the control is realized by the PI controller from gain tuning formulas which are based on model identification. This underwater mining robot Minero (KORDI) machinery parts for dredging application is a hydraulically operated system, has a configured framework structure, buoyancy system identified, and electronic and real-time operation software system. Its hydraulic system had a Hydraulic Powered Unit (HPU: 3KVAC, 134kW). It had a control value assemblage, an oil reservoir, a pressure compensator, a relief valve, filters, and a pipe.

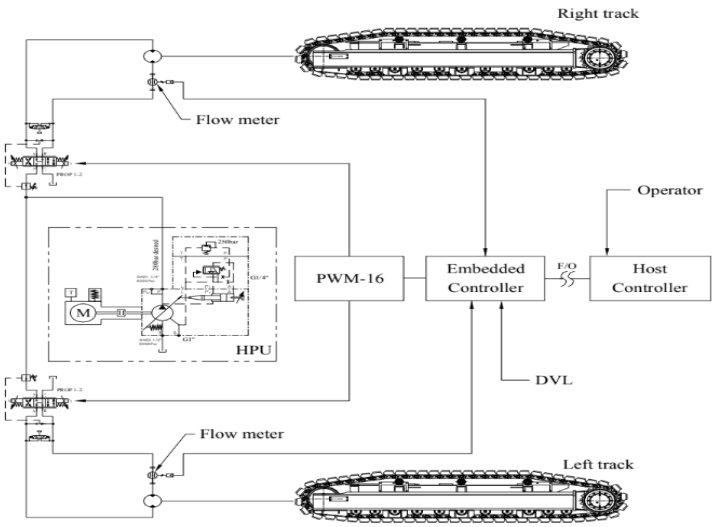

Figure 2.10: tracking control system for hydraulic powered ocean crawler (Yoon et al., 2012)

This tread tracked chain link control system, shown in figure 2.10, is on the MINERO (KORDI) and is designed for traveling on soft soil. The dynamic drive traction system is made possible by hydraulic motors, control valves, controllers, and a turbine-type flow meter. Yoon et al., stated that the design component is made possible by the body track shoes, driving chain, hydraulic motor, with reduction gear, idler and rollers, and framework construction. Tae-Kyeong Yeu et al.,(n.d.) Discussed the two navigational algorithms, which are reckoning and the extended Kalman filter (EKF), based on robotic kinematics. In the major parameters, it was stated that the kinematic velocity at the center of mass and the slip angle are calculated from the velocity of DVL and yaw-rate time.

Figure 2.11: concept of a crawler test on the ocean floor (Tae-Kyeong Yeu et al., n.d.)

figure 2.11, is a self-propelled South Korean mining crawler that excavates valuable minerals using a kinematic operation on extremely soft, cohesive soil. The skid-steering had the ability to estimate its position at sea. Outlining its differential systems, which include inner track slip, outer track slip, and slip angle, allows for these slips.

Ocean mining crawlers are more reliable and effective when the potential dynamic drive system is figured out based on it means of operation. In figure 2.12 below, the track vehicle performance, shows a kinematic model in a x-y coordinate system. This figure shows the relationship between certain angles and the differential drive parameters in the system based on the coordinate system.

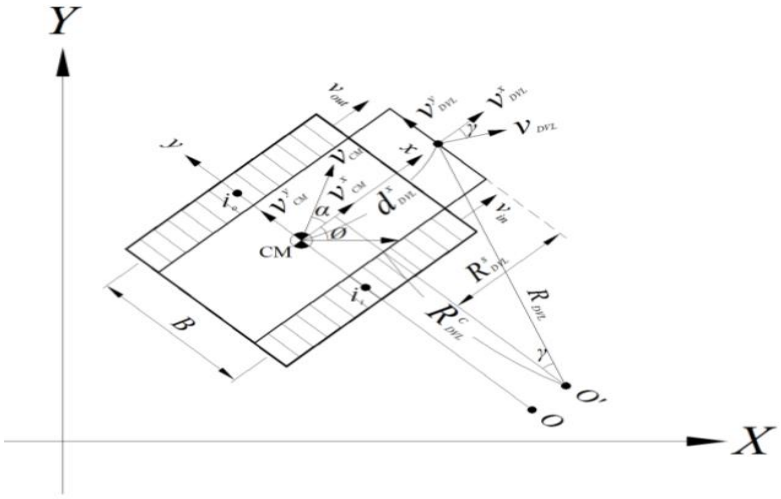

Figure 2.12: kinematic model of tracked vehicle in x-y coordinate system (Tae-Kyeong Yeu et al., n.d.)

As described in the diagram above:

- The angle ∅ is the concentrated heading direction.
- α is the direction of the ship angle.
- $0'$ is the fixed instantaneous centre of rotation.
- CM is the fixed centre of mass for the ocean crawler robot.
- B is the tread track for the driving system.

The ocean crawler velocity shown in figure 2.12 is defined as:

- V_{0ut} (t) and V_{in} (t) are used to demonstrate the velocity of the crawler out track drive system and the inner track drive system.
- i_o (t) and i_i (t) are the slip for both track drive system of the crawler as shown in figure 29

These equations are further combined and expressed as demonstrated by A.T.Le (199) and (Tae-Kyeong Yeu et al., n.d.), which is proposed by the following kinematics equations.

- $\dot{X}(t) = \frac{\frac{1}{2}\{V_{out}(t)(1 - i_o(t)) + V_{in}(t)(1 - i_o(t))\}}{\{\cos\emptyset(t) - \sin\emptyset(t)\tan\alpha(t)\}}$ ---------- equation (1)
- $\dot{Y}(t) = \frac{\frac{1}{2}\{V_{out}(t)(1 - i_o(t)) + V_{in}(t)(1 - i_o(t))\}(1)}{\{S\ln\emptyset(t) + \cos\emptyset(t)\tan\alpha(t)\}}$ ---------- equation (2)
- $\emptyset(t) = \frac{\{V_{0ut}(t)(1 - i_0(t)) - Vin(t)(1 - i_i(t))\}}{B}$ ---------- equation (3)

From the assumption that the effect is very weak at the bottom of the crawler, the analog or digital operation (fluidics) effects can be ignored using these math equations. According to the researchers, the ultra-short baseline (USBL) is the main channel that allows underwater navigation to be possible for its location data. According to their final assessment, which was based on key decisions due to the conditions that the navigation system encountered underwater, most sonar systems have measurement errors of up to several meters while the drive system is in motion and delays of several seconds. The kinematics of the system are captured by inertial sensors and EKF. Hydraulic crawlers were examined by Nazaruddin Nazaruddin & Gunawan, (2015). The undercarriage is an essential part of heavy-duty equipment. It also contains other components necessary for the movement of the excavator.

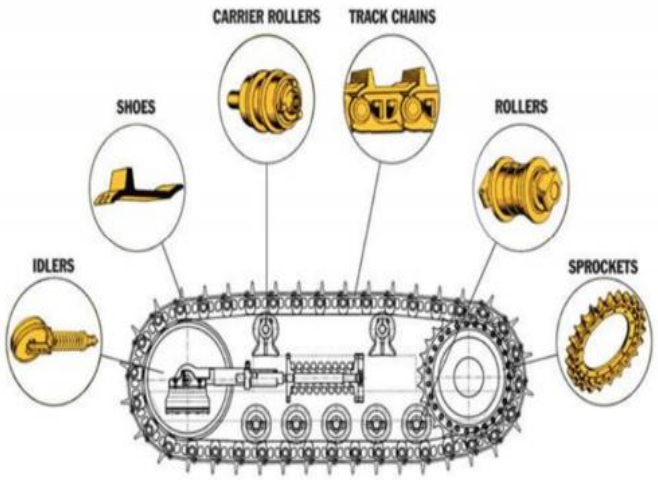

Figure 2.13: crawler drive tracking undercarriage unit (Nazaruddin & Gunawan, 2015)

Figure 2.13 shows the essential parts for the excavator drive system. This consists of several components responsible for autonomous movement. The undercarriage includes a sprocket, final drive unit, track shoe, carrier roller, track frame, track chains, and a front idler. Among these, the final drive unit has key functions

like transmitting power from the engine and increasing the torque for the entire track automation. This paper stated that the transmission for the arrangement is powered with a low speed of 3.6 km/h and a maximum speed of 5.5 km/h as a result of a generated motor-driven rotation of 2000 rpm.

(Yoon et al., 2012) studied the characteristics of hydraulic crawler drive track systems. The study detailed the implementation of velocity control on an ocean crawler drive tracked system, which was on the robot's mining path. The basic method for velocity control and the properties of the track system, which are still being explored, were extensively described. The ocean robot first executed a shallow water test to ensure efficient clarity in roving crawlers on the seafloor. In order to save time while constructing the control system for this crawler, the robot was suspended in the air by a crane to determine the basic time measurement of the control and establish a fundamental relationship between the input Pulse Width Modulation value (PWM) and the output flow rate from the flow meter in the dynamic drive track system. For measurement and control systems, it is crucial to understand the sample time definition. It was also stated in the paper that the application of commercial robotic sensors in hydraulic crawlers is limited by waterproofing and pressure resistance technologies. If the sensor is accidentally exposed to seawater, the crawler's performance will be significantly affected. The relationship between the RPM and the flowmeter, which is supplied by the manufacturer, is used to calculate track velocities. It is critical to model the vertical rise of a dredging pump; these centrifugal pumps are connected to an exploration crawler for product suction to the ship. According to Keisuke et al., (2015), the ocean dredging robotic crawlers are equipped with large drills that allow minerals to be deposited horizontally. The Horizontal Mining System (HMS) is used for the extraction of ore, which is classified as natural rock or sediment that contain one or more valuable minerals which vary by size. This implies that the subsea crushing feeding unit (SCFU) ensures that slurry transportation is used for traditional riser systems. In this paper, three concepts were analyzed. These include Vertical Mining Systems (VMS), Down-The-Hold drill (DTH) and unit mount on a jack-up platform. It was stated that vertical mining can be used for both exploration and subsea mineral deposits. The DTH makes ocean mining operations more efficient by loosening the ocean floor. The experiment demonstrated the transport of ore slurry directly through the traditional riser/pump system. Using the HMS, the concepts allow dredging crawlers to explore up to a maximum drilling depth of 30m to 50m. This research paper advocates that the mining speed for dredging ore per DTH is determined by the drilling diameter and the drilling pressure. The drilling pressure is related to the speed which depends on the dredging rock strength. This experiment was carried out using gravity type of jack system with XY horizontal sliding actuators which enables the positioning of the drilling system on the seabed. According to Arcangeletti et al., (2021) the increase in demand for ocean mineral extraction processing and the surveillance of the ocean floor, is driving development in ocean instrumentation and control systems. This

area of research is rapidly growing and awaiting the next generation of ocean engineering technology. ExxonMobil URC (upstream researching company) are optimizing autonomous subsea systems by re-designing robust electronic subsea equipment which include ocean crawling robots, ocean drones and ROVs. It was further stated that using systematic value engineering approach, the VPV equation, shows the relationship between technological advancement and economic progress. Manager & Ç Yavuz, (2009) analyzed a conceptual robotic arm and the relationship between the positions, velocities, and accelerations, of different links for the manipulator based on its projected application. In this research, a prototype robotic arm with 3 DOF was manufactured with a user interface for controlling the system. As part of the communication system, a software application was developed on a personal computer and used to send in control inputs through serial communication cables. According to the researchers, the robotic arm is further divided into two parts: forward kinematics and inverse kinematics. In the forward kinematics of a robotic arm, the length of each link and the angle of each link joint is displayed, and mathematical computation is done to determine the position of the robot in its work volume. In the project, the forward kinematics equations were solved by using homogenous matrices while the inverse kinematics equations were solved using the analytic methods and Jacobian methods.

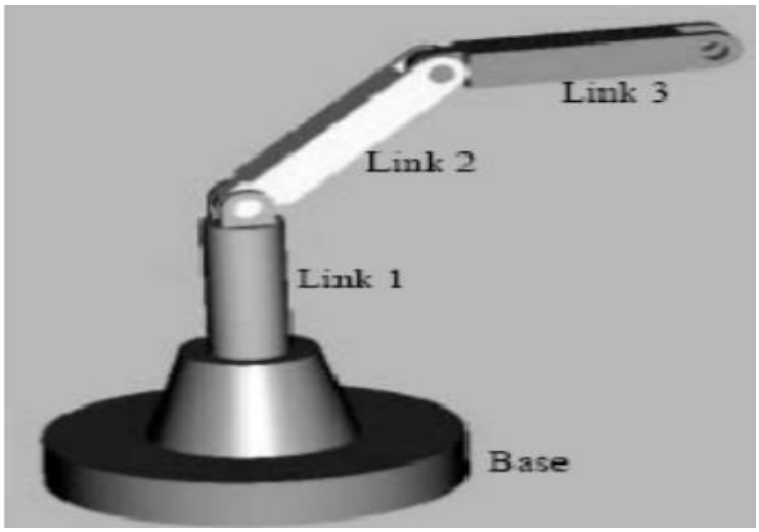

Figure 2.14: simple design of an open chain serial robotic arm (Hu & Meng, 2020)

Considering the open chain manipulator kinematics as represented in figure 2.14, the rigid bodies' link is connected by a revolute or prismatic joint. One end of this chain system is static, which is the base, and the other end (link 3) is represented as the end effector. These joints can be controlled individually by servo motors or DC motors. The resultant motion is obtained by composition of the elementary motion of each link with respect to the previous link of the robot arm.

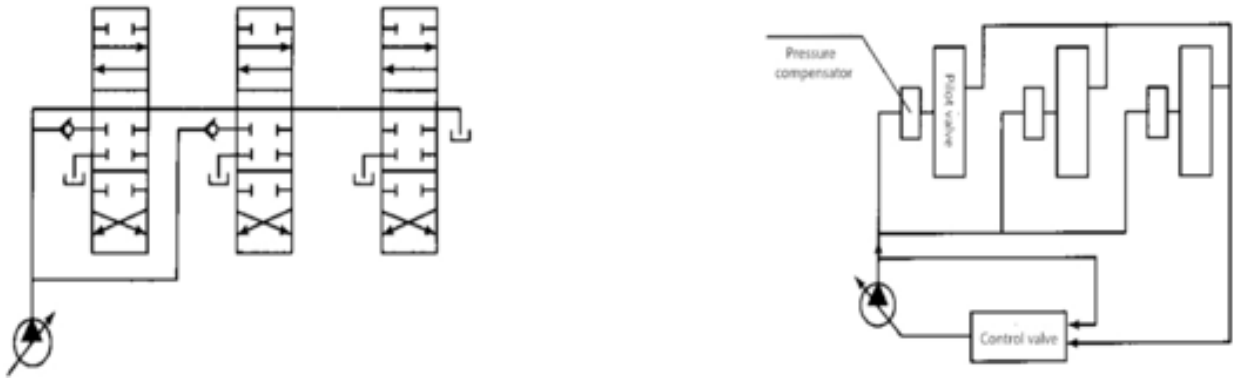

Figure 2.15: hydraulic excavator oil sight feed and oil supply for hydraulic system. (Hu & Meng, 2020)

(Hu & Meng, 2020) discussed the history of hydraulic excavators which started in the United States. Those excavators were powered by steam engines. Common hydraulic systems and their oil supply system are represented in figure 2.15. According to the authors of this paper, the working principle of most land mining and offshore hydraulics powered excavators depends on pressure distribution in the hydraulic fluid which is used for control. These hydraulic systems exchange directional data under the action of the high-performance flow sharing Load pressure independent flow distribution LUDV systems. Hu & Meg in 2020 further stated their design approach for hydraulic powered devices. Their design approach involved the following variables: frequency, brakes, change in direction, and change in external load, bad working condition, bearing shocks and vibration. In conclusion their approach was proven to be highly suitable for real world working models in ocean applications.

2.5 Characteristics of hydraulic machines

1. Operating mechanism and transport requirements
2. Mechanical design
3. Structural strength
4. Economic standards

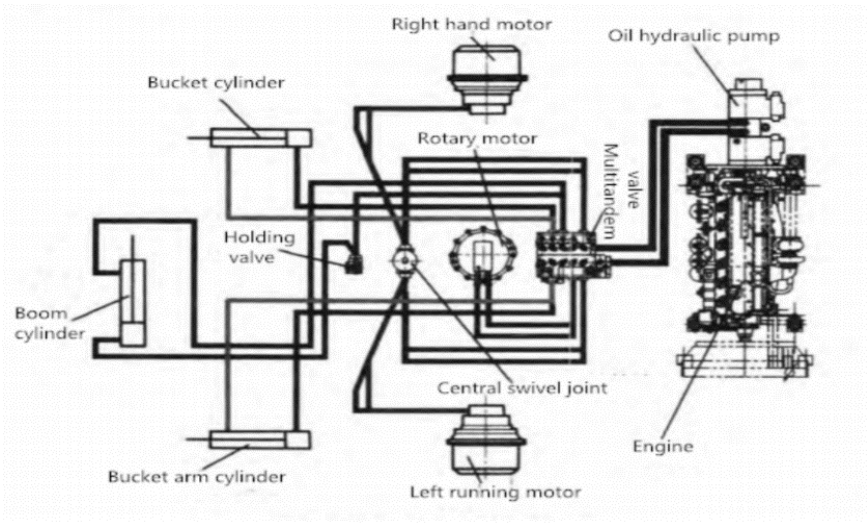

Figure 2.16: excavator hydraulic system operational diagram (Hu & Meng, 2020)

Figure 2.16 above shows a detailed design of a hydraulic drive, arm system and their mode of operation. The researcher analyzed the working principles in parallel with a standard excavator in the mining environment. The system illustrated details about power and force requirements for hydraulic action. During operation, power and oil is hydraulically supplied to each component. We can see in figure 2.16 that the oil hydraulic pump is responsible for forcing hydraulic fluid to the valve multi tandem. This further distributes fluid through pipes to the mid rotary motor, right motor, and left motor. The holding valve after resaving hydraulic fluid holds the force fluids pumped into the bucket cylinder, bucket arm cylinder and boom cylinder. The excavation resistance mainly comes from its resistances, which is further decomposed in the tangential direction and normal direction as represented by F1, F2 in equation 1 and equation 2 respectively. In the former, it is perpendicular to the tip of the tooth and later tangent to the tip of the tooth.

$F_1 = k_0 wd$ ---------- equation (4)

$F_{2=\varphi F_1}$ ---------- equation (5)

- k_0 is represented as the mining specific.
- W is the mining depth.
- φ Is the mining resistance to it coefficient

According to Arcangeletti et al., (2021), hydraulic powered subsea crawlers or underwater crawlers are mainly launched from a mother ship which is used for ocean mining of useful resources from the sea floor into the mother ship. This is possible by using pumps and flexible pipes which convey the products into the

ship. It was further stated in this paper that hydraulic crawlers are operated though special custom-made umbilical cables which are connected to the control system in the mother ship. This crawler's movement are mostly translational and rotational along the sea floor.

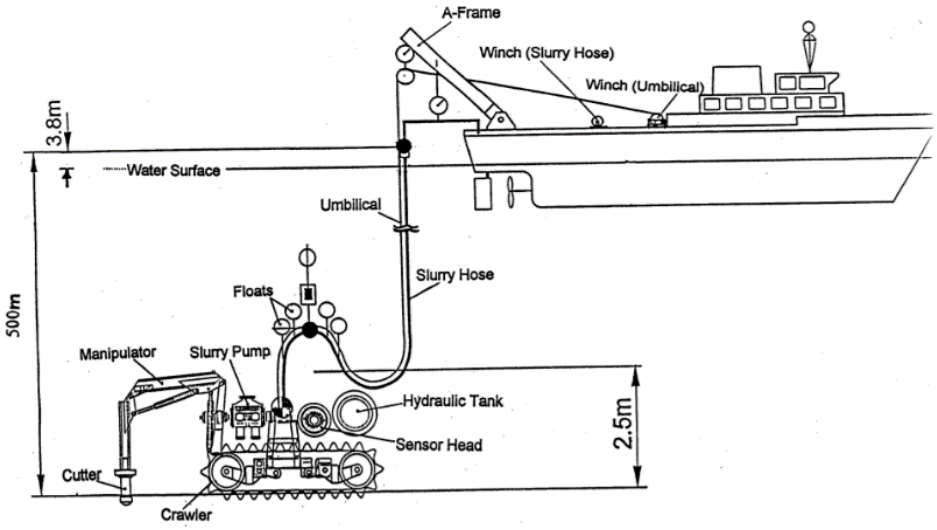

Figure 2.17: underwater mining crawler alongside a mother ship (Arcangeletti et al., 2021)

A sketch of an underwater mining ocean floor crawler is shown in figure 2.17. The ship's movement is controlled by a joystick. The umbilical cable uses a fiber optic wire for communication. The underwater crawler's location was tracked by an acoustic short base line system. The velocity was determined by another acoustic system. The Doppler log, temperature and pressure were monitored by a transducer in this study. The PC-104 is the "brain" of the crawler's control system, which is based on the ship's bus data system. The acquisition card sensor was communicated with by the ship's computer systems, which used the RS-232 protocol. RS 232 on the fiber optics operating system is based on the QNX data and was controlled through the MULTIPROG software for no data. This crawler's positioning system was determined by Global Positioning Systems in the ship. Some inbuilt transducers are used to measure various parameters to enable the crawler accurately to carry out its motion and dredging capabilities. In this research, (RTD) Resistance Temperature Detectors were used for the measurement of the hydraulic circuit parameters in different locations. The cardan joint angle of this crawler was measured with a tilt transducer. An absolute pressure transducer was used to measure the ambient pressure. A power transducer was used in measuring the true electrical power delivered to the pump motor. The concentration measuring system was implemented using the gamma ray-based slurry. The Linear Variable Differential Transformer (LVDT) was used for the measurement of the positioning potentiometer for the angle measurement on the manipulator. The altimeter was used to measure the distance from the ocean surface to the ocean floor. Magnetic switches were used for the measurement of track velocity or drum speed. Short base line acoustic positioning system was used for measuring the crawler's position with respect to the ships direction. The

motion sensor was used for the measurement of the heading direction. Finally, the Doppler log was used for the absolute measurement of the velocity. This paper gave a detailed report of the instrumentation aspects of the shallow water mining system using ocean crawlers. (Hunter & Richard Joseph, 2007) stated that 75% of the earth surface is covered by oceans. These oceans are embedded with bountiful natural resources that can be explored. This study discusses the historical laws that relates to ocean mining. This act stated that the increase in ocean mining led to the establishment of the International Seabed Authority (ISA 2006) which was implemented under the United Nation convention laws of the sea.

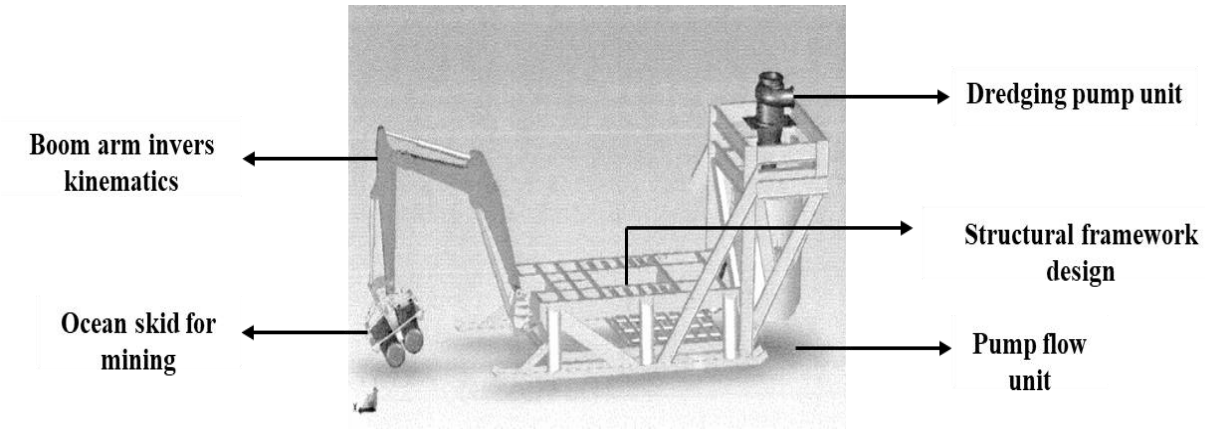

Figure 2.18: concept of the deep ocean sampling (Hunter & Richard Joseph, 2007)

Figure 2.18 shows a detailed illustration of the ocean sampling skid and its characteristic function in deep-sea mining. According to the authors, the post-detection telemetry subsystem PDTS was designed and developed for a test platform that was used to monitor cutting forces and collect the cuttings. In the process of achieving this, a subsea skid was mounted on the conventional ocean remote operation vehicle (ROV), which was more appropriate than the self-contained unit. The DOSS was designed as a tele-remote unit that was mounted with multiple cameras for the crawler command and control system. The DOSS is a well-designed tool that is equipped with a full-featured all-around sensor and data acquisition system. Convergent robotics was used to develop the data management software interface, which included the logging and control software systems. The platform, as well as the material handling system, were designed considering the mechanical structure. The equipment were visible with the help of optical ocean clarity, which allowed the tele-remote operator to evaluate the dredging performance over time. Hunter & Richard Joseph, (2007) discussed a research investigation on ocean underwater tracked vehicles with a ladder trencher. They also discussed the mechanical design for the autonomous operation of the tracked underwater vehicles that are connected with a Ladder Tendier (LT).

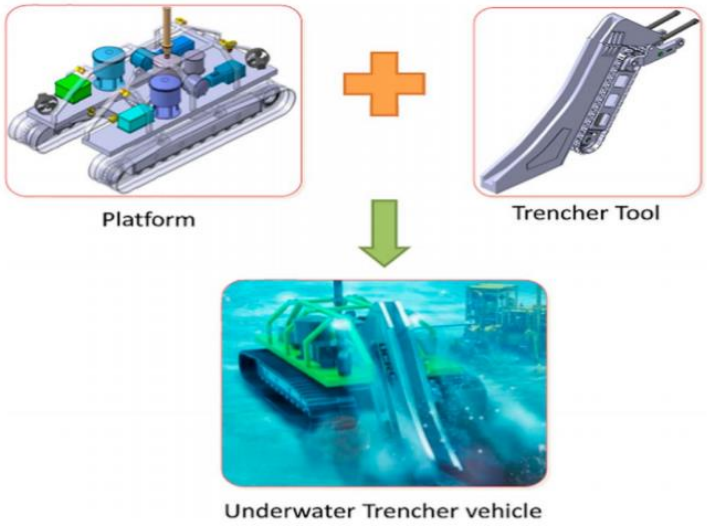

Figure 2.19: trencher excavator platform (Hunter & Richard Joseph, 2007)

Figure 2.19 shows the arrangement of a hydraulic system platform, a trencher product drive system, and a combined system of the two images. The trencher cutter bar I press applies force to the ocean floor's surface, allowing the drag cutter tool bits to make contact. The purpose of this study was to determine the force of a drive cutting tool installed on a trencher tool, as well as how the tool's assembly impacts the moments and force operating on the cutter. The normal force was demonstrated by calculating the thrust cutter's penetrating force efficacy. According to the analysis of the LT's force and moment, the movement of the trencher tool is a nonlinear coupled dynamic system that allows movement beneath the ocean floor. It was shown that the forward tractive drive thrust of a given type of ocean ground vehicle is usually represented by the net traction of the two-way wheel or crawler dynamic drive system. Fluid dynamic resistance on the traction system of ocean vehicle technology is referred to as "drawbar pull" in this article. The reverse capacities of ocean vessels on their pull, push, or climb slop drive systems are determined or measured using this technology. In other words, multiple types of vehicle pull systems exist based on the ocean ground condition, the vehicle traction system's gearing, and whether the load power is provided by an electric or hydraulic drive system. (swire seabed, 2008) discussed a detailed fundamental analysis on the seabed excavator which has multiple tool carriers for different ocean operations and dredging.

Figure 2.20: hydraulic ocean crawler (swire seabed, 2008)

Figure 2.20 illustrates the design equipment for a seabed excavator that has the capability of dredging up to 2500 meters of ocean depth. This ocean driving and extraction vehicle is delivered with a Kongsberg Evotech active, which is designed with a stable compensator launch and recovery system (LARS). The ocean vehicle was designed in such a systematic way that it can be launched and appropriately recovered in waves with a height of up to 4 meters. The dredging mechanisms have the capability to run high-power we-ocean ejectors up to 16 units, providing 4800kg/h through the ejectors. The automated ocean crawler excavator is a Swire Ocean robust crawler that is designed with competent structural hardware and software based on a Perry Slingsby XLX ROV, combined with a Kaiser Excavator body and a Wesubsea Titanium dredging system. This piece of equipment was created to work in a specific area for subsea excavation under specific operational conditions, such as ocean excavation and dredging, decommissioning removal, and relocation of drill cutting and rock dumping, cargo loading into baskets or containers, and the removal and recovery of ocean structures. It is also used for cutting and grinding, scour protection, ocean floor drilling well centers, spud operations, seabed sampling, and the removal and recovery of ocean structures (D. Reibbit & Hanson Aggregates Marine Ltd., n.d.). They discussed environmental consent that allow ocean dredging in a production-licensed area to take place. Before obtaining a license, governing agencies in mining countries (such as the Marine and Fisheries Agency/Marine Management Organization in England and the Welsh Assembly Government) conduct a thorough environmental impact and research study. The geographical mapping region that can be explored, as well as the mining period, are determined by government issued licenses. According to the document, the maximum tonnage that can be excavated in a single year must be adhered to in accordance with the regulation. A conditional authority specified by regulating management, mitigation, and monitoring controls is often used to grant instructional permission. The details of the vessel's EMS must be examined and certified by offshore management agents of the royal

estate before any modified or factory-built vessel for dredging application in a crown estate licensed excavator area for operation in any parameter**.** The first stage for dredging companies in this category is to get an ocean mining license. This is done by submitting an EMS information sheet to the offshore management agency that includes a well-detailed important feature of the EMS configuration. This includes information on the principal type and quantity of excavation status inductors utilized, as well as detailed information on the other components. The outcome of the data test must be transmitted from the vessel to the satisfied party to finalize the information for this certification to be issued. Once the vessel's EMS or action is functioning properly, an approval can be granted. It is critical to provide a detailed subsea excavator specification to guide us through our electrical subsea crawler conversion.

Table 2.2: Ocean crawler's excavation specifications, recovery procedures, dredging capabilities and tooling interface (Swire Seabed, 2008)

Ocean floor dredging specification.	**Ocean floor lunching and recovery procedures.**	**Extraction capacities of product.**	**Seabed tooling interface for recovery.**
Ocean depth rating 2500m	Controlled using electric drive systems.	Ejector system sizes 12, 14, 16	Auxiliary HPU: pressure: 3200 psi. max flow: 95 L/pm
Power pack system 150HPU.	Controlled operation using active heave compensated winch system.	Operative water pump system 2 x 135kW.	Operated using 360°rotor on the boom for tolling operation system.
Operate speed forward.	DNV 2.22 operation certification	Max capacity 4800m3/h flow inside	Easy for quick connection for tool swapping operation.
Speed lateral: 1+ knots	24.5/14Te SWL (dry weight system)	Back flushing system for unclogging.	Operation includes hydraulic for tooling operation.
Weight (dry/subsea): 14/10t	2.4m/s on winch (inner layer)	External cooling pump to increase reliability for nonstop operation.	Breaking ocean floor jetting nozzle: 10 bars at 3400 Lpm (7 bar at 6000 Lpm)
Controller standard arm: 5m (extended nozzle can be mounted)	Tow fails safe disc brakes.	–	Drum cutter system include for operation.
Deck area: 100m2 required	–	–	Diamond wire cutter, circular saw, 3 in 1 bucker, dredging nozzle, normal scoop bucket (1.2m wide), and other tools as required.
Lifting capabilities: Approx.1500kg on full boom extension.	–	–	–

Under specific ocean circumstances, ocean mining crawlers are guided by standard procedures. Table 2.2 displays some precise specification that should be taken into account when designing ocean crawlers for dredging. The crawler should be equipped with some operational sensors, such as a gyroscope and a fluxgate compass, as a minimum level of functioning. The fluxgate compass is a highly permeable electromagnetic device designed to carry two or more smaller coils around it. The horizontal component of the earth's magnetic field is sensed using an ocean bottom extraction crawler. The Pitch roll sensor is used for the measurement of movement and orientation, which provide an accurate heading. This sensor provides the ultimate precision in water level measurement. Obstacle Avoidance sensor (OAA) are intended to provide specific information about the underwater environment. These are the control system values for hydraulic vertical stacking designs with one to ten stations. This system is used to distribute LEDs and the energy required to power ocean lighting in order to illuminate the ocean floor. Kongsberg OE 15-100 near SIT camera are used for ocean view that sends back signals to the pilots. These systems are enhanced by the CCD camera which represents a background in non-intensified performances. On the other hand, the Kongsberg OE14-366 are a color zoom camera that are used for ocean crawler inspections as this system are mounted on the seabed excavators. (Seascape BV, 2017) is an innovation and ocean engineering developing company which has provided ocean solution by designing and building concepts of sea robot both for mining extraction, and other scientific reasons.

(Crawler & seascape BV, 2017) developed their first generation of a mini sized electrical ocean crawlers for subsea surveying, inspection, and cleaning. The project objectives were developing a system that can operate in tunnels, pipes and ocean floor which has a monitoring live camera and autonomous control system.

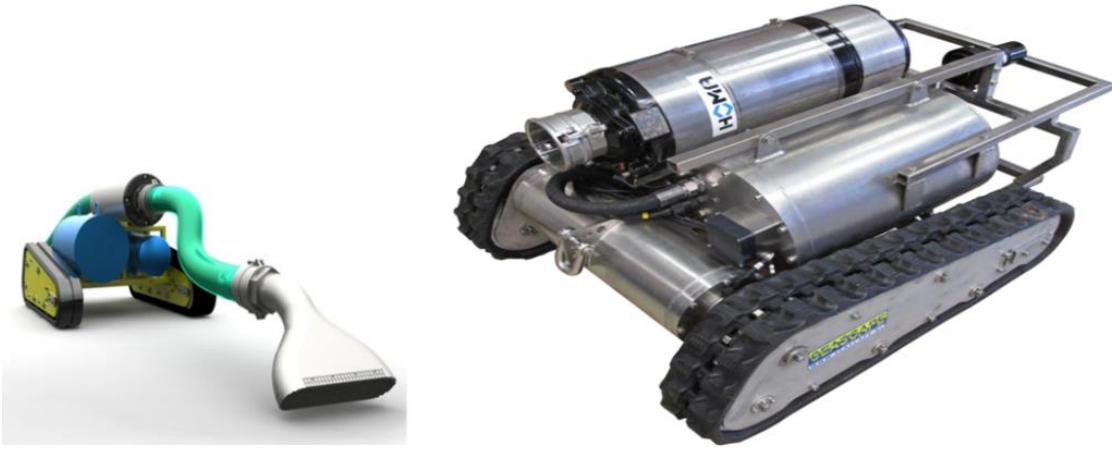

Figure 2.21: ocean crawling machine. (Crawler & seascape BV, 2017)

Figure 2.21 shows a design of a mini ocean crawler that has basic system capabilities of interfacing with all types of ocean sensors for different applications. This crawler's standard system for ocean intervention has an on-board 10 kW power supply for the dredging pump and other systematic operations as required for its application.

Table 2.3: Ocean crawler's manufacturing specifications

Embedded specification for operation	Mathematical unit and specification.
Crawler operating depth	40 meters to (optional deeper)
Operation umbilical cord	Length of 30 meter to 1000-meter neutral
Under operation, crawlers pulling force	Up to 100kg of pulling force
Payload for the control	150 kg
Weight of min crawler	250-400 kg
Dimensional size of crawler	1.2 x 1 x 1 m
Structural material	Stainless steel
Driving traction system	Rubber steels reinforce
Power supply	400 VAC @ 50 Hz 2-12 kW depending on tools
sensor	Ocean depth, roll/pitch, temperature, heading, DVL, USBL
Camera	2X HD zoom camera with LED light
Extra port	RS232 / RS485
Data information transmission	Gigabit Ethernet over fibre optics
Dynamic driving speed	1-1.5 km/ hours.
Control system	Joystick and GUI driving switching on/off on 2x HD monitor
Standard system	Dredging pump 10 kW.
Sonar	Scanning imaging sonar.

The mini excavator machine, which is embedded with a robust positioning system, has applications in ocean floor cleaning, fundamental research and ocean inspection, digital live monitoring, and control system. The main unit can be extended, and a scaled-up version is also possible, as shown in Table 2.3. With this specification, a scaled-up version of the crawler can be developed. According to (Seabed dredger & seascape BV, 2017), the second generational build of their ocean crawler is a hydraulic powered ocean mining crawler. The mining crawler was built with a multipurpose bottom tracking vehicle with facilitates the movement necessary for ocean exploration of mineral resources. Furthermore, it was stated that this machine is a remote-controlled vehicle, which can operate in narrow spaces as the mining operation is in progress. On the seabed dredger (SBD) a designed manipulator was mounted onto the exploration pipe and the water jet that is used for breaking the ocean floor was attached to the manipulator.

Figure 2.22: hydraulic dredger with 2DOF boom arm (Seabed dredger & seascape BV, 2017)

The hydraulic crawler seen above is used for mud and sand suction dredging. It is equipped with a soil jetting effective pump for freeing the ocean floor. A tilted camera is fitted on the crawler manipulator's pan, and the electric-hydraulic aggregate is hidden by a valve pod. The water jet pump is hydraulically operated, and the north gyro is housed in an electronic pod. The seabed dredger's communication system, which includes electronics, pressure transducers, and PLCs, is systematically managed by the panel on the surface control system. With a total traction force of 2500N and a working depth of 150 meters, this driven vehicle traction system was achieved. The seabed dredger was created for the following applications: trash removal, ocean drilling, exploration, ocean floor video inspection, ocean floor construction drive assistance and observation, hydraulic platform for underwater tooling, high pressure cleaning.

seabed dredging excavator & seascape technology BV, (2017) described their third generation of ocean crawler seabed dredging excavator, which was manufactured in their company. The developed concept was designed for large scale ocean exploration. The ocean dredger weighed 28 tons. This excavator is redesigned and modified to operate under the ocean for exploration. It was stated in this paper that an excavator was fitted with 4 electrohydraulic powered packs which pulls sufficient power supply of about 275 kW to power the dredging pump. Electric motors are responsible for driving the centrifugal dredging pumps. A jet-built nozzle which is driven by a 130kW jet pump was fitted on the end manipulator.

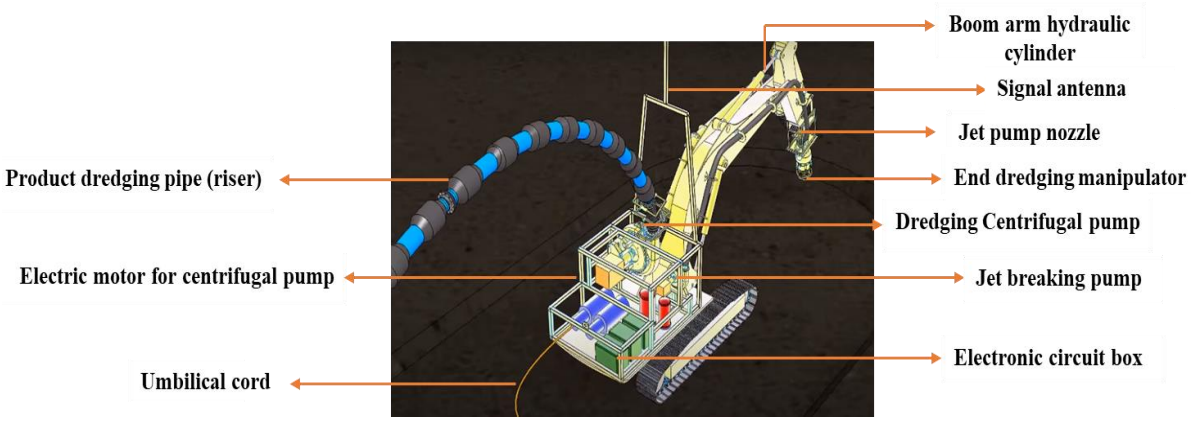

Figure 2.23:3rd generation seabed dredging excavator (seabed dredging excavator & seascape technology BV, 2017)

(seascape technology BV, 2017) further discussed that the SBDE is fitted consecutively with a monitoring sensor on its positioning system. This sensor was visualized with a 3D software. The positioning system of the SBDE is based on the GPS RTK antenna fitted on the head of the crane over the water level. Using the GPS on the crane, this crawler can only work within 10-meter ocean depth. This dredging model was embedded with a 100-meter standard pressure tight system and connected with a 400- meter umbilical cable that is tittered to the control transformer container. The electrical system was powered by a generator of about 100 KVA (400 VAC/60Hz). The SBDE uses a 12-meter discharge hose, and the mining dredger is fully operated remotely with 2 joysticks system for all boom arm movements and driving. The paper stated that the control system is operated through the Graphical User Interface (GUI) which is touchscreen. Some sensors like the scanning sonar visualizing device and profiling sonar scanning dredging parts were used in real-time during dredging. The SBDE is used for application such as, Deepwater dredging (max 3000 meters), ocean debris removal, ocean drilling, excavating, Deep-sea video inspection, ocean mining drive assistant and observer, hydraulic power platform for underwater tools, and high-pressure cleaning tool.

Dai et al., (2019), carried out a CFD simulation for non-negligent interference acting on ocean vehicles by surrounding water. They analyzed the fluid resistance on ocean vehicles which affected the torque.

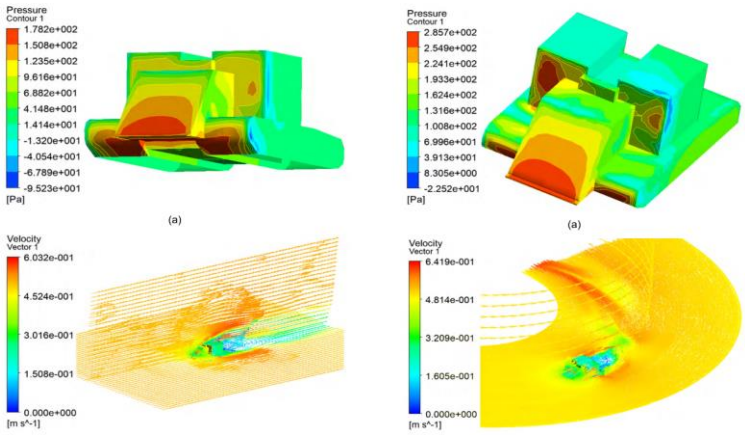

Figure 2.24: CFD simulation for straight-line/turning motion in fluid pressure and fluid velocity (Dai et al., 2019)

Figure 2.24 shows the results from the simulation of the straight line and turning motion of a submerged underwater vehicle. The fluid pressure and fluid velocity are systematically distributed round the vehicle a displayed in figure 2.25, The diagram A below shows fluid resistance on the vehicle and resistance torque acting on the body of the crawler. These values were obtained by loading five concentrated point on the Multi-Body Dynamic (MBD) deep-sea mining vehicle. This paper further discussed motion control model for the deep-sea mining vehicle. A conductive simulation was performed using the mathematical turning motion model:

$$e = \left\{\sqrt{(x - x_0)^2} + (y - y_0)^2 - |R| \times s_1 gn(R)\right. \text{---------- equation (6)}$$

$$\alpha = \theta - \frac{\pi}{2} \times \text{sign}(R)\beta \text{---------- equation (7)}$$

$$\Delta\theta = \theta - \theta_1$$

$$i = \frac{R+B12}{R-B/2} + \Delta_1 \text{---------- equation (8)}$$

The above equations show predetermined trajectories, combined trajectories by straight line and turning circular arc trajectories. MATLAB, Simulink and RecurDyn were used to determine the integrated motion system and total dynamic model for the mining vehicle. Monitoring modules were used to read and store dynamic parameters from the RecurDyn module system.

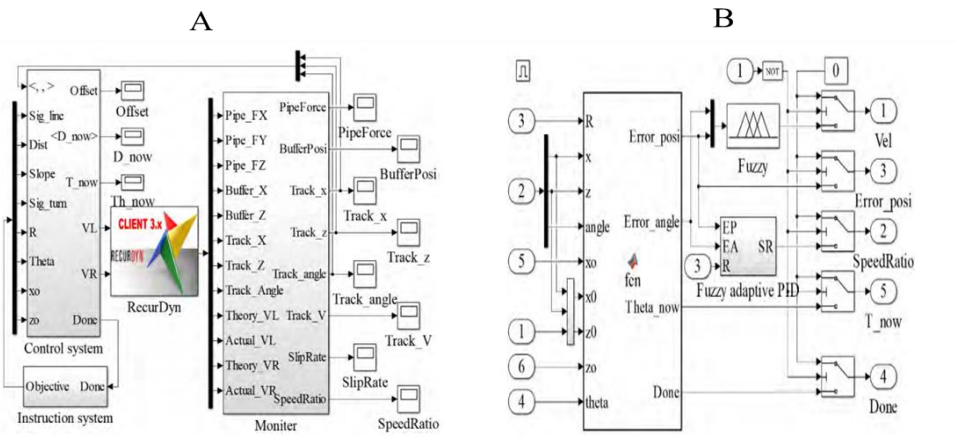

Figure 2.25: system and turning motion control module for crawlers (Dai et al., 2019)

In the above figure 2.25**,** diagram B is a representation of an ocean crawler turning module. The effect of vehicle-sediment interaction, fluid resistance factor, has led to high complexity in designing accurate models of ocean hydraulic crawlers. Hence the PID control algorithm with good performance has increased the speed ratio where the trajectories heading, and deviation are the variables. Wood et al., (2013) analyzed the initial design requirements for the RG-III remotely operated crawler.

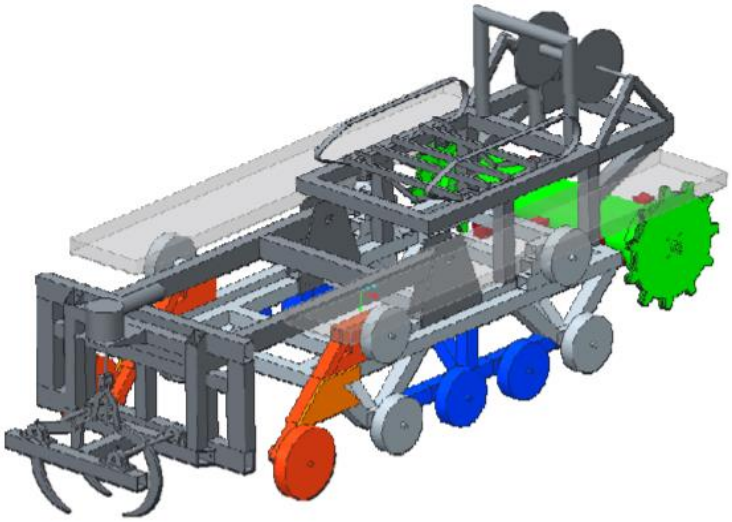

Figure 2.26: RG-iii remote operated crawler design

Illustrated in the above figure 2.26**,** is an engineering design of the RG-iii. The parts are divided into seven different categories, which include: the crawler frame and motor housing, the dynamic propulsion, tether management system (TMS), crawlers' buoyancy system, the dredging manipulator boom arm, and power distribution and ROV (tomcat).

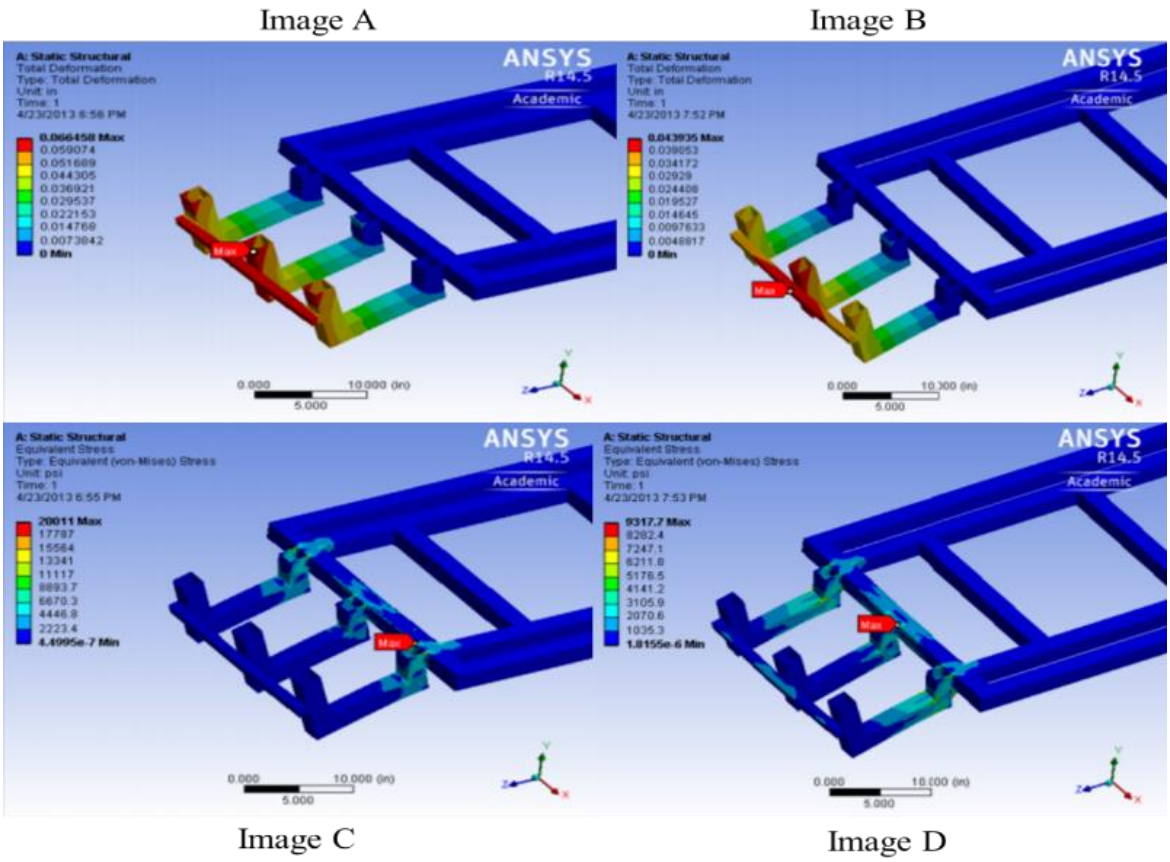

Figure 2.27: RG-iii FEA structural frame simulation using ANSYS (Wood et al., 2013)

This research further covers a CFD simulation using ANSYS, to analyze the RG-iii ocean vehicle under certain condition. Four different categories were analyzed, this includes figure 2.27'**s** image A, which is likely a deformation of the RG-iii original frame under certain conditions, and this matched known failure points on the vehicle. Furthermore, the max displacement value for the original design 0.066458-in (1.6880332-mm) was shown. Image B shows RG-iii deformation for the revised, the max stress according to this image B were easily indicated in certain areas were weld cracks of the frame with the design stress of 20011-psi (1407-kg/cm^2) were analyzed. Image C indicates the Von Mises stress for the original frame design under simulation, this analysis was still under certain minimum yield point but had the tendency of failures under consistent stress. The maximum stress was decreased to 9317.7-psi (655-kg/cm^2) after certain conditions. Image D indicated the points of failure and described what material is stronger and safer for the use of this design. This report concluded by stating the factors of safety of the RG-iii design, which was greater than 1. This confirmed that the frame is less likely to fail. But after due forces were added multiple times, failure such as cracks occurred in certain points.

Li et al., (2019) analyzed the mechanical structural design for underwater crawlers such as the Hybrid crawler-flyer underwater vehicle, (HUV). This paper categorized the design into five categories: the hydraulic piston, drive transmission system, drive motors, the waterproofed cabin and approach switch.

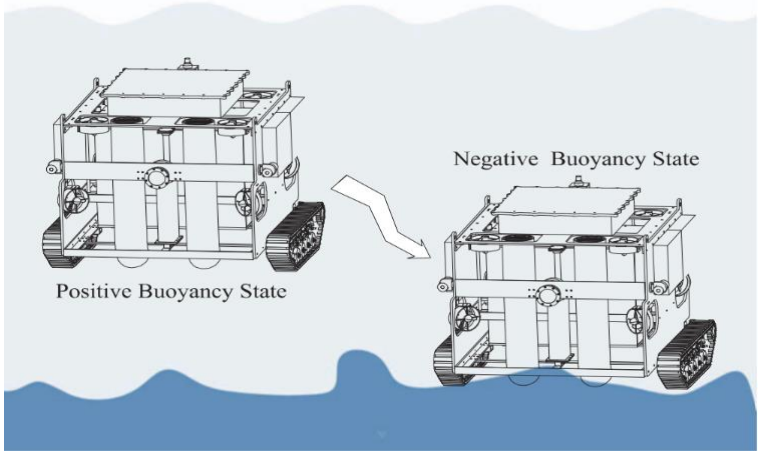

Figure 2.28: HUV design, positive and negative buoyancy state (Li et al., 2019)

The above figure 2.28 describes the HUV, and the mechanical structure. The sealed cabin of the crawler is categorized into five principal stages: HUV air enclosed cabin, water enclosed cabin, hydraulic cylinder end cover for water cabin, end cylinder head for air cover seal and the fixation plate. They analyzed the measurement of the O sealing ring and grooving of the cylinder flow. The piston had a working pressure within 0 MPa and 0.2 MPa and a sliding speed of 2mm/s. The transmission system comprised of one solid shaft and three hollow shafts. The system worked synchronously to generate linear movement of the piston. At the end of every second shaft drive system, a ball nut is attached with screw to determine some free point of motion. Drive motors were used as reducers, to generate strong output torque and the following formula was used to determine the minimum motor power:

$$P_0 = \frac{F_0 \cdot v_{r1}}{\eta_2} = 2076w$$----------equation (9)

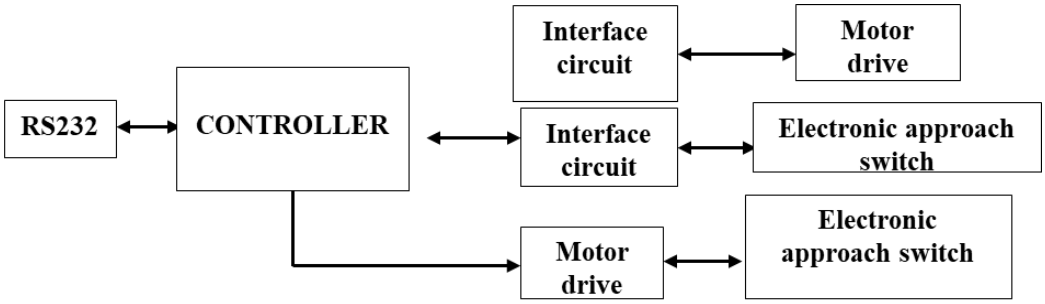

Figure 2.29: layout design for the electronic control system

Figure 2.29 was used to show the power and the output torque of the system. The piston moves to certain distance to stop the motor automatically. The system controller in figure 2.29 uses the enhanced 32-bit microcontroller STM32F103C8T6, and the 64KB flash operating system has the maximum frequency of 72MHz. It was further stated that the arm cortex-M3 core was designed with a high-performance microcontroller system for power conservation.

According to Wood et al., (2013) control systems and algorithm for unmanned ROVs, AUVs and UUVs make use of Proportional Integral Derivation (PID) and Fuzzy Logic Controllers (FLC). The paper discusses concepts in the field of ocean robot control systems. These controllers were used to compare control system designs for the existing development of unmanned ocean vehicles. (Wood et al., 2013) discussed about a new concept of complex control system for autonomous machines. This system combines different individual fuzzy controllers for their operation system. The combining of other complex controllers tends to give unpredicted problems that are difficult to approach. These kinds of operations are used to achieve consistent control of the operation. Joysticks are used in the control system for ocean robots such as AUVs, ROVs and UUVs. Operation control using this device introduce noise and reduces accuracy in controlling the robots. In other to develop better methods, two fuzzy were introduced and simulated, a decent result was used to determine if these complex methods are useful to solve control unit problems. Furthermore, there was a reduction in the control errors which was used to improve the complexity of the behavior of the control system. (Zhong et al., 2014) investigated on comparing Proportional-Integral-Derivative controller (PID) control systems and fuzzy logic control units for hydraulic flowing fluids. This system was carefully analyzed by using MATLAB and Simulink for up tanning the result. The results gotten from these simulations proved that fuzzy logic response faster and has small overshoot compared to the PID controller for hydraulic liquefied system. These autonomous controllers can be used for applications requiring robust performance that can't be achieved with simple functionality. This paper concluded by stating that the PID and PD are oscillatory in functionality which cause damage to the controlling units. Lee & Kim, (2014) analyzed the implementation of electronic control digital PID for the automation of speed control, for Direct Current (DC) motor systems using feedback systems. This research covers the

design of PID system controller. PID in this paper was used for feedback in a closed loop system to increase the accuracy and reduce the consistent effect of external disturbance and variation in a system. For an increase in the system performance ability, the total sum of three action term was performed which increased gain margin, stabilize unstable system and rapid control response by systematic proportional control. In the minimization of the system steady errors and derivation, an increase in the steady system was done and reduction in the overshoot circuit was improved for the behavioral control system during operational transients. (Suhas & Prof.S.S.Patil, 2014) stated that the development of very high-performance drive motors are useful for industries such as, offshore, automation, and mining. It was further stated that high performance drive motors have excellent dynamic speed command tracking system and fundamental load regulatory response. In addition to the authors finding, DC drive motors and servo motors have been finding useful application in today's technology, which includes defense, industries, robotics, and the ocean environment. These systems for DC application are simplified, easer for different application, reliable, and favorable. For practical research investigation, the author designed a control system for DC drive motors using fuzzy logic controller for their operation. The parameter for the fuzzy system controller was improved by MATLAB-GUI which was based on FLC and IFLC software algorithms. MATLAB-GUI was used for the reduction of the drive motor turning time and the controller in other software used less efforts for their operations. Three components were arranged systematically together for the structure FLC which can be called the Fuzzier, and they were used to measure the input of the fuzzy set. PID controller were used to compare IFLC for the improvement of the performance of the motor drive system in term of minimizing the overshoot settling time. Upalanchiwar & Sakhare, (2014) discussed the use of motion controllers in today's industries, and their mode of control for various application. DC motors are used for motion control systems. PID controllers with fuzzy technology were used to control DC motors. These methods were used for the control of complex systems and unclear models. It was stated that fuzzy PID controllers are one of the best methods used for controlling system because of their turning parameters for conventional PID related to the difficulty faced by these systems. According to the author, PID conventional system has poor robustness and are difficult in accomplishing their optimal condition under field operation. Fuzzy PID has provided excellent performance in effective control system, good dynamic response, and fuzzy control robustness. (Hanafi et al., 2013) analyzed a Quad-copter control system, operated through a GUI. Communication between the GUI and quadcopter was controlled wirelessly. This research approached a design for the GUI using Visual Basic (VB). In order to control the Quadcopter a simulation was rendered; fuzzy logic controllers were implemented to the design. The PID control system was designed and embedded in Arduino (UNO). PID was implemented for altitude motion control of the Quadcopter. For sustaining the quad-copter altitude using the input ultrasonic sensor, a PID was designed for that application. (Srinivas & Rao, 2012) stated that real control system exhibits a non-linear nature, conventional

controllers in some certain cases do not have the capacity to provide good and accurate results. This paper presented an efficient controller with three tanks level using a PID controller over fuzzy logic. This approach was used for the fuzzification and defuzzification process. A result was presented, FLC responded quicker and had the best centroid. Defuzzification method and triangular membership functions due the PID controller cannot give corrective actions and only initiate control action after error has been developed. On this PID controllers, concretive response with peak overshoot for the unit step input was observed. The FLC removed overshoot and the rise-time and settling time as well. Bhaskar & Sudheer, (2012) analysed the design and the development of a GUI using MATLAB, for the operation of DC motor speed control. The GUI was used for the turning direction of DC motors, control effectiveness and running control system. MATLAB-GUI software program made it user friendly to study the performance of various real time control system with less effort and energy consumption. (Sousa et al., 2012) discussed a concept of a lightweight ocean operator, the man-portable autonomous underwater vehicle (LAUV). The LAUV is lunched into the ocean depth of about 50 meters and can be recovered with less energy and operation. This ocean vehicle was built cost effectively for the use of oceanography, environmental and security surveys. The control system of this ocean robot was made possible by a Control Command Unit (CCU). The systematic operation of LAUV supports network of inter-operation of unmanned vehicles in the body of ocean water, for different operated vehicles. (Tehrani et al., 2010) discussed the operational design of the development, depth control and stability analysis of an underwater remotely operated vehicle (DENA ROV). This paper talks about the controller design which was used to reduce overshoot limitation in the system. Overshoot systems were used for unsafe environment detection, such as if the ROV is piloted in a dangerous location a sent back signal system picks up. A PID was designed to overcome the problems of pickup system. The controller for the DENA ROV was designed to have five electronic boards which include the power controller, controller arm sensor, and tow thruster proportional control board. On the board, a joystick was used for the pilot control. Commands are collected by the joysticks which are translated into a separate coded instructions by a tethered cable RS232. The board consist of two AVR Atmega16 microcontrollers which were used for the Main Micro and the Equipment Micro. Corinna Kanzog, (2015) defined a concept for electric subsea crawlers as a remotely controlled vehicle that is used for exploration and recovery in deep sea. It is designed to sink to the bottom of a body of water such as in deep-sea exploration (mining), where it moves about using traction against the bottom of the seabed with wheels or tracks. It is usually tethered to a surface ship by cables providing power, control, video, and lifting capabilities, which enable its operating function. This paper further discussed collaboration of ocean robots in operations such as situational awareness, probe extraction. Probe handling in situ analysis were performed after the design of the manipulators. This robot was designed for complex functions such as moon rover, for the International Space Station (ISS). Electronic ocean crawlers were first introduced in

the year 1950. (Chutia et al., 2017) discussed the history of underwater electrical propelled crawler, which was launched in the early 19s and was proposed by the Royal Navy of Great Britain. It was aimed at the recovery of torpedoes and removal of underwater sea mines, in the 1960. A cable remotely controlled underwater vehicle was lunched for the aim of rescue and recovery operation. The growth of offshore industry in 1980 to 1990 for military operations was very noticeable, however it later shifted to the oil and gas industries. probably interactive, (2019) described a concept as shown in figure 2.30 below. The figure shows a vacuum cleaner, which is used to illustrate the fundamental dredging unit of an electrical seabed crawler.

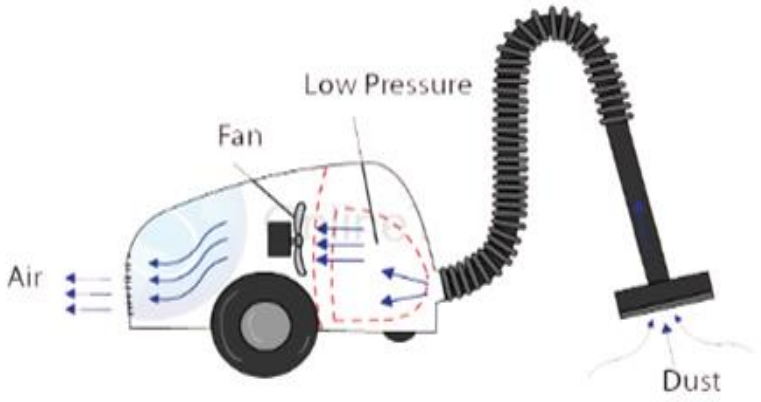

Figure 2.30: illustrates a Vacuum with direction of air flow (probably interactive, 2019)

The Bernoulli's principle, states that as the speed of air increases, the pressure decreases. Air will always flow from higher pressure area to a low-pressure area, to try balance out the pressure. The vacuum pulls air in, and the air sucks up dust as a negative pressure. Bernoulli's formula is expressed as shown below:

$$P_1 + {}^1\!/_2\, pv_1^2 Pgh_1 = P_2 + {}^1\!/_2\, pv_2^2 + Pgh_2. \text{ ----------equation (10)}$$

Lumen physics, (2021) analysed the simplified form of the Bernoulli's equation, that was summarized in the following memorable world equation:

static pressure + dynamic pressure = total pressure points in a steadily flowing fluid. --------equation (11)

This is regardless of the fluid speed at that point which has its own unique pressure p and dynamic pressure q. The rotation of the fan in powered by a 220 V electric motor, which causes a clockwise rotation and enables the fan to suck in air. Anything caught in is pushed out into a bag or a canister, to create the negative pressure. The same principle can be applied to the electrical seabed crawler. This autonomous crawler is built in with a dredging pump called the centrifugal pump or positive displacement pump. This pump is connected to a powered electric motor which helps to drive the impeller in the casing. The

centrifugal pump has two openings: the product inlet and product outlet. Flexible hoses/pipe depending on the product type are connected to the outlet of the centrifugal pump which helps in systematic passage of the product to the ship.

Due to the condition of the sea floor, Automotive Sea Vehicles (ASV) use the track wheels' system which are mainly designed for low seep movement but are power efficient in any condition of seafloor or land operation. The track system of the robot for the use of traveling can be used in rocky seabed or soft soil depending on the geologist mapping on mineral location. Electrical motor control valve and controller flow meter is used accordingly. The track system is best used when it comes to seabed automation systems due to its advantage in maneuverability. This has sufficient weight to stabilize traction between the sea and the crawler tracking system. In the propulsion system, the continuous track systematically runs on a fixed band of treads or track plates driven by two or more bearing wheels. These track wheels have large surface area around the track's distribution. Rubber tracks are better than steel ones on an equivalent vehicle, because they enable continuous tracked vehicles to traverse soft ground with less likelihood of becoming stuck due to sinking seabed. Vehicles tracks generally enable more balancing when motion is taking place, moving from one point to another, not considering the heavy dredging machines that are built on it. The dredging crawler, which is a remotely operated crawler, uses several types of electrical equipment such as sensors tracks, metal detectors, crawler chain, crawler belts, electrical cylinder, electrical camera, very high-frequency lighting, centrifugal pump, joystick and return switches. These systems assist in efficient automation and extraction under the seabed. Ocean tracking robots drive system can be mathematically modelled using tracking vehicle dynamics and its differential movements. According to Daanen, (2017), who analysed the development of a model that describes the interaction between a track drive system and the seabed soil. Based on the model an analytical tool was used to qualify and quantify the impact of some aerometer's sensors. The Vehicles were driven by a track drive and referred to as tracked vehicles or tracked equipment. Forward thrust was generated by the electrical motors which produced rotational motion. In theory, two different types of track drives were identified: flexible and rigid track belts. Flexible tracks contain rubber belts and certain types of steel linked tracks. The rigid track belts were governed by steel linked tracks. The operational behaviour of both were reported to be different. The main criteria to identify a track belt type, is the ratio between road wheel spacing and track link length. The analysis of both track types was described in reference to the rigid track belts. Track driven vehicles can be assembled with or without a suspension. If a suspension is applied, it could be one suspension for the entire track frame or a separate suspension for each road wheel. The presence of a suspension has an impact on the interaction between the track and the soil, which depend on a significant number of parameters.

Figure 2.31: fundamental parts of a robotic track drive system (Daanen, 2017)

As shown in figure 2.31, the presence of a suspension has an impact on the interaction between the track and seabed floor, this paper was used to describe the extent of interactions which depend on the significant number of parameters components for our tank tread drive system of the electric powered subsea robotic crawler. The track frame is made out of aluminum. The following components such as tank tread chain link, Tank tread idler wheels, Tank tread sprockets 11mm bronze bushing, motor hub, DC gear motor, and motor mount are assembled to make up the driving base. The undercarriage frame provides the track drive with structural support, furthermore most of the other components are mounted on the frame. The track tank tread chain link differs from each unit, but it consists of a chain with pads mounted on it. These pads can be made of steel or heavy-duty plastics. If grousers are applied, they are mounted on the pads of the track chain. This system maintains sufficient pre-tension in the track. The idler is a big roller, via a cylinder connected to the frame. The desired pre-tension can be set by operating the cylinder. The function of the track and carrier rollers are to support the track over the horizontal lengths between the sprocket and idler. It was stated that track drive contains more track rollers then carriers. The track rollers are used to secure contact area between track and the seabed. Ciszewski et al., (2014) analysed the structural design of an in-pipe mobile inspection robot. It utilized two tracks for its movement. The subsea configuration ensures stability and manoeuvrability. This robot was designed to operate with a flexible drive positioning system. The paper further stated that robot track drives were designed to operate in circular and rectangle pipes. A prototype was designed, and the dynamics was illustrated under certain conditions. The tracks were tested in the laboratory and a FEA simulation was conducted. This paper described the working configurations for this robot kinematics and dynamic model formulated and verified experimentally. Mooney & Johnson, (2014) studied the method used in solving the efficiency of loop closure in harsh environments that utilize RFID technology for slippage-sensitivities in odometry 2D pose dynamic drive tracking. He presented an approach that enables the robot to continuously execute its climbing elevation in rough weather. The angle of elevation had been evaluated on ground driving motor such as Lurker robot. This robotic platform is capable of overcoming autonomous rough terrain containing ramps and rolls. In areas where robotic crawler

machines are used for ocean exploration, the evaluated elevation for their driving unit are coded to its highest estimate. In unpredictable environments, these methods cause less efficient torque for climbing an open ramp elevation.

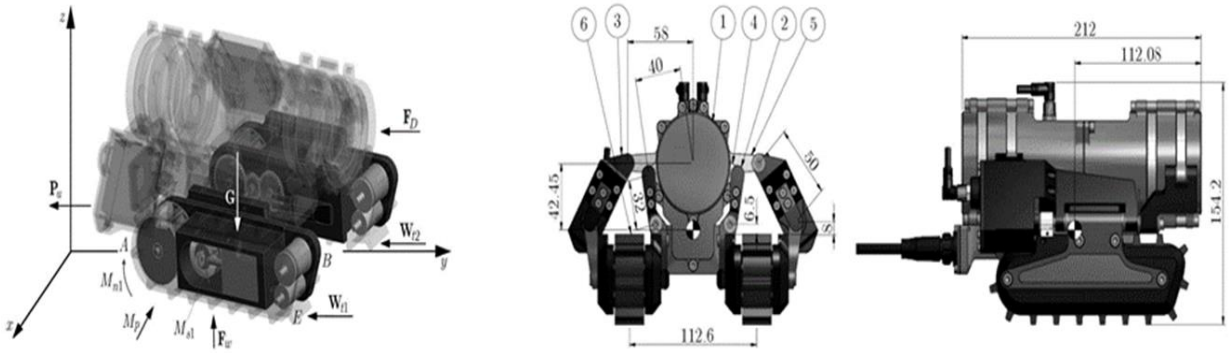

Figure 2.32: force acting on the dynamic robot as simulated (Ciszewski et al., 2014)

Figure 2.32 shows the robot track positioning system. This consists of two independently rotating rings with the centre of rotation at a fixed axis. The dynamic modelling of a dredging crawler is described in the following research (Burdzinski 1972; Chodkowski, 1982, 1990; Danjniak, 1985; Trojnacki, 2011; Zylski 1996). The equations were modelled using a method based on Lagrange multipliers. Maggi's equations were also simplified and used for this operation (Giergiel and Żylski,2005). In the dynamic model of the robot, the same characteristic point on the structure is considered as in the kinematic description.

The kinetic energy of the robot E is the total number of energies in a particular component $E = E_R + E_m, + E_{m_2}$

Where; E_R is the kinetic energy of the frame.

E_{m_1} is the kinetic energy of the left track drive module.

Em_2 is the kinetic energy of the right-side track module

The kinetic energy of the robot frame is the sum of energies E_R and E_{R_2}, resultant from translational and rotational motion with respect to the instantaneous centre of rotation 0.

$$E_R = E_{R_1} + E_{R_2} = \frac{I}{2} M_R V_c^2 + \frac{1}{2} I_R B^2$$ ---------- equation (12)

Where m_R is the robot frame I_R- moment of the inertia of the robot frame, β- angular velocity of the robot frame with respect to the instantaneous centre of rotation. By introducing

$v_c = \sqrt{x_c^2 + y_c^2 + z^2 c}$ and $E = E_R + E_m, + E_{m_2}$ ---------- equation (13)

the kinetic energy of the robot frame will be obtained as

$$E_R = \frac{1}{2} m_R (x_c^2 + y_c^2 + z_c^2) + \frac{1}{2} I_R B^2 \text{---------- equation (14)}$$

Track drive was determined by using this formula:

$$E_m = k_1 + E_k 2 + E_{k_3} + E_0 \text{ ---------- equation (15)}$$

Djordje Vukcevic et al., (2018) demonstrated a test setup to show the feasibility of proposed and derived approaches for including static friction joint forces, in computations of motion for a one degree of freedom inverse kinematics. The experimental setup involved scenarios, i.e., modeling of a robot environment in which gravity effects do not exist. Additionally, artificial static friction joint torques, and artificial external Cartesian forces were generated. Furthermore, in both parts of the experiment, the motion of the robot is not constrained. In this paper, the crawler's model was designed using a 3 DOF joint arm. Multiple control system were represented as a kinetic chain of rigid bodies connected by a prismatic joint. One of the connected chains was fixed permanently to the base, while an end effector was mounted to the other end of the chain. Manager & Ç Yavuz, (2009), discussed and analyzed a robotic arm, as well as the relationship between the positions, velocities, and accelerations of different links for the manipulators based on its manufactured application. (mathworks, 2021) described kinematics as a science of motion. In a three-joint robotic arm, given the angles of the joints, the kinematics equations can give the location of the tip of the arm. Inverse kinematics were described for the reverse process. Urrea & Saa, (2020) analysed the desired location for the tip of the robotic arm. A systematic graphic simulation was performed to determine the kinematics and dynamics behavior for the redundant planar manipulator for the robot. To analyze the graphical simulator, solidworks, SIMMECHANICS tools and MATLAB/Simulink were used to mathematically obtain results. This paper further reported the results obtained from control of the inverse kinematics using algorithm based on probabilistic methods. In controlling the joint trajectory, interpolation third order polynomial were used. Daanen, (2017) developed a model that describes the interaction between a track drive system and the seabed soil. Based on the model an analytical tool was used to qualify and quantify the impact of aerometer sensors. The Vehicles were driven by a track drive and referred to as tracked vehicles or tracked equipment. He further stated that forward thrust was generated through rotational motion caused by the electrical motor, which resulted in translating motion. In theory, two different types of track drives were identified: flexible and rigid track belts. The group considered as flexible tracks contain rubber belts and certain types of steel linked tracks. The rigid track belts were governed by steel linked tracks. The operational behaviour of both were reported to be different. The main criteria to identify a track belt type, is the ratio between road wheel spacing and track link length. The analysis of both track types was described in dedication to the rigid track belts. Track driven vehicles can be equipped with

or without a suspension. If a suspension is applied, it could be one suspension for the entire track frame or a separate suspension for each road wheel. The presence of a suspension has an impact on the interaction between the track and the soil, to what extend depends on a significant number of parameters.

Yang et al., (2012) discussed about hydraulic excavator design and their wide range of usage such as mining, construction, and forestry application. The paper further stated that the structural design for excavator undercarriage depends on the performance of the backhoe front attachment. The author research focused on excavator attachment which includes structural kinematics analysis, dynamic analysis, trajectory planning and control, fatigue life analysis and structural optimization design.

This paper concluded with some fundamental improvement such as reliability and efficiency which reduce excavator production cost. The increase in using the approach of virtual prototyping has led to more cost effectiveness, less wastage, improved efficiency, and time conservation.

CHAPTER THREE: METHODOLOGY

This chapter started by presenting the undercarriage system of the EPRSDC. After which the electronic components were discussed with respect to their specifications and functions. The next section covers the design and manufacturing of the venturi dredging nozzle. Following that, the software used was mentioned. In the subsequent sections the test environment, final design, waterproofing concepts for future design and the test ramp were presented respectively.

The model was designed using parts from PITSCO TETRIX MAX robotic kits. The electric powered robotic subsea dredging crawler design is subdivided into four main parts.

1. designing and assembly of the undercarriage drive system,
2. the 2DOF boom arm
3. the tank chain drive system, and
4. the electronic system, which is controlled using a custom User Interface

All design and simulation were done using solidworks 2020 student version.

3.1 Hardware for the EPRSDC with an using PITSCO TETRIX MAX robotic kits

3.1.1 Crawler Frame

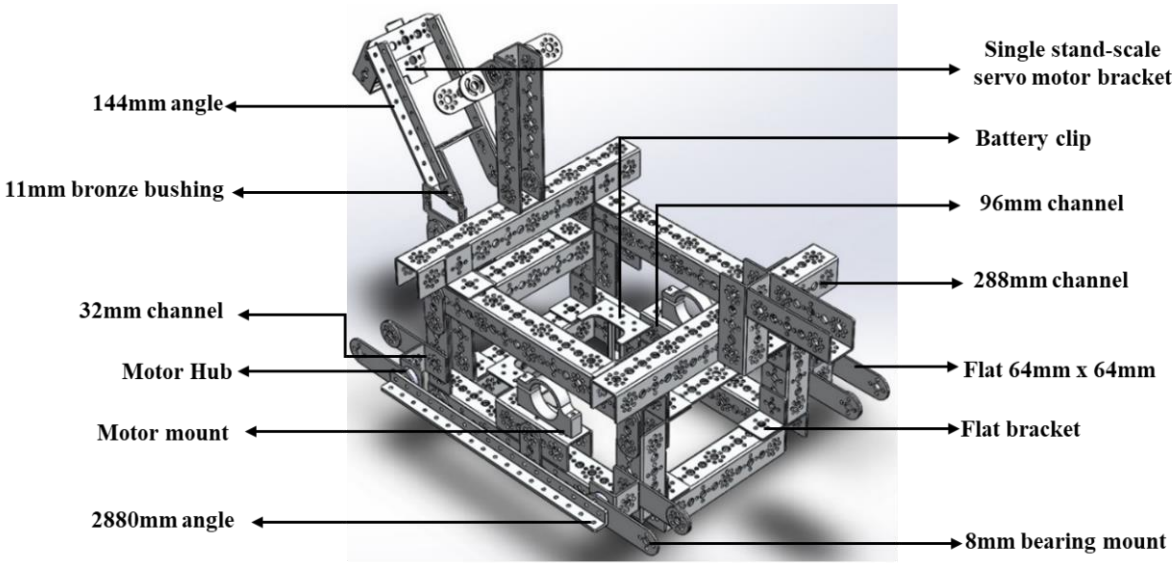

Figure 3.1: structural frame of the EPRSDC

Figure 3.1 above shows the main structural design. The frame was designed and assembled using channels, bars, angles, plates and brackets, flats, axles, hubs, spacers, posts, stands-offs, nuts, screws, and fasteners. The material used in fabricating these above-mentioned parts is the 1050 series Aircraft grade aluminum.

3.1.2 2DOF for the boom arm with a venturi dredging nozzle

Some ocean dredging crawlers utilize a boom arm with various degrees of freedom to position the suction pump. Our arm allows for mounting of dredging and pressure pump nozzles at the end effector to carry out underwater dredging operations.

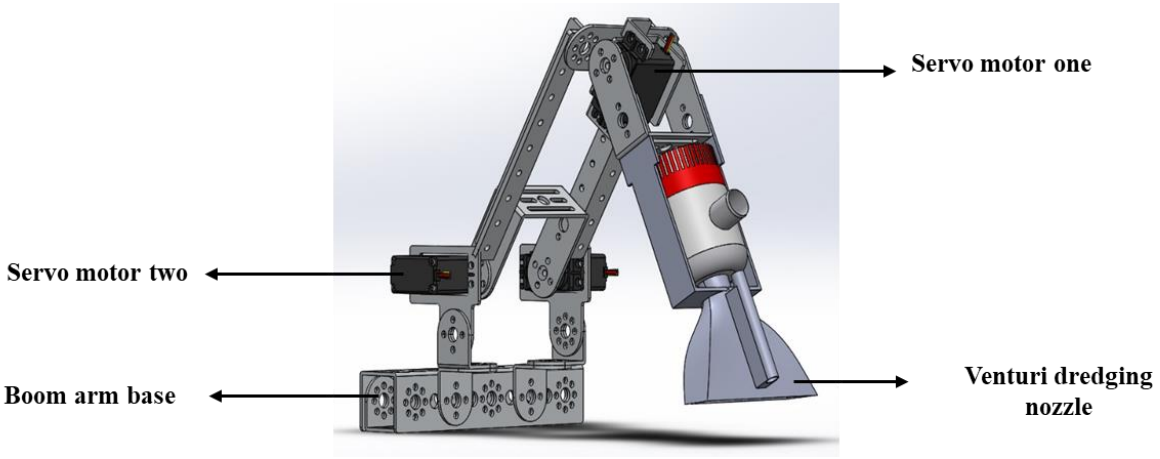

Figure 3.2: 2DOF boom arm with a venturi dredging nozzle

Figure 3.2 shows our 2-DOF concept for the boom arm with a venturi dredging nozzle. The arm is controlled using three 6.7V servo motors, which get control signals from the NI myRIO and the servo motor controllers. The purpose of this arm is to access extractable materials. The arm was made from 1050 aircraft grade aluminum, whereas the venturi dredging nozzle was made of 3-D printed plastic. The servo motors were mounted with a servo motor single standard-scale bracket and standard-scale pivot arm with bearings. The servo motors used to control the movements of the arm are the 180° DSSERVO DS3225 25KG Metal Gear High Torque Waterproof Digital Servo motors. The venturi dredging nozzle was manufactured using Aluminum. In this research, a prototype with a robotic arm having 2DOF was implemented. UI was also developed for sending commands, to control the operation of the system. A program was developed using LABVIEW to connect with an NI myRIO in order to control the arm's movement and positions.

3.1.3 EPRSDC undercarriage structural base

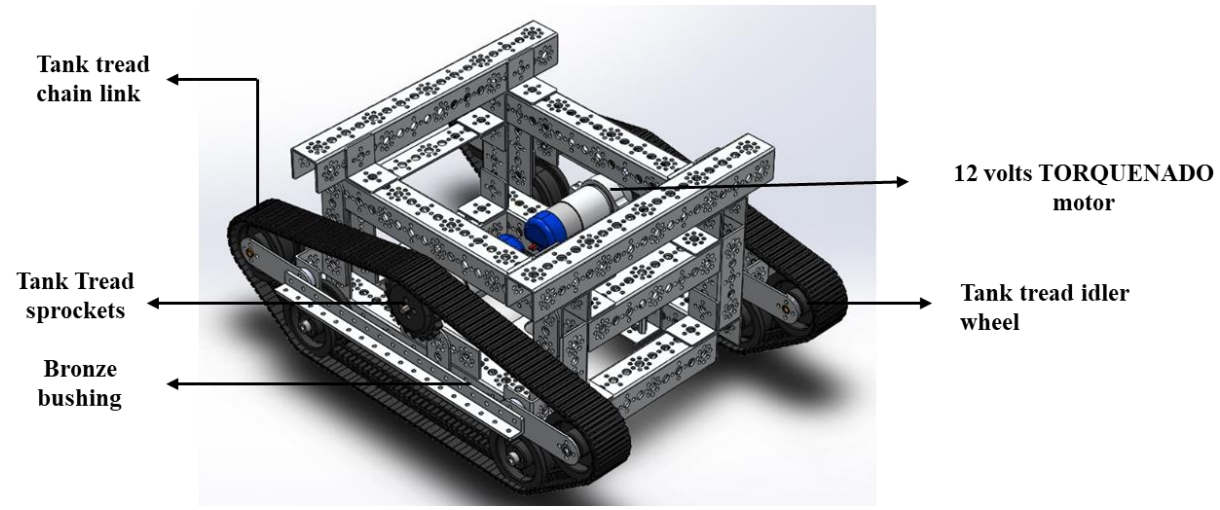

Figure 3.3: undercarriage tank tread idler drive system for EPRSDC

Figure 3.3 shows the structural design for the electric powered robotic subsea dredging crawler's undercarriage drive system. A 288mm x 160mm x 96mm stand up plate boxed frame was designed with the total tank tread chain link of 406mm length. The tank tread sprocket was attached with a motor hub, which was connected to a 12-volt torquenado motor shaft to rotate the track clockwise and counterclockwise. The tank tread idle wheels were used to implement a parallel drive for the chain link and also give shape to the structure. The electronic motor controller was used to drive the 12-volt torquenado.

3.2 Communication system for the EPRSDC

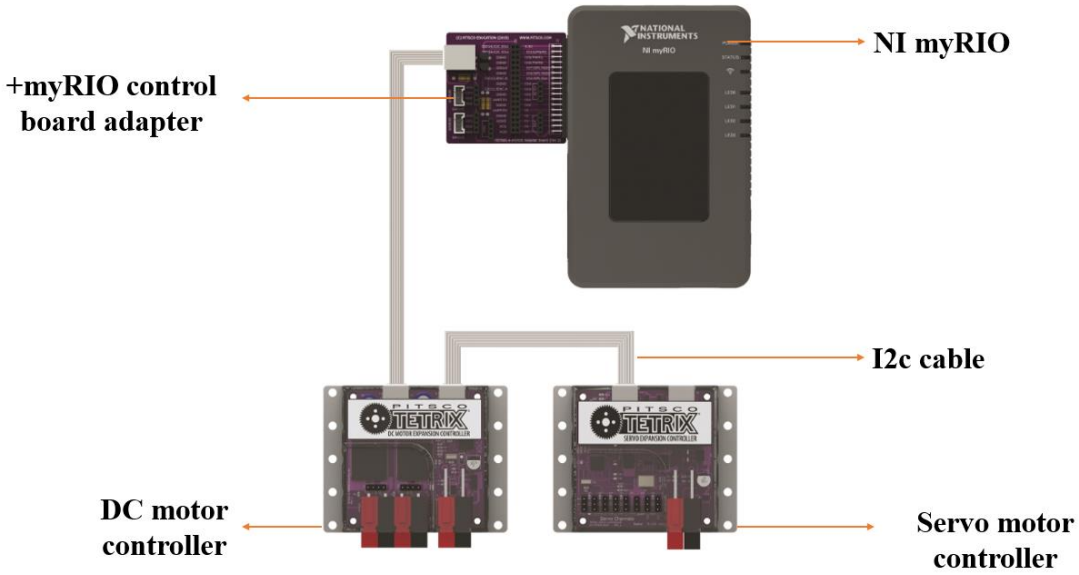

Figure 3.4: electronic communication system for the EPRSDC

The communication system of the electric powered robotic subsea dredging crawler is seen in Figure 3.4 above. The crawler is operated using LabVIEW for its programming algorithm. The National Instruments (NI myRIO) is responsible for processing both basic and complex instructions through programs. This electronic machine is considered the “brain box” of the EPRSDC. It is show in figure 3.5. The electronic model also includes Wi-Fi support, which was used to operate the crawler over a long distance instead of tethering. The NI myRIO is connected to the + myRIO Control Board Adapter. This electronic device is designed to easily connect TETRIX Motor Controllers to the NI myRIO using the I2C cables. The motor controllers were used to operate two DC 12-volt torquenado motor. A I2C cable was used to output communication for the motor controller to the servo motors. The servo motors were used to control the 2DOF boom arm for the venturi dredging nozzle.

3.3 Electronic components and specifications for the EPRSDC Prototype

3.3.1 NI myRIO

Figure 3.5: NI myRIO used for the control system of the EPRSDC

As shown in figure 3.5, the NI myRIO is considered the brain of the EPRSDC. The myRIO is an Embedded Device featured with an I/O on both sides of the device in the form of MXP and MSP connectors. It includes analog inputs, analog outputs, digital I/O lines, LEDs, a push button, an onboard accelerometer, a Xilinx FPGA, and a dual-core ARM Cortex-A9 processor. This model also includes Wi-Fi support. You can program the myRIO Device with LabVIEW or C. The NI myRIO has sufficient functionality to operate the subsea robotic crawler. Its specification is shown below.

Table 3.1: The NI myRIO-1900 Hardware specification

provides analog input (AI)
analog output (AO)
digital input and output (DIO)
power output in a compact embedded device
audio
It connects to a host computer over USB and wireless 802.11b, g, n.

3.3.2 12-volt DC Tetrix Max Torquenado motor

We used two 12-volt DC Tetrix Max torquenado motors to drive the tank track system, tank tread idler wheels, the tank tread chain links and tank tread sprockets of the EPRSDC. Note that all the above-mentioned components make up the EPRSDC driving unit when combined.

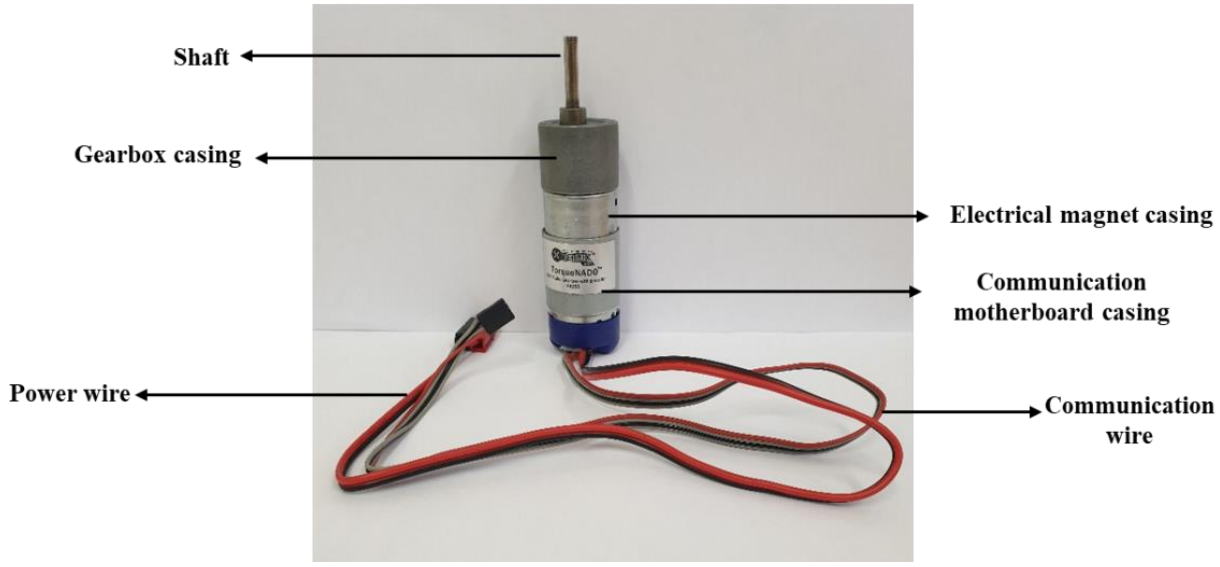

Figure 3.6: 12-volt DC Tetrix Max torquenado motor

Table 3.2: DC gear motor specification as used for EPRSDC model

Overall Length	134.1 mm (5.28 in.)
Maximum Diameter	37 mm
Body Material	Steel with plastic encoder housing
Lubrication Included	inside Gear box
Shaft Hardness	45-50 Rockwell C
Motor Weight	324 g
Output Shaft Diameter	6 mm with 0.5 mm deep flat
Output Shaft Length	26 mm
Gear Ratio	60:1
No-Load Speed	100 rpm
Voltage (nominal)	12 volts DC
Stall Current	8.7
Stall Torque	4.9Nm (700 oz-in)
Cycles per Revolution (motor shaft)	6
Cycles per Revolution (output shaft)	360
Countable Events per Revolution (motor shaft)	24
Countable Events per Revolution (output shaft)	1440

3.3.3 Tetrix Max DC motor expansion controller

Figure 3.7: Tetrix Max R/C motor controller

Illustrated in figure 3.7 is the motor controller, which is a DC motor expansion peripheral designed to allow the addition of multiple DC motors connection, additional two DC motor output channels and two quadrature encoder inputs for easy motor control. The motor controller is responsible for controlling the speed and torque of the electric drive system for the crawler.

Table 3.3: Motor controller specification

Memory	32 KB flash programmable memory (ATmega328P).
Power	9-18 volts DC.
Recommended motor	TETRIX 12-volt DC Motor (39530).
Battery voltage monitoring	0-18 volts range.

3.3.4 Tetrix Max servo motor expansion controller

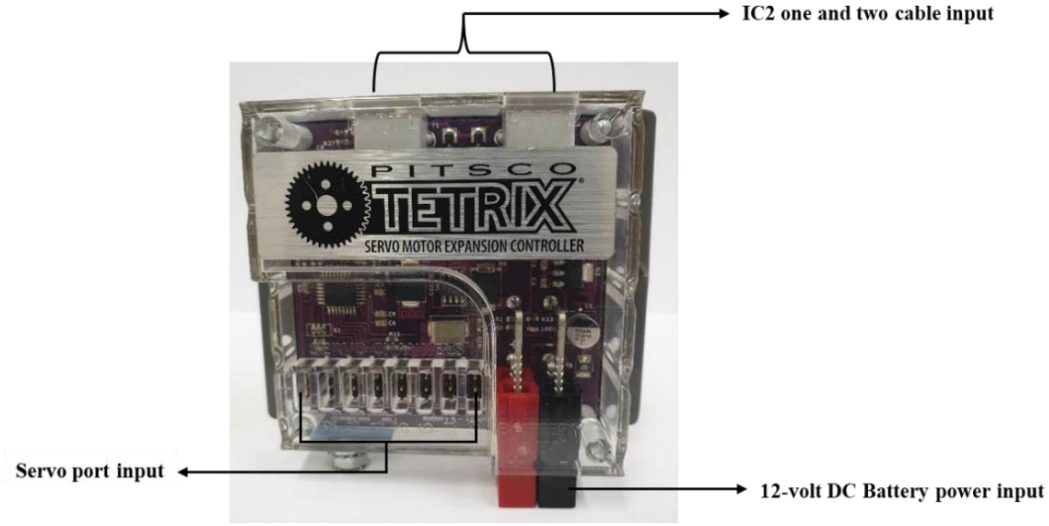

Figure 3.8: Tetrix Max servo motor expansion controller

As shown in figure 3.8 the Tetrix Max servo motor expansion controller enables the boom arm of the EPRSDC to utilizes its 2-DOF. The arm uses a 180° DSSERVO DS3225 25KG Metal Gear High Torque Waterproof Digital Servo to control its movements. The TETRIX MAX Servo Motor Expansion Controllers are servo motor expansion peripheral that are designed to allow addition and operation of multiple servo motors at the same time. The device provides us with an additional six servo motor output channels and two continuous rotation (CR) servo motor output channels for increased motor control capacity.

Table 3.4: Servo motor controller specification

Power	12 volts DC using TETRIX MAX NiMH fuse protected battery pack; blue LED power indicator
Standard servo ports	6 total; servo channels 1-6
Continuous rotation (CR) servo ports:	2 total; CR1 and CR2 channels
Total servo power limit:	6 volts DC; 6 A max
Servo motor control modes	Set servo speed (0-100%) Set servo position (0-180 degrees) Set CR servo state (Spin CW/CCW) Read servo position
Battery voltage monitoring	Battery voltage monitoring: 0–18-volt range
Battery connection port	Power pole type; additional port for daisy-chaining battery power to additional motor controllers
I2C data port	2 ports total sharing the same bus; one port used for input, the second for output to additional daisy-chained motor controllers

3.3.5 +myRIO control board adapter

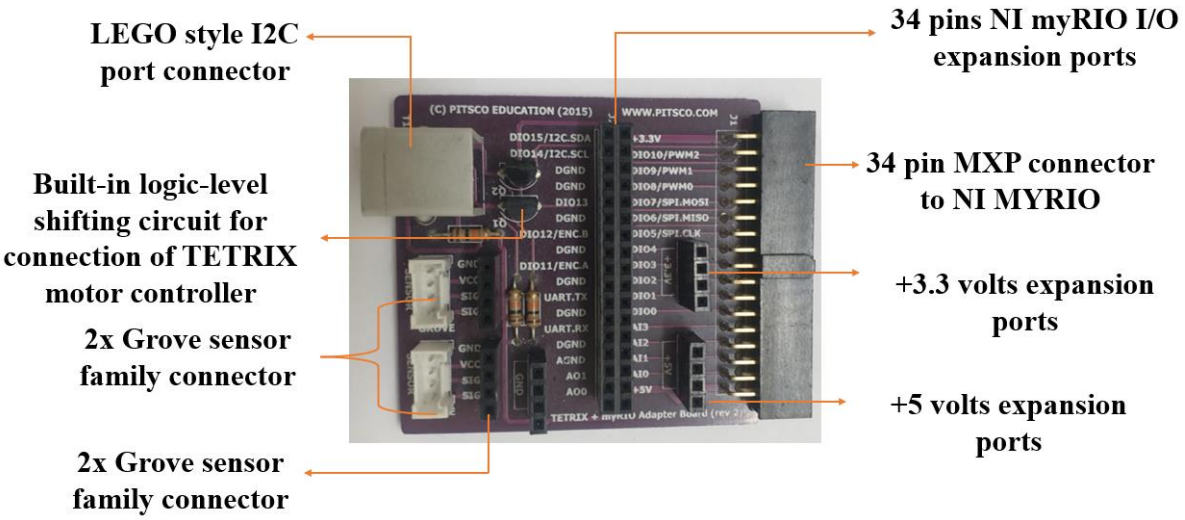

Figure 3.9: +myRIO control board adapter

The + myRIO Control Board Adapter shown in figure 3.9, is designed to easily connect TETRIX Motor Controllers to the NI myRIO. On our NI myRIO, the 34-pin MXP connector was used to link communication to the NI myRIO. The LEGO style I^2C port connector for the TETRIX motor controllers were used to link control communication from the first port of the motor expansion controllers.

Table 3.5: +My RIO control board adapter specifications

logic-level shifting circuit
GND expansion port
34-pin my RIO I/O expansion port
+3.3 V expansion port
+5 V expansion port
12v battery

3.3.6 BETU 2pack 25kg High Torque RC servo, Waterproof servo motor

Figure 3.10: BETU 2pack 25kg High Torque RC servo, Waterproof servo motor

As shown in figure 3.10 above, the servo motors control the boom arm of the EPRSDC. The robotic crawler boom arm was controlled using two servo motors which also enable the lifting motion of the venturi dredging nozzle for obstacle avoidance and dredging in narrow spaces. These servo motors can operate under high temperatures ranging from $30^0\text{C} - 80^0\text{C}$ with an operating temperature ranging from$15^0\text{C} - 70^0\text{C}$. These servo motors get their communication signals from the servo motor controllers with a power input of 4.8-6.8 volts. The dimensions of the servo motor assembly with the single standard-scale servo motor bracket, were measured as 40mm x 20mm x 40.5 mm with the total weight of 60kg. The servo motor gear ratio is 275 with a double bearing system. The connector wire is 300mm long and the device has a working frequency within 50-333Hz. It has a waterproofing IP rating of IP66.

Table 3.6: Servo motors electrical and Control Specifications

Operating voltage	5v/6.8v	Control system	PWM (plus width modification)
Idle current (at stopped)	4mA-5/5mA-6.8v	Pulse width range	500-2500µsec
Operation speed (at no load)	0.15 sec/60^0-5v; 0.13sec/60^0-6.8v	Neutral position	1500 µsec
Stall torque (at locked)	21kg-cm-5v; 24kg-cm-6.8v	Running dredging	270^0 (when 500-2500 µsec)
Stall current (at locked)	1.9A@5v; 2.3A-6.8v	Dead band width	3 µsec
Connector wire	300 ± 5mm	Operating frequency	50-330HZ
		Rotation direction	Counter-clockwise (when 500-2500 µsec)

3.3.7 Logitech brio 4k ultra-HD webcam stream edition pro

Figure 3.11: Logitech brio 4k ultra-HD webcam stream edition pro

Seen in figure 3.12, is a Logitech brio 4k ultra-HD webcam stream edition pro webcam camera. This device was used to capture images and videos in order to send back visual signals to the crawler operator. It can be modified to be used in viewing mapped points for the subsea dredging operation in the mining industry. The ocean crawler's maximum zoom video feature resolution is 4096 x 21060 pixels. The maximum frame rate is 60 fps with a supported video mode of 1080p. A 3.5m tethered wire interface was connected from the crawler to the control system via a 3.2 USB cable. The ULTRA HD 4K system captures the smallest details of the pool floor and maintains full HD quality even as you zoom in. HDR vividly shows you accurate colors, even in dim lighting. It provides 4 times the resolution of a full HD video and adjusts to changes in brightness.

3.3.8 Tetrix Max 12-volt 3000 mAh battery

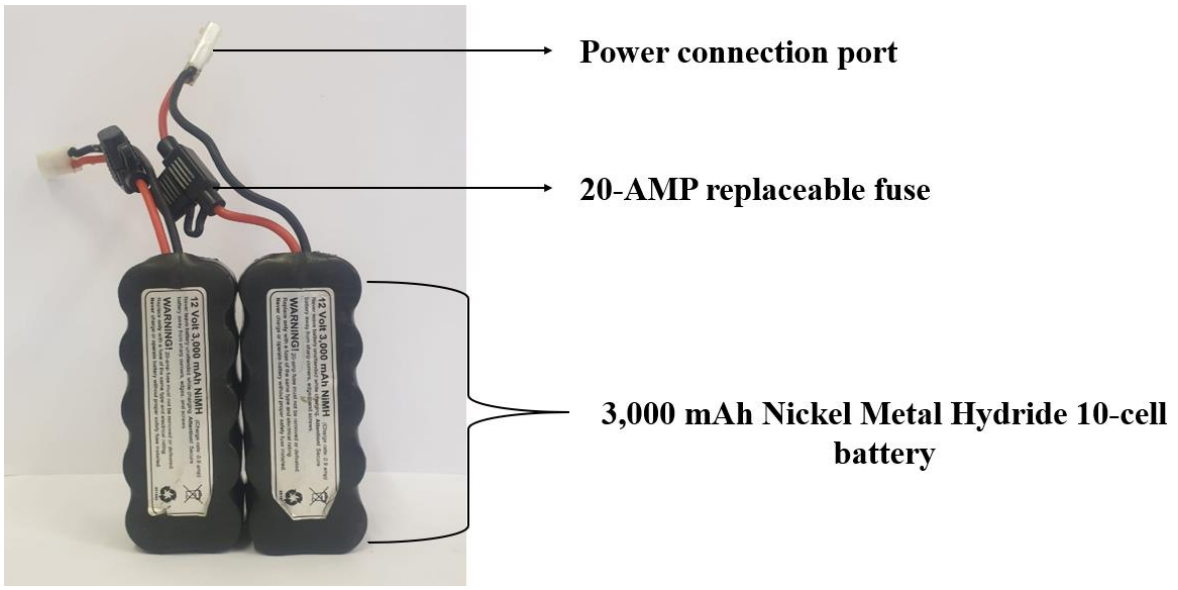

Figure 3.12: crawlers 10-cell power pack battery

We powered the electric robotic subsea dredging crawler with a 12V Nickel Metal Hydride (NiMH) 3000mAh capacity 10-cell battery, seen in figure 3.12. This rechargeable pack can power the EPRSDC for about 2-3 hours. The 3,000mAh NiMH pack features a built-in, 20-amp replaceable fuse for safety. The 2-relay module used 30A high/low level trigger was powered directly from the nickel metal battery to control the two bilge SEAFLO pumps.

Table 3.7: Battery Specifications

Weight: 579.6 g per battery
Size: 115 mm x 45 mm x 50 mm
Other Products Required: Battery charger, sold separately

3.3.9 Subsea lighting led Nova sub 6000 Lumen LED light

Figure 3.13: Subsea lighting led Nova sub 6000 Lumen LED light

Figure 3.13 shows a subsea (LED) with a dive light, and a light source carried by the EPRSDC to illuminate the underwater environment. Usually, underwater vehicles carry self-contained lights. In some cases, surface-supplied divers may carry lights powered by a cable supply.

Table 3.8: Subsea lighting led Nova sub 6000 Lumen LED light specifications

Brightness	6000 lumens
Beam angle	130 floods
Size	54mm diameter
Material	Plastic
Weight	470g (on land), 250g (underwater)
Voltage	7 volt each

3.3.10 12-volt SEAFLO 01 series 1 100GPH SEAFLO BILGE pump

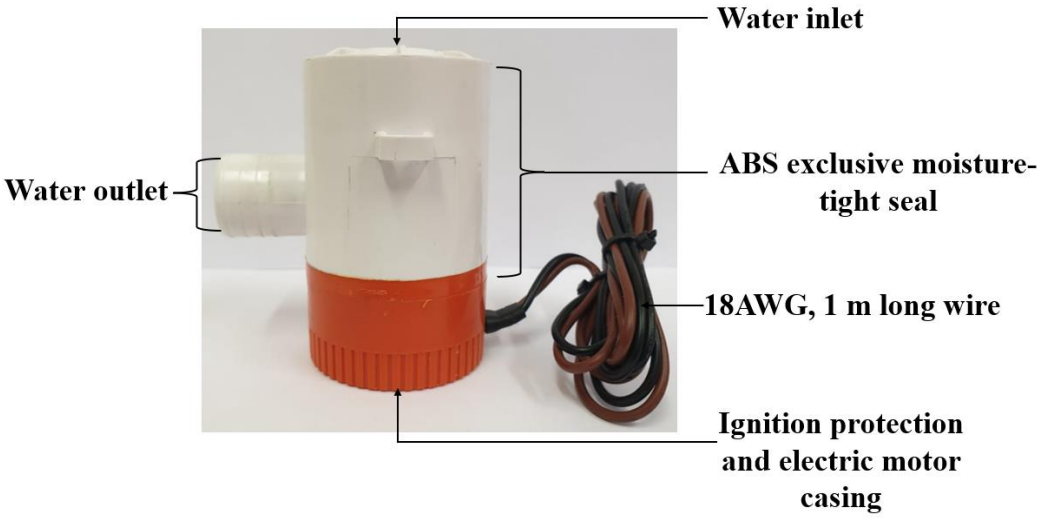

Figure 3.14: EPRSDC seaflo bilge pump

Figure 3.14 is the 12-volt SAILO PUMP used for the dredging of materials from the CPUT swimming pool floor of about 1.8m deep, to the collector and also for pressure breaking of the sea floor. The pump was mounted to the venturi dredging nozzle and also at the back of the crawler as shown in our results and discussion (chapter 4). To select an appropriate pump for this design we considered parameters such as: weight of the pump, low power consumption, low maintenance cost and high flow rate. Our selected pump weighed 0.3306 kilograms, with a length of 180mm and a breadth of 100.7mm. The pump's outlet was connected to a 16mm-diameter venturi dredging nozzle, which allowed easy flow of sediments to the impeller and through the pipe (riser). Furthermore, this pump was controlled by the NI myRIO incorporated with a relay. The relay was powered with a 12-volt 3000mAh 10 cells battery, which was connected with a 5-volt digital communication in-link from the NI myRIO to the relay output. This enabled us to control the pump directly from the program to switch it off and on.

Table 3.9: EPRSDC 12-volt 100GPH SEAFLO Bilge dredging pump specifications

Pump model	Pumps flow rate	Voltage capacity	Max draw	Fuse Amps	Pumping head	Wire leads	Pump outlet Diameter
SFBP1-G1100-01	1130GPH	12VOLT	6.0A	5.0A	4.5m	3' (1 m)	1-1/8

3.3.11 2-way relay, module 30A high/low trigger

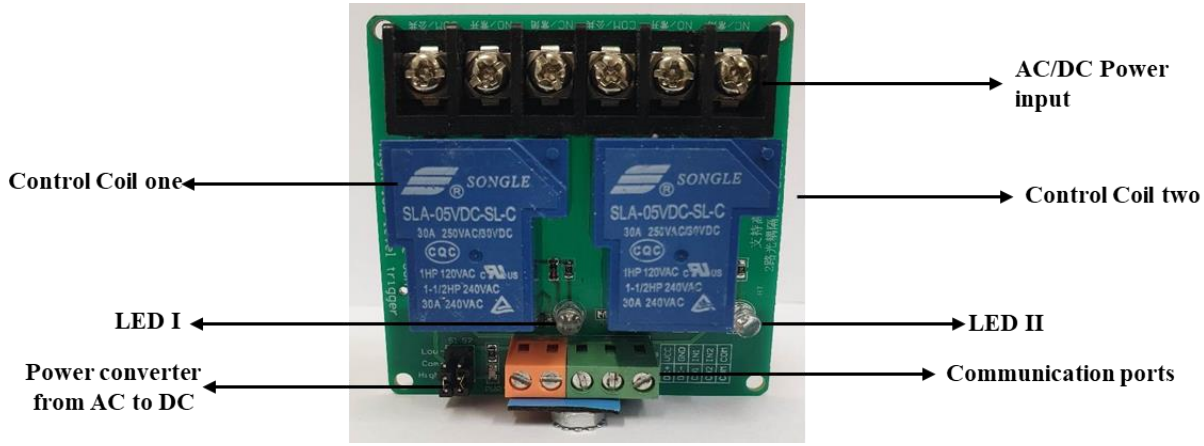

Figure 3.15: 12–240-volt relay module used in controlling the dredging and jet pump system of the EPRSDC

As shown in figure 3.15, the 2-way power relay controller is used for high or low signal trigger. It is designed to control a load of up to 30A. The relay system module has a reliable power relay system with an ultra-small packaged optocoupler, high-power high-voltage transistor, red blue signal light, military-grade double-sided PCB, and a cloth board. The two SEAFLO BILGE pump power cable was connected to channels one and two of the relay board. The relay was powered by the 12V Nickel Metal Hydride (NiMH) 3000mAh capacity 10-cell battery. Furthermore, for us to control the pumps switch, we connected a 9-volt Duracell plus power battery. After achieving the required results manually, we integrated software algorithms using LabVIEW and NI myRIO to control the system with a UI. The +myRIO control board adapter digital input 1 was connected to the positive terminal of the pump positive and ground served as the negative terminal.

3.4 Setup for the venturi dredging system

This section presents the design of the jet pump nozzle used for breaking the ocean floor for direct and easy accessibility to material beneath the seabed. The 12-volt seaflo bilge pump was mounted on the shaft of the crawler with the water inlet facing the horizontal flow direction. After sucking water through the pipe based on the directional placement, we then designed a reducer which reduced the cross-sectional area and increased the velocity of the water passing through the pipe. This reducer can also be called a venturi reducer.

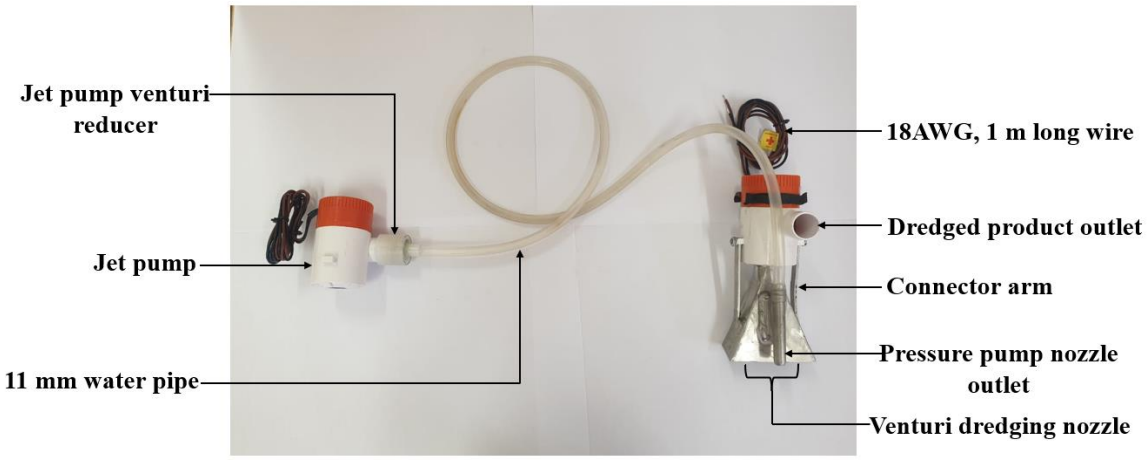

Figure 3.16: setup for the venturi dredger, jet pump reducer, and breaking nozzle for the EPRSDC

As presented in figure 3.16, the setup of the dredging system comprises of six main parts which will be discussed further in the report. The 1050 series aluminum venturi dredging nozzle design weighs 0.1293 kilograms, with an overall length of 125mm and breadth of 90mm. The aluminum sheet was cut to size and was welded using the TIG315PAC/DC THERMAMAX aluminum welding machine. The jet breaking nozzle was machined out of a 12mm aluminum alloy rod and was drilled through with a 6.5mm drill bit. An 11mm OD clear PVC tubing water pipe was connected from the jet pump nozzle to the reducer of the bilge dredging pump outlet. The reducer was machined out of a high-density polyethylene (HDPE). The HDPE on one end has a diameter of 28.5mm and was reduced to 8.5mm to fit the radius of the pipe. The jet venturi dredging nozzle system was designed to increase the speed flow of fluid (water) by constricting it to a cone shaped tube. The flow of fluid through the reducer causes an increase in its velocity, while reducing its pressure and producing a partial vacuum draw in the system.

3.5 Software used

We used the Laboratory Virtual Instrument Engineering Workbench (LabVIEW) to automate the control system for the scaled down prototype of the EPRSDC. LabVIEW was used as the programming language for the EPRSDC. In the programming environment, control block diagrams were created to implement a UI for controlling the system. The UI enabled easy control for the drive system comprising of both track systems, the boom arm, the dredging pump/jet pressure pump control, the camera and finally the lighting.

3.6 SOLIDWORKS 2020 student version

The first step to achieving the design was to design all the components of the EPRSDC in fully defined details. We proceeded with designing two CAD models which included the first test design and the final design using solidworks 2020 student version. On the first model, we used the prebuilt Tetrix max solidworks parts design to assemble the electric powered robotic subsea dredging crawler parts. Afterwards, we designed the crawler using a 25mm x 25mm iron steel tube for the final manufacture of the scaled down model of the EPRSDC. The solidworks model for this project were used to visualize all mechanisms for the model.

3.7 FEA using SOLIDWORK 2020 student vision

We performed FEA to simulate static loading conditions for the structural frame of the EPRSDC. This helped to determine whether the model would fail, wear out, or successfully perform the task it was designed for.

3.8 Physical test environment for the EPRSDC

AMTL Land test center: We used the AMTL-LAB as our dry land test center facility to determine the track driving performance under certain angle of inclinations.

3.9 The EPRSDC final design using 25mm x 25mm square steel tube

In achieving the final design, we used the 25 x 25mm square hollow section tube pipes with wall thickness of 2 to 3mm and total weight of 1.43 to 2.04kg/m. After series of simulations and experiments (covered in chapter 4), we settled at using the 25 x 25mm square hollow section tube pipes for the final design and manufacturing of the electric powered robotic subsea dredging crawler. We used a 3mm flat bar for the crawler wheel arm extension of the tank tread idler which formed the hexagonal shape.

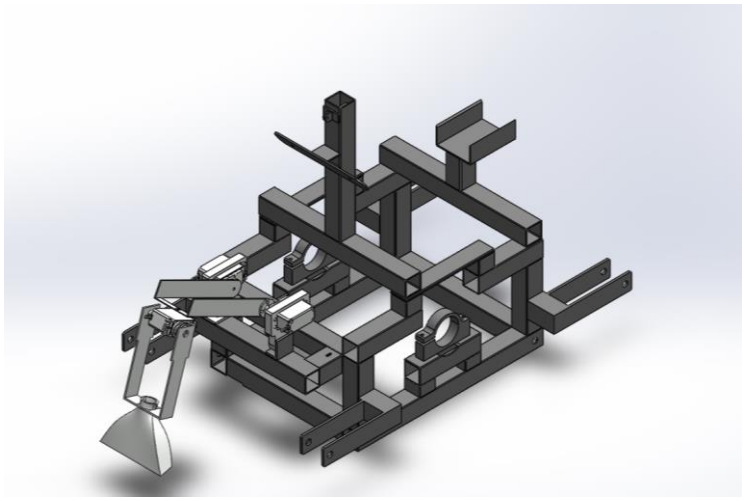

Figure 3.17: final design using 25 x 25 square tube pipe used in manufacturing the EPRSDC

Figure 3.17 above presents us with the undercarriage final design of our electric powered robotic subsea dredging crawler. The structural parts using 25 x 25mm square hollow section tube pipes were assembled using the SOLIDWORKS mate feature. We also used SOLIDWORKS mass properties to determine the weight of the undercarriage design which is 13.8kg.

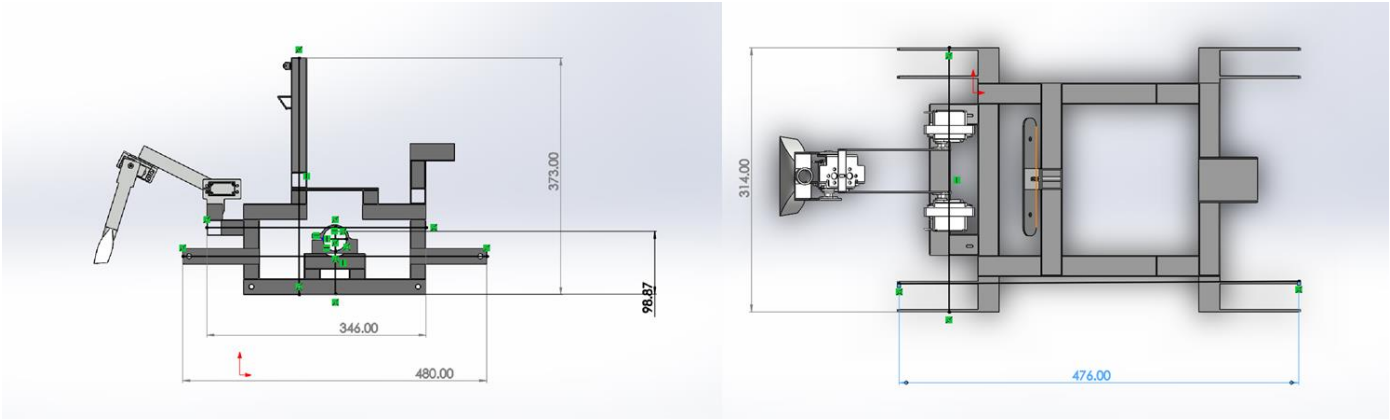

Figure 3.18: front view and top view measurement of the EPRSDC using 25 x 25 square hollow section tube pipe rages

In figure 3.18 we showed a methodological approach used in achieving the measurement of our design. The total length of the electric crawler viewing from the front is 346mm and the breadth is 373mm. Viewing the design of the crawler from the front direction, the drive chain extension arm system which we used a 3mm flat bar is 480mm in length and has a breadth of 98.8mm. Viewing the design from the top, the arm extension to arm extension has a length of 314mm and breadth of 474mm.

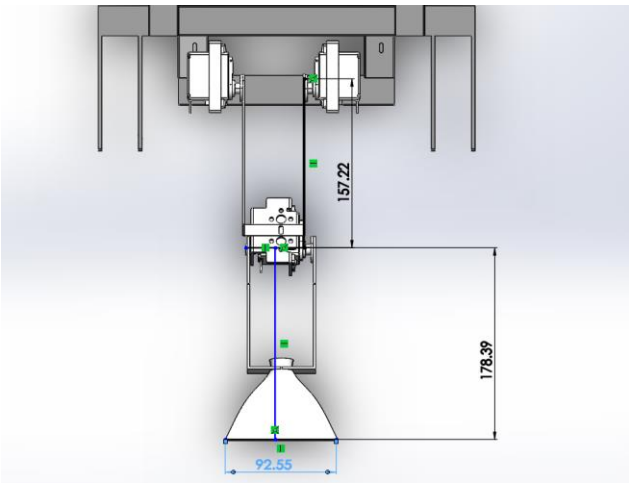

Figure 3.19: dredging arm measurement and total weight

In figure 3.19, we presented more details on the overall measurement, weight, and modifications done on the 2DOF arm dredging pump. The first joint uses two servo motors each producing a maximum torque of 25kgcm and consuming 6.8-volt DC current. The shafts of the first joints were set facing each other with a distance of 28mm. The total distance from the first shaft to the arm is 158.22mm and the second shaft to the venturi dredging nozzle is 178.39mm. The total length of the 2DOF dredging arm is 336.61mm with a breadth of 92.55mm. Both the arm and dredging venturi nozzle are made of 1050 series aircraft grade aluminum. The 2DOF arm has a weight of 0.58kg.

3.10 Logitech brio 4k ultra-HD webcam stream edition pro waterproofing concept and design

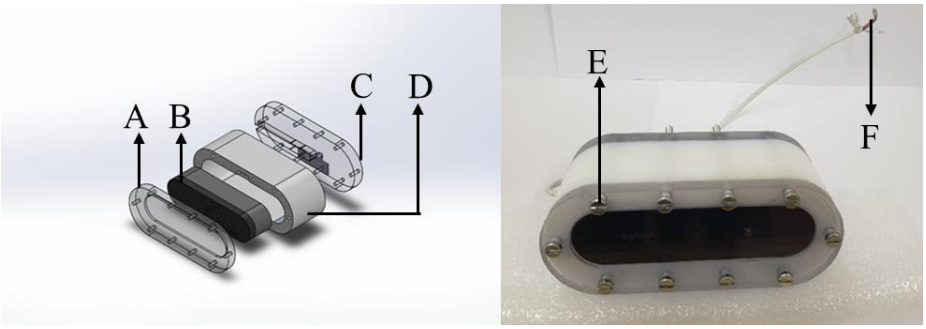

Figure 3.20: waterproofing system of the Logitech brio 4k ultra-HD of the EPRSDC

In figure 3.20 we listed the parts used in waterproofing the Logitech brio 4k ultra-HD webcam stream edition. The parts are as follows:

- A= is a 10mm Perspex transparent plastic with a length of 103mm and a breadth of 48mm.
- B= Logitech brio 4k ultra-HD camera.

- C= The rear Perspex transparent plastic with the length 103mm and breadth of 48mm used in covering the camera and keeping the wires in place.
- D= High-density polyethylene (HDPE) with a length of 103mm, breadth 48mm, camera deep 29mm. This polyethylene has a wall thickness of 10.90mm.
- E= 5m galvanized bolts and nuts
- F= type C USB L cable O-COPPER with power and communication wires.

The parts were designed using SOLIDWORKS and manufactured using a Computerized Numerical Control (CNC) machine. A-D were assembled, and silicon was applied in-between A, C and D and we used a 5m bolt and nuts to torque and pull the design components together. The four assembled components have a total weight of 0.3762kg. The camera was operated and controlled with a wire, and the 4K ultra zoom was stabilized with the Logitech application for cameral control system.

3.11 12-volt DC Tetrix Max torquenado motor waterproofing for the final design concept

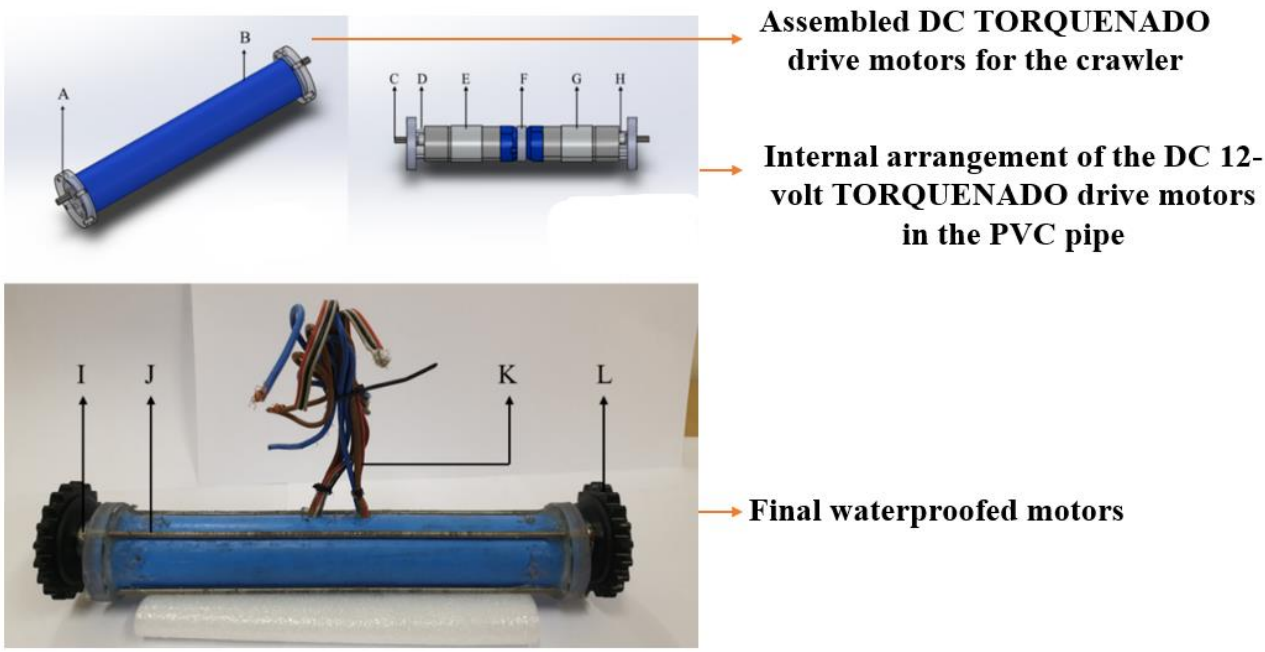

Figure 3.21: waterproofing concept of the Tetrix Max torquenado motor

The 12-volt DC Tetrix Max torquenado motor for the final design as shown in figure 3.21 was waterproofed to enable it function under 1.5m in CPUT swimming pool. The DC motor waterproofing concept was achieved with the following parts and assembling process.

- A= 10mm Perspex transparent plastic with an outside diameter of 45mm and an inside diameter of 40.50mm.
- B= 40mm PVC pipe with the total length of 260mm
- C =6mm shaft.
- D= 4mm threaded bar with the length of 7mm.
- E= starboard 12-volt DC Tetrix Max torquenado motor.
- F= 10m spacer with an outside diameter of 37mm.
- G= Portside 12-volt DC Tetrix Max torquenado motor.
- H= 5mm valve stem oil seal.
- I= Tetrix Max motor hub.
- J= 5mm threaded bar with the length of 275mm
- K= 12-volt DC wire connector with communication lids.
- L= Tetrix Max Tank Tread Sprocket.

The above parts when assembled together has a total weight of 1.0468kg. The 10mm Perspex transparent plastic with an outside diameter of 45mm and an inside diameter of 40.50mm was machined to fit the outer radius of the 40mm PVC pipe. The 10mm perspex was drilled throught with a 6mm drill bits to enable the motor shaft fit in. A 4mm threaded bar with a length of 7mm was used to create a distance from the perspex and the starboard/portside 12-volt DC Tetrix Max torquenado motor from rotating under motion in the PVC pipe. We used a 10mm spacer with an outside diameter of 37mm to separate the portside and starboard motor in the PVC pipe. To prevent water from paving its way through the 6mm drilled shaft outlet, we used a 5mm valve stem oil seal rotating it to face the opposite direction to the machined 10mm Perspex transparent plastic. Silicon was pumped in the distance created using the 4mm threaded bar with the length of 7mm. Finally, both motors were forced into the PVC pipe and covered end to end with the Perspex transparent machined plastic. The 5mm threaded bar with the length of 275mm was used to pull and fasten the two Perspex transparent.

3.12 The umbilical cord and specifications

The umbilical cord is a 1.5m 36 core screened industrial cables tethered from the crawler to the control box. The control box can be connected over Wi-Fi having a range of 100m. The control box houses the following components: NI myRIO, motor controller, servo motor control, the pumps, camera cable, and the lighting systems.

Table 3.10: Umbilical cord Wire specification

Description	36 cores 0.20.22mm^2 screened PVC insulated and sheathed industrial cable
conductor	7/0.2mm tinned copper (nominal construction)
Insulation	PVC 0.3mm normal thickness 1.2mm normal diameter.
Braid shield	PVC 0.75mm normal thickness to 10.7mm normal diameter.
outer diameter	10mm
Conductor Resistance	92Ω/km max at 20^0C
maximum operating temperature	-15^0C +80^0C
Current Rating	Current rating are carrying capacities for multi-core cable are not given owning to the varied conditions of loading a construction or project. However, for guidance on this application, a single core of multiple cables is loaded, the current in a 7/0.2 conductor should not exceed 1 Amp
Voltage rating	440v at frequencies up to 1.6KHz
Sheath material	Polyvinyl chloride PVC

3.13 The control system using IP/Wi-Fi

The micro controller (NI myRIO) was connected to a surface pro windows laptop using an IP address. This framework can be used to control the robot over a distance of 100 meters. The global variables were used to store information while the program is running. The wireless network was configured from the settings of the wireless network on the myRIO, the system controller must be connected to the myRIO using a USB to configure the software. In order for you to have access and operate the programming software, LabVIEW must be installed on the computer.

3.14 Design and manufacture of the testing ramp for the EPRSDC

The developed EPRSDC required an angle testing ramp to determine the possible angles of inclination which it can effectively operate at. We designed a ramp which had a length of 1.8 meter and a width of 0.6 meter with five incline planes as seen in figure 3.24.

3.14.1 3-D design for the ramp

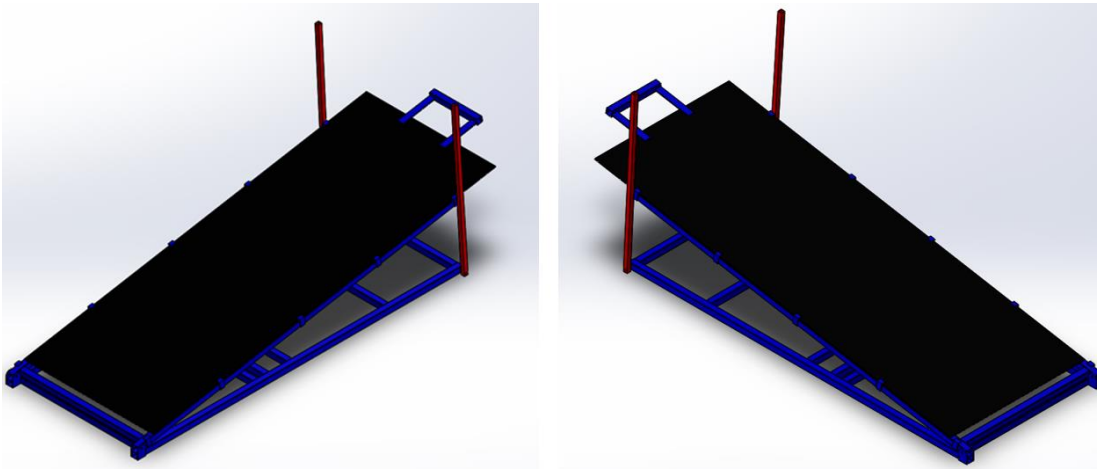

Figure 3.22: 3D SOLIDWORK conceptual Design of the ramp

Figure 3.23: structural frame of the test ramp

As seen in figure 3.23, during the experiment, the ramp was adjusted to the desired angle using the two arms with the holes to adjust the five degree of inclination which are 0^0 15^0 , 20^0, 25^0 and 30^0.When the height is adjusted, the crawler was operated to climb the ramp and the details of its operation during the process was recorded.

Figure 3.24: final design for the ramp describing the function

As presented in figure 3.24, the ramp was manufactured using 25 X 25 steel tube pipes and the climbing sheet was factory manufactured with 3 mm thickness. The Arm of the ramp was used as a stopper for the measured angle of elevation.

CHAPTER FOUR: ANALYSIS AND RESULTS

This chapter starts with presenting the CAD model and physical model of the EPRSDC. Afterwards, the User Interface (UI) was presented. The next section covers the drive test carried out and the corresponding control program used to handle mechanical errors in the driving system. After which the dredging test is discussed. The next section covers the drive experiments performed for 5 different angles of inclinations. FEA simulations on the EPRSDC preliminary design is presented next. The chapter concludes with some discussions on the specification of the final design.

This chapter presents us with analysis and results for our model which was built using Tetrix robotics kit. The EPRSDC was deployed to climb and descend under certain angles of inclination while moving along a distance of 1.8 meters. We recorded our results in six tables. We also took relevant pictures of the set up while carrying out the experiments. We considered the following relationships between some parameters which include:

1. maximum velocity versus the angle of inclination,
2. torque versus velocity at an angle of 0^0,
3. torque versus velocity at an angle of 20^0,
4. average minimum torque versus the five angles of elevation ($0^0, 15^0, 20^0, 25^0,$ and 30^0), and
5. efficiency versus torque at 0^0 and 20^0 angle of inclination

These relationships were used to evaluate the drive performance of the robot. This experiment was performed at AMTL-CPUT test center. All experiments were repeated three consecutive times and a stopwatch was used to time each run.

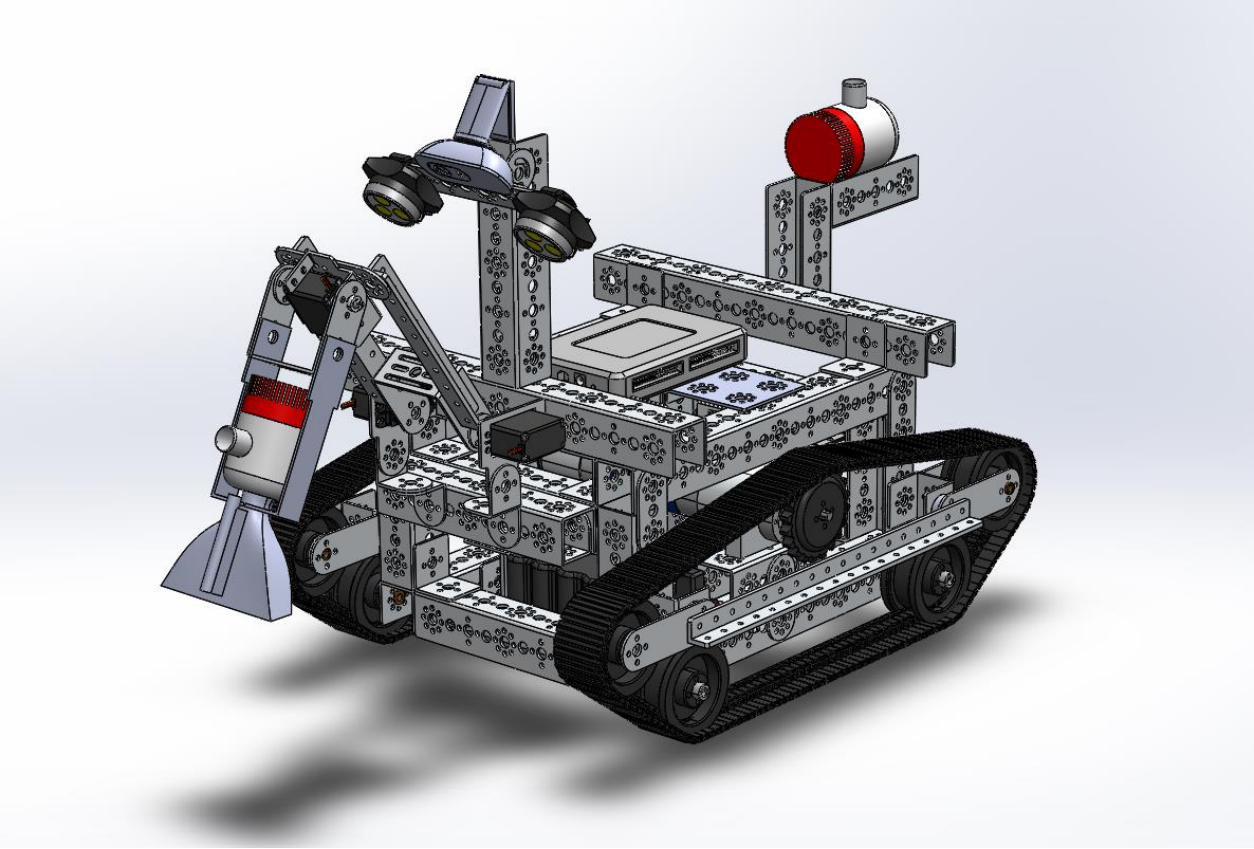

Figure 4.1: 3-D SOLIDWORKS design model of the EPRSDC's

As shown in figure 4.1, we used the SOLIDWORKS student version to model the EPRSDC. The software made it easier to adjust individual parts before the final design was assembled. This design is scalable and can be used for large-scale industrial manufacturing of the EPRSDC.

For this scaled-down prototype, all electronic components were appropriately placed using solidworks mates to achieve a realistic 3D visualization of the model. As shown in figures 3.1, 3.2, 3.3, and 3.4, the software was used to assemble the three undercarriage systems of the EPRSDC. It is necessary to design the robot's structural and hardware components using CAD software. This enables complete freedom and flexibility in the development process from the conceptualization to the manufacturing stage.

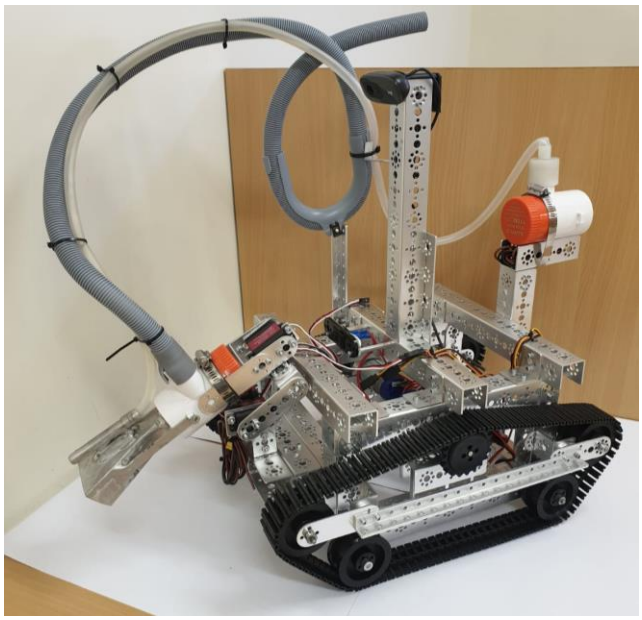

Figure 4.2: completed hardware design concept of the EPRSDC's

Figure 4.2 presents the structural technicalities of the assembled design. The model comprised of some electronic components such as a 12-volt DC dredging pump, a Logitech webcam camera, overhead lighting, motor controllers, Torquernado 12-volt DC motor, waterproofed servo motor, and the NI myRIO. For the driving base and frame chassis, the components used were the track frame (made of 1050 aircraft-grade aluminum), Tank tread chain link, Tank tread idler wheels, Tank tread sprockets, bronze bushing, motor hub, tank tread sprocket, tank tread idle wheel, motor mount and channels (96 mm, 160 mm, and 288 mm channels). The listed component served as the main structural support for the undercarriage frame which provided the track drive with a rolling surface. Most of the other components were mounted on the boom arm. The track tank tread chain link units differ from each other, but they can be interconnected to form a chain which pads can be mounted on. The chain can be made of steel or heavy-duty plastic depending on the manufacturer's application. The idler is a big roller having a cylindrical profile connected to the frame. The function of the track and carrier rollers are to support the track over the horizontal lengths to create an angular inclination for the ends of the tracks. The sprocket and idler track drive contain more track rollers than the carrier, the track rollers are used to secure the contact area between tracks.

4.1 User Interface (UI)

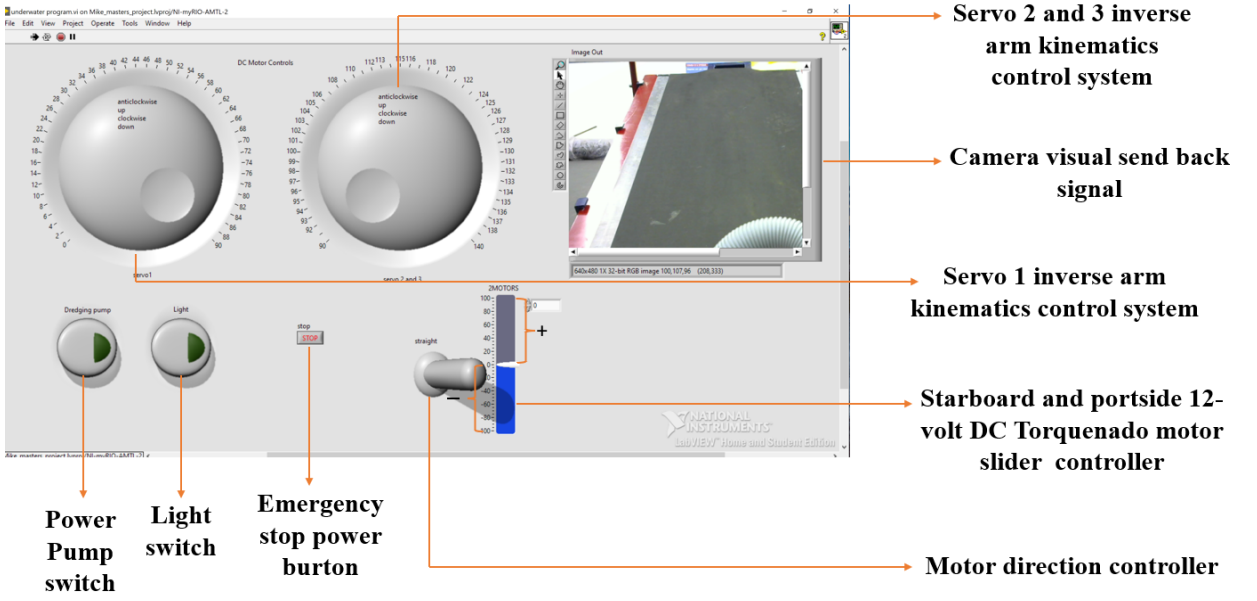

Figure 4.3: user interface control system platform designed using LabVIEW software algorithms

This figure 4.3 Is the Controller Unit (CU) which can also be called the User Interface. The software platform deploys instructions from the computer to the NI myRIO. This enables the crawler to perform certain functions. The knob servo controllers (1, (2 and 3)) were used to control the first and second joints of the 2DOF boom arm. Due to the of the arm (0.548kg), the servo motor was doubled at the 2nd joint (2 x 25kgcm), which gave us sufficient torque to lift its weight. For the arm which has a uniformly distributed load of (0.548kg), we multiplied the total arm length by the weight (0.54 x 15.5) to get the moment of the force acting on the arm, which was equal to 8.494kg/cm. The two-motor control knobs were calibrated for 0 to 100% to lift the arm on the first or second joint and – 0 to 100% to return the boom arm to its initial position. For the slider + 0 to 100% was used to move the EPRSDC forward and – 0 to –100 was used to move the EPRSDC backward. The motor controller switch button (straight) is used to change the direction of the drive system (clockwise and counterclockwise). The Emergency button was designed to shut down the entire control system during operation in case of program malfunction. The camera system was used to transmit real-time videos and pictures to the control room enabling the crawler pilot to see the operating environment. The pump and light switches were used to power on or off the dredging pump.

4.2 First performance test under 10^0 angle of inclination

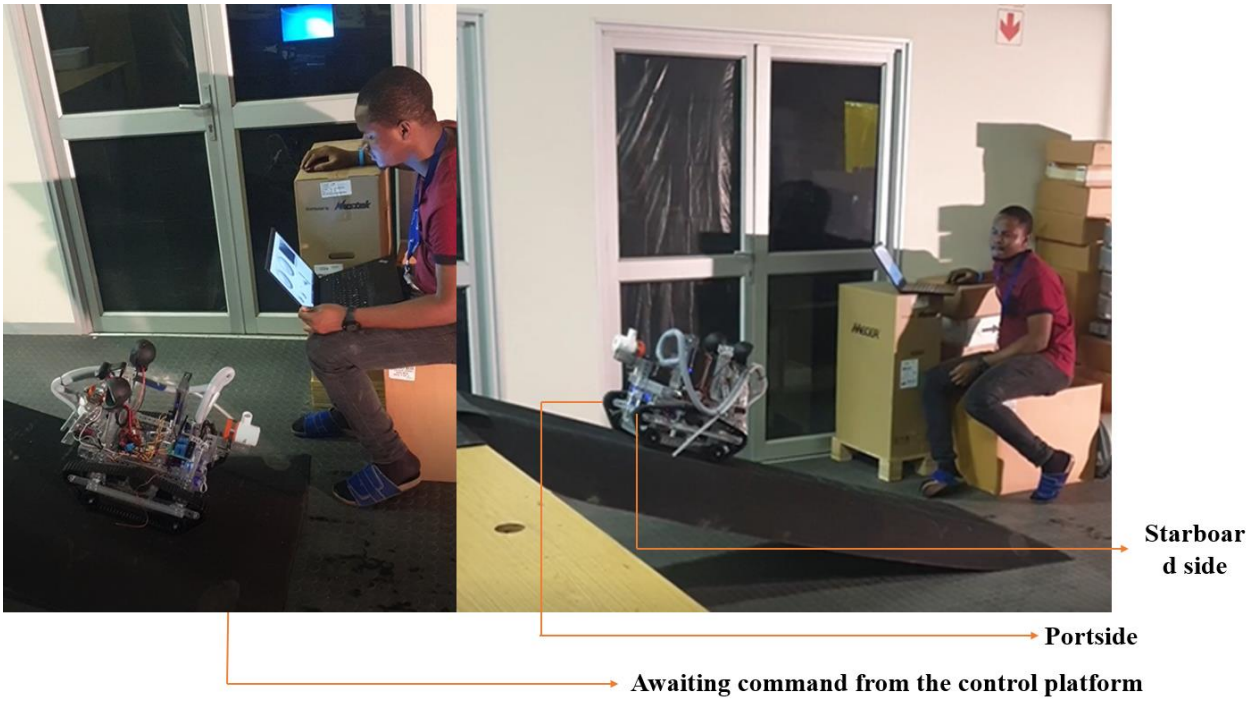

Figure 4.4: EPRSDC's first performance test over 10^0 angle of inclination

As demonstrated in figure 4.4, the EPRSDC followed commands from the operator using the software. After the command was sent from the computer to the microcontroller, the crawler made its first attempt at climbing the test angle. Due to the mechanical uncertainties, while both motors were powered at the same value, the portside 12-volt DC Torquenado motor was slightly faster than the starboard motor. This made the EPRSDC slightly skew to one direction while moving forward or backwards. We corrected this error by using our program to slightly increase the power supply on the disadvantaged motor to compensate for the skew and achieve movement along a straight path. We have shown the LabVIEW block diagram for our solution in Figure 4.5.

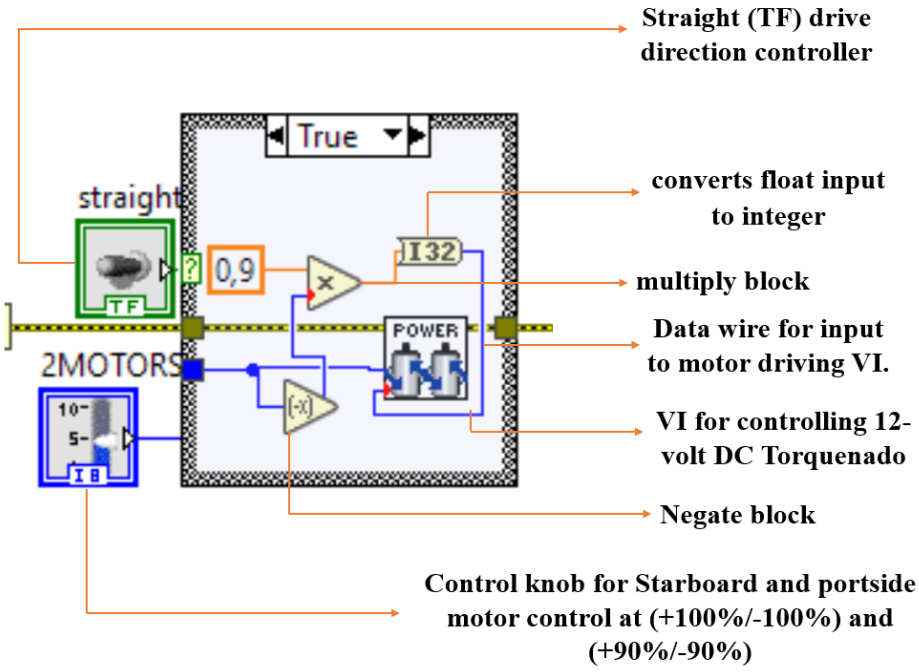

Figure 4.5: Programming blocks used to correct the drive system mechanical errors

As shown in figure 4.5, the above block diagram was used in adjusting the mechanical uncertainties affecting the structural design. As presented in the block diagram, the I32 was used to convert the float control number into an integer. The motor control block used for this system does not have the ability to control speed as a float input. The control slider for the starboard side ranges from +100% to -100% and portside motor +90% to -90% as presented in diagram above. The power for driving the portside was reduced by 10% to give the crawler a straight heading. The data wire connected to the input of motor driving VI came from the I32 block which converted the float number from the multiply block into an integer. Furthermore, the negate block was used to change the direction of one motor, considering that only one input was sent to the motor control blocks and both motors needed to turn in different direction to move the vehicle forward.

4.3 Dredging test for the EPRSDC's pump

Figure 4.6: dredging sand sediment from a lower to higher region

As seen in figure 4.6 The seaflo pump was used to dredge both sand sediments and water over 1.2 meters. This experiment was used to demonstrate the possible pump performance considering the newly designed venturi dredging nozzle. The pump performed decently, pumping sediment mixed with water from the collector to the discharge unit.

4.4 Experimental demonstration for the EPRSDC driving performance over certain angles of inclination

4.4.1 Maximum velocity versus different angles of inclination

4.4.1.1 This experimental image covers figure 4.7 to 4.11

This experiment presents the performance of the EPRSDC during its movement on the surface of the test terrain. We tried to recreate an ocean bed environment having flat surfaces and different inclined planes. The terrain was used to determine the crawler's performance in an unstructured environment having uneven grounds and obstacles which are different in dimensions and shapes.

Ocean tracked robots perform better when differential tank tracking system is used. The weight of the vehicle and contact between the tank tracks and the ground constrains the vehicle to a fixed position. Ocean crawlers need to have sufficient weight to have good traction with the ocean floor.

The subsea crawler was placed at the ramp's start position and the ramp was set at an inclination of 0^0 i.e., flat surface. It was observed from the experiment that two different types of slippages could occur during the movement of the vehicle. There could be slippage in the contact between the sprocket and the chain or in the contact between the chain link and the ground surface as shown in figures 4.7 and 4.11. These two cases can be corrected as seen in figure 4.5 and the recommended design as shown in figure 7.1.

As displayed in Figures 4.7 to 4.18, this shows that when the movement of the vehicle starts at its initial position, the third and fourth idle rollers are designed to lift up the crawler when approaching an elevated terrain. At some angles, it is difficult for the tank track chain link system to move the vehicle forward because of gravity which increases the slip. In some situations, the vehicle can climb steeper angles using a tank tread rubber attached to each chain link.

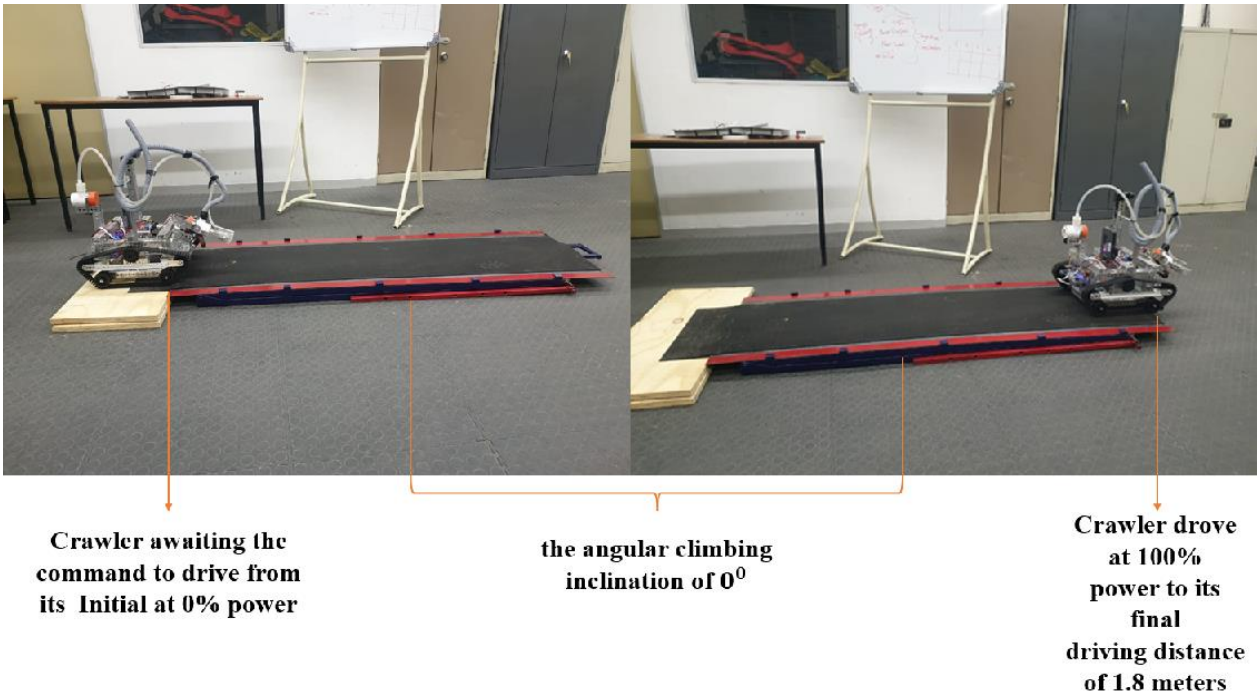

Figure 4.7: Drive test experiment for EPRSDC's at an angle of 0^0

The crawler was powered to its maximum value (100%) and the time taken to cover the ramp distance of 1.8 meters was recorded. After conducting this experiment three consecutive times, the average time taken was 5.9s

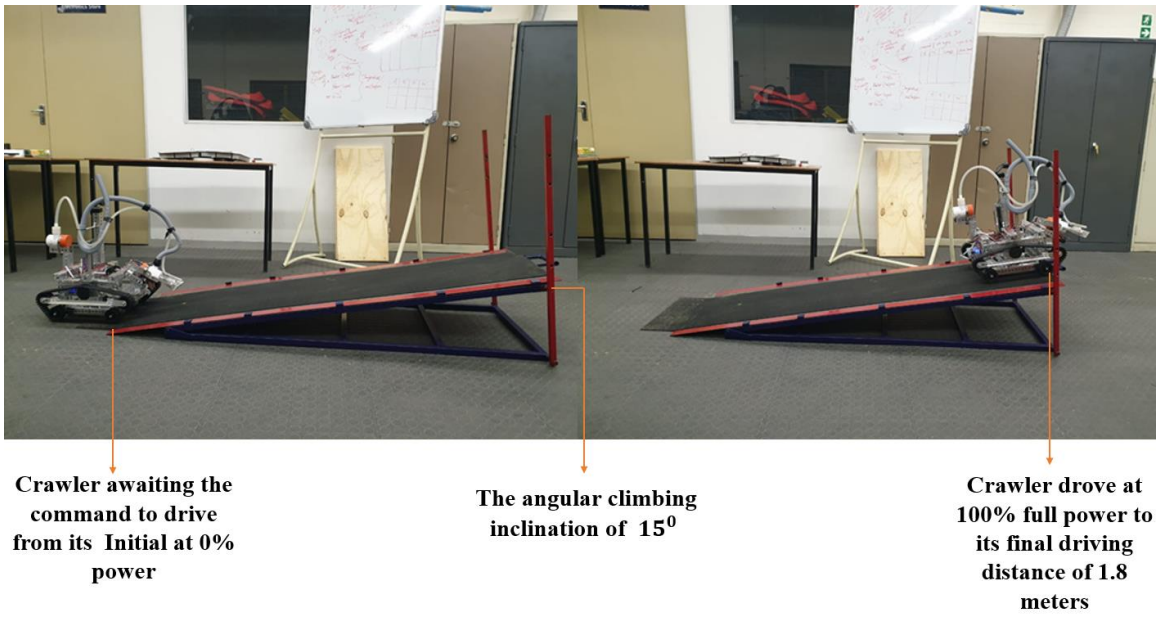

Figure 4.8: Drive test experiment for EPRSDC drive at an angle of 15^0

The crawler was powered to its maximum value (100%) and the time taken to cover the ramp distance of 1.8 meters was recorded. The ramp was inclined at 15^0. After conducting this experiment three consecutive times, the average time taken was 9.0s.

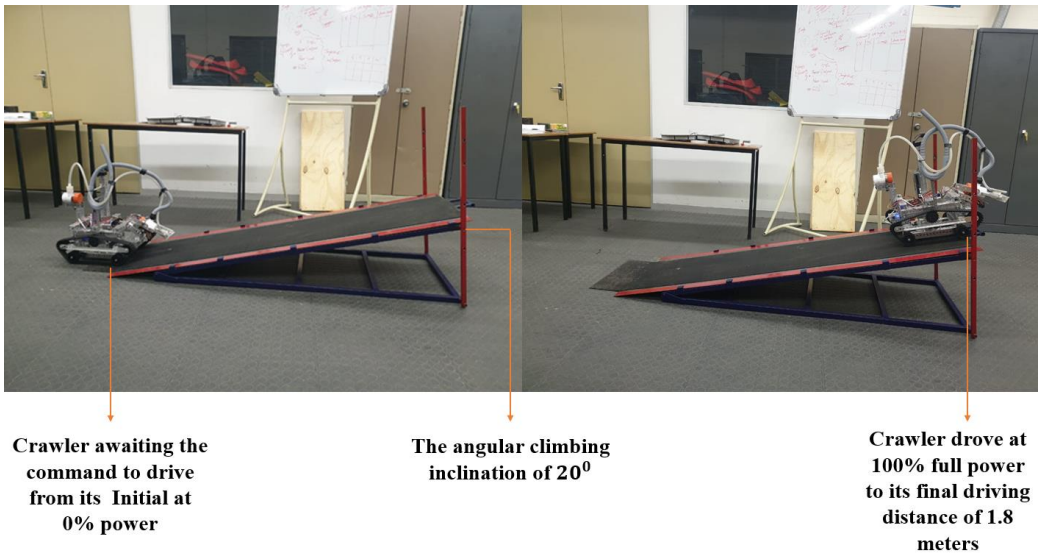

Figure 4.9: Drive test for EPRSDC at an angle of 20^0

The crawler was powered to its maximum value (100%) and the time taken to cover the ramp distance of 1.8 meters was recorded. The ramp was inclined at 20^0. After conducting this experiment three consecutive times, the average time taken was 7.2s.

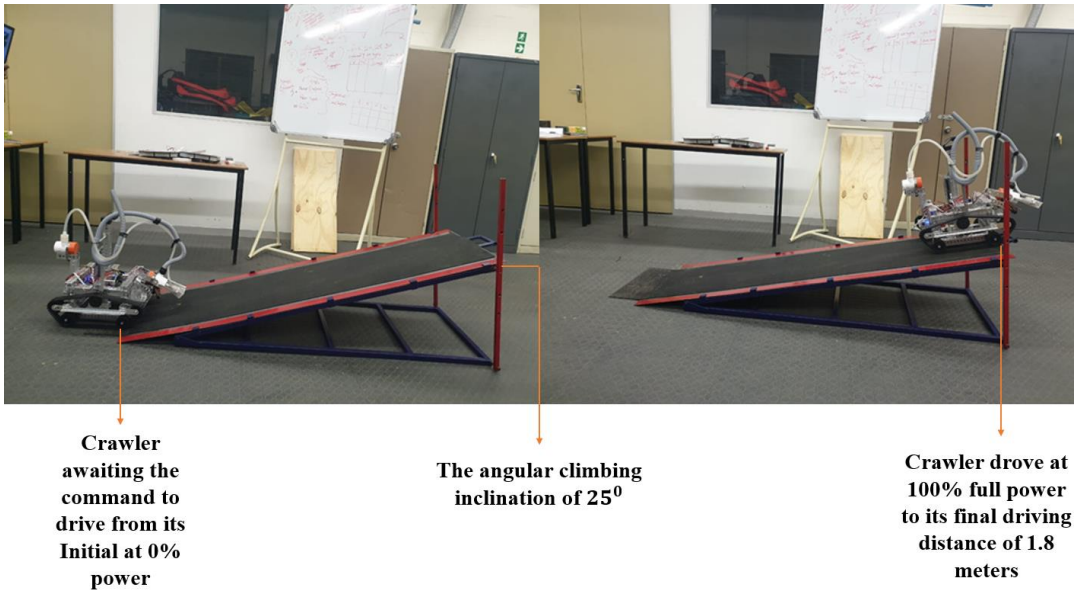

Figure 4.10: Drive test for EPRSDC at an angle of 25^0

The crawler was powered to its maximum value (100%) and the time taken to cover the ramp distance of 1.8 meters was recorded. The ramp was inclined at 25^0. After conducting this experiment three consecutive times, the average time taken was 8.5s.

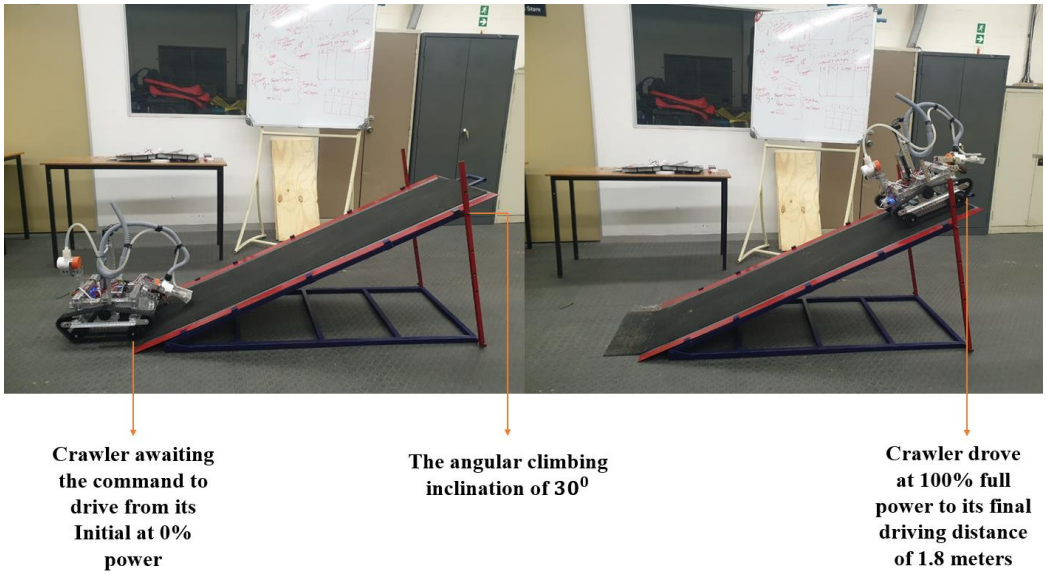

Figure 4.11: Drive test for EPRSDC at an angle of 30^0

The crawler was powered to its maximum value (100%) and the time taken to cover the ramp distance of 1.8 meters was recorded. The ramp was inclined at 30^0. After conducting this experiment three consecutive times, the average time taken was 9.9s.

4.4.2 Torque versus velocity at 0^0 angle of inclination

4.4.2.1 This experimental image covers figure 4.12 to 4.13

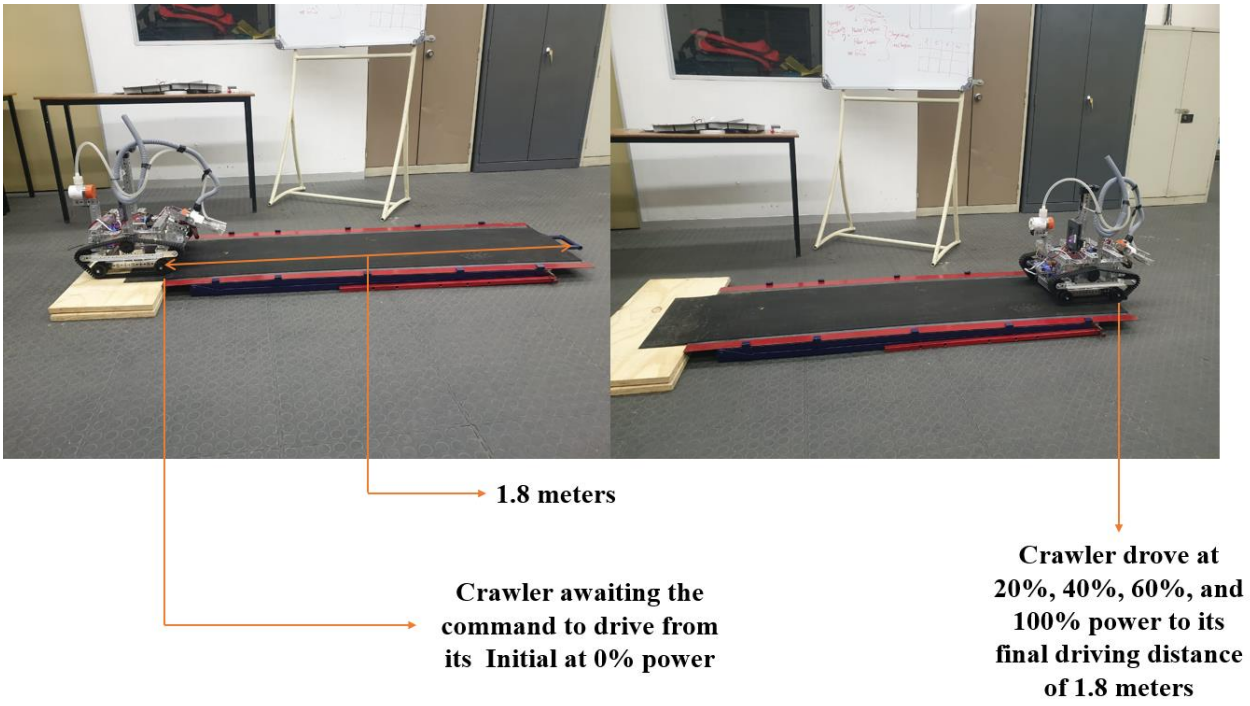

Figure 4.12: Drive test of EPRSDC at an angle of 0^0

The experiment showed the relationship between the torque and velocity at 0^0 angle of inclination. The time taken to cover the distance of 1.8 mm at different torque values was recorded. From the UI, we increased the motor power to five different values as shown below:

- At 20% of maximum power, the crawler did not move. This shows that from the power range of 1% to 19%, the crawler which weighs 8.173kg made no attempt to move forward.
- At 40% of maximum power the crawler took 25.7s to complete the task.
- At 60% of maximum power the crawler took 12s to complete the task.
- At 80% of maximum power the crawler took 7s to complete the task.
- At 100% of maximum power the crawler took 6s to complete the task.

4.4.3 Torque versus velocity at 20^0 angle of inclination

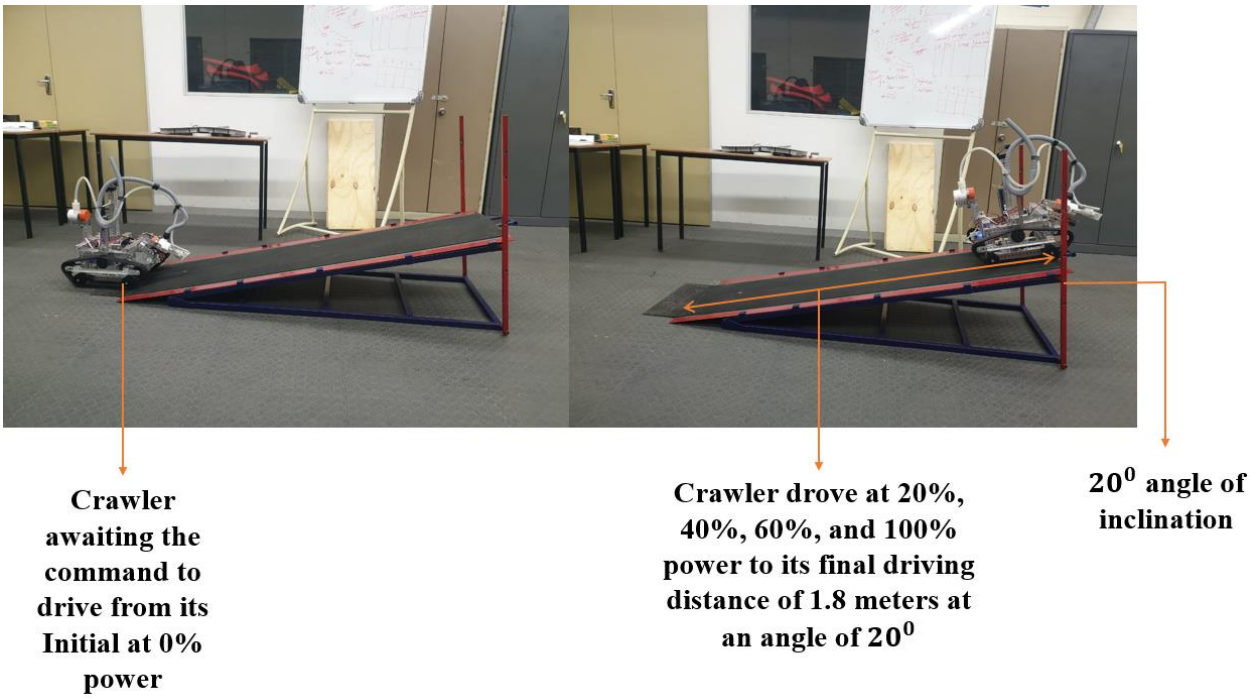

Figure 4.13: Drive test for EPRSDC at an angle of inclination 20^0

The experiment shows the relationship between torque and velocity at 20^0 angle of inclination. The time taken to cover the distance of 1.8 mm at different torque values was recorded. From the UI, we increased the motor power to five different values as shown below:

- At 20% of maximum power, the crawler did not move. This shows that from the power range of 1% to 19%, the crawler which weighs 8.173kg made no attempt to move forward.
- At 40% of maximum power the crawler took 41s to complete the task.
- At 60% of maximum power the crawler took15s to complete the task.
- At 80% of maximum power the crawler took 9.9s to complete the task.
- At 100% of maximum power the crawler took 7s to complete the task.

4.4.4 Minimum Torque versus different angle of inclination

4.4.4.1 This experimental image covers Figure 4.12 to 4.16

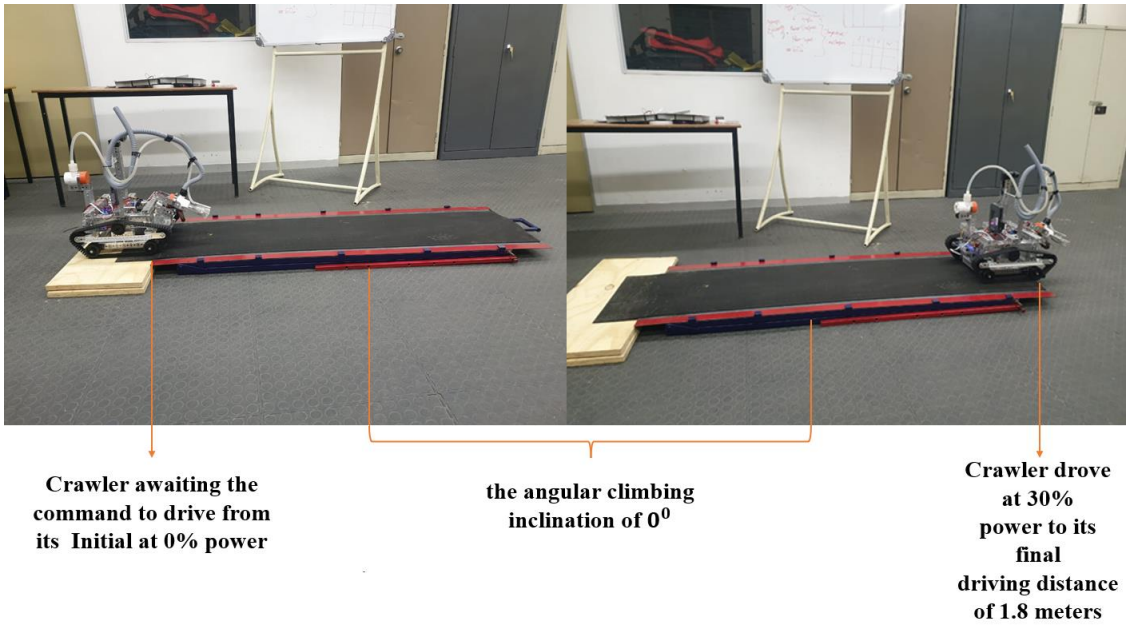

Figure 4.14: EPRSDC at an angle of inclination 0^0 and minimum torque of 30% maximum torque

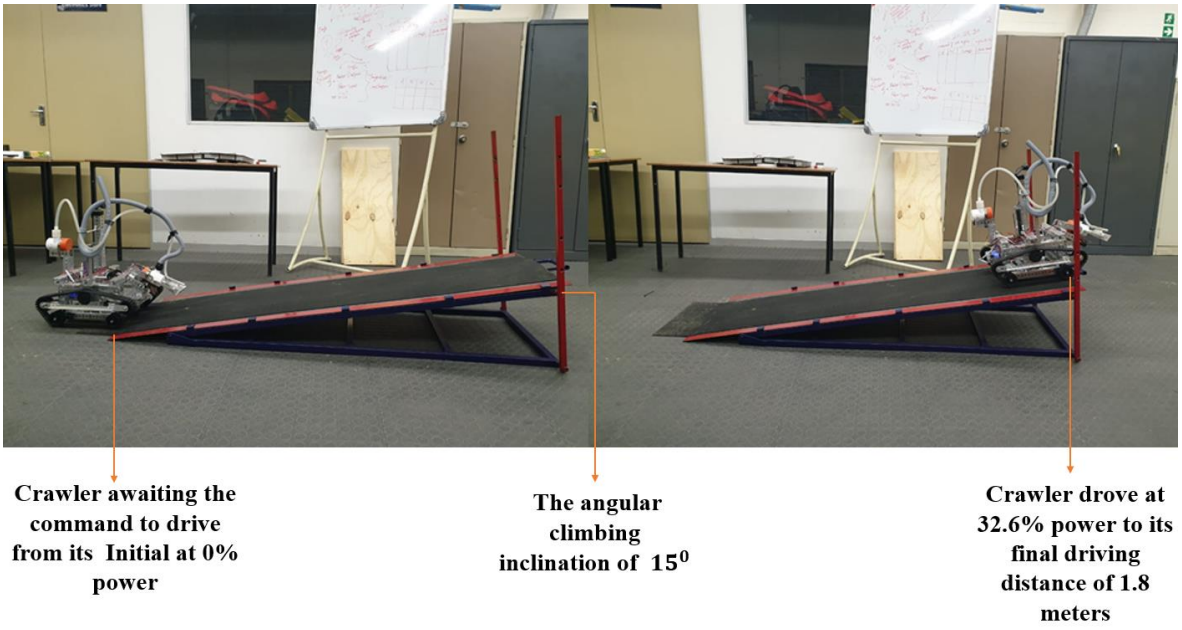

Figure 4.15: EPRSDC at an angle of inclination 15^0 and minimum torque of 32.6% maximum torque

Figure 4.16: EPRSDC at an angle of inclination 20^0 and minimum torque of 34.3% maximum torque

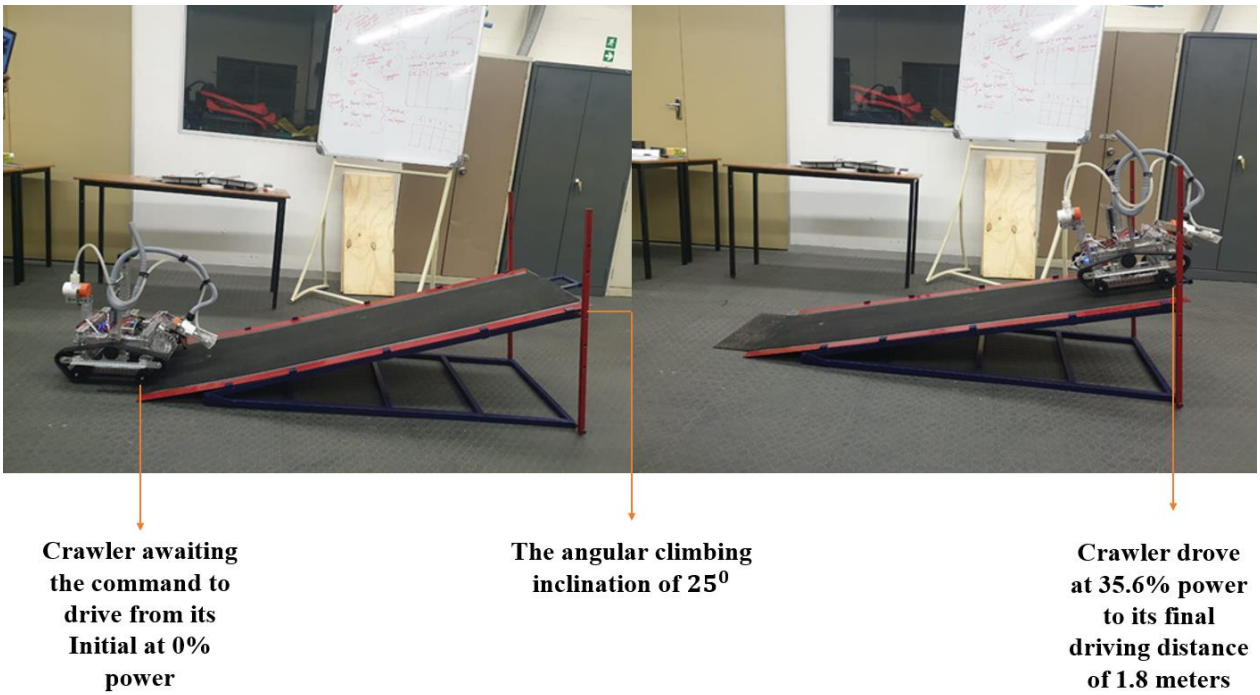

Figure 4.17: EPRSDC at an angle of inclination 25^0 and minimum torque of 35.6% maximum torque

Figure 4.18: EPRSDC at an angle of inclination 30^0 and minimum torque of 37.3% maximum torque

4.4.5 Results on EPRSDC motion on an inclined surface

The aim of driving the EPRSDC on the ramp was to determine the drive characteristics in different terrain simulated by inclined surfaces. The robot was driven up the ramp through a distance of 1.8 meters. We recorded the time in seconds starting from the initial to the final point in different angles of inclination from 0^0 to 30^0. The crawler could successfully climb different slopes under different climbing modes. The prototype had some limitations with climbing certain angular inclinations. This limitation is due to the power rating of the motor, the weight of the crawler and the steepness of the angles used in this experiment. The robot's total weight was 8.173kg.

tables 4.10 and 4.11, show the values of torque and velocity at 0^0 to 20^0. The tables can be used to show the relationship between the torque and maximum velocity. The experiment further disclosed the transitions between advancing mode (initials at 0 power) and climbing mode which is triggered by different torque (20%, 40%, 60%, and 100%). The first drive test was performed at 0^0 under the former mentioned torque percentages. The ramp was later increased to 20^0 to determine the time taken to complete each task at certain torque percentage.

4.4.6 Experimental drive test on uneven and soft ground terrains

It is very important to understand the driving dynamics in ocean crawlers. During our experiment, the rotation of the tank tread chain link was sometimes affected by slippage occurring on the surface of the 3 mm ramp plate. After we covered the ramp with a rubber-made material about 3mm thick, the transition between advancing mode and climbing mode resulted in better drive performances.

4.4.7 Energy consumption for scaled-down design of the EPRSDC

The purpose of this experiment for energy consumption is to evaluate the energy required for running the EPRSDC. We used two motors powered by a 12v battery. The track carried a load of 8.174kg and moved in different terrains. This set up showed a decent performance in its energy consumption over some period of time.

We observed that on full charge, during the experiment, the battery lasted for about 3-4 hours for each category. On full charge, the battery is capable of powering a 12-v motor that drives 5km. The battery used was a removable 12-v 3000mAh Nickel Metal Hydride (NiMH) 10 cells battery.

The NiMH technology provided significant advantage in battery energy-to-weight ratio which helped our crawler. The battery was also environmentally friendly during this experiment with no environmental pollution such as leakages in cadmium, lead, mercury, or lithium which are composite of batteries. The above-mentioned battery had a relatively high self-discharge rate compared to most available battery technologies making them stable for long-term energy storage.

In the recommendations section of this thesis, we proposed that NiMH battery can provide us with better result outputs for the mechanical system optimization. Hou et al., (2021) compared the energy consumption modeling with the actual energy consumption measured in the actual power value during their experiment. The robot was reported to climb some certain inclinations. The energy consumption was compared with energy consumption in driving on flat ground surfaces. Graphs were used to illustrate the various relationships based on the power consumptions and mechanical efficiencies.

4.5 Static loading analysis of the EPRSDC's structural frame chassis made of 1050 aircraft grade aluminum

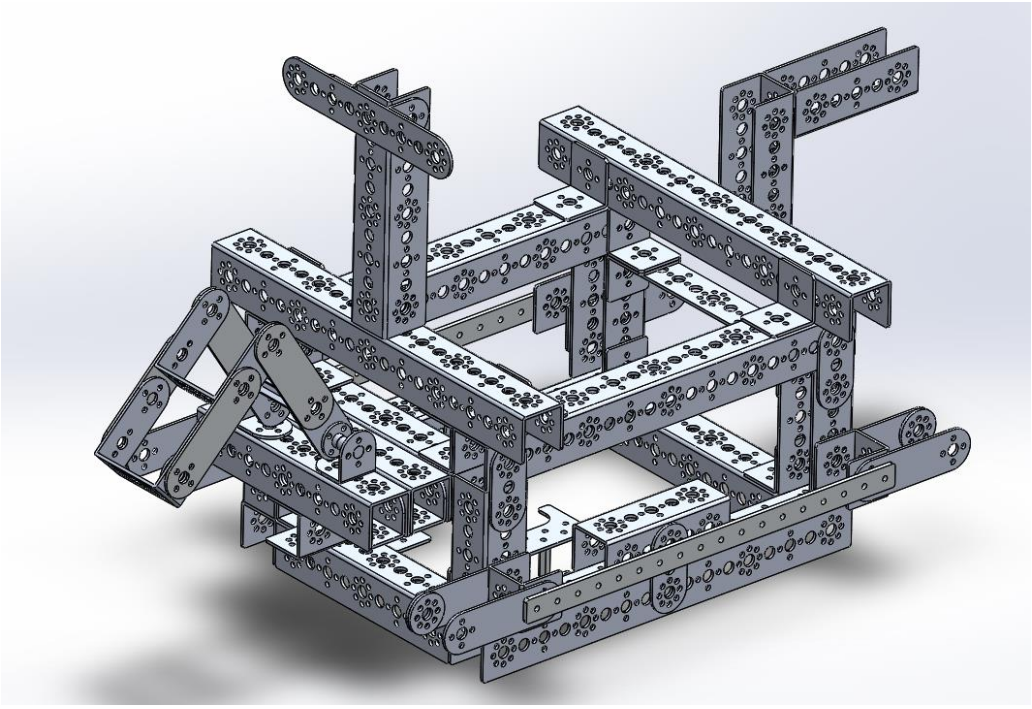

Figure 4.19: assembled structural frame of made from 1050 aircraft grade aluminum

The above frame presented in figure 4.19 was used to perform a simulation using FEA to determine if 1050 aircraft-grade aluminum can be used to develop future EPRSDCs. The weight of some components was measured. The component mass was used to load some certain points to determine the likely places that will deform.

For ocean applications, aluminum has been successfully used in manufacturing structural frames for Remote Operated Vehicles ROVs and Unmanned Surface Vehicles (USVs). This is due to their lower tendency to corrode in ocean applications. In 2014, Lozano & Dutra designed an ROV for pluvial application. Two different structural design for the frame was accomplished using 2024-T4 aluminum and the second one was an ASI 316 steel. The result was used to analyze the Minimum Tension (MT) and ocean Safety Fracture (SF). The aluminum alloy showed the best result for the test with 134.906 of MT and 4.64 in SF which refers to aluminum 2024-T4 normal car (NC) structures. This result shows that aluminum materials have promising mechanical characteristics that allow its use for underwater applications.

4.6 Material selection

The chassis is made up of 1050 series aircraft grade aluminum.

Table 4.1: shows the material properties for 1050 aircraft grade aluminum as gotten from solidworks software

Property	Value	Units
Elastic Modulus	3.7e+11	N/m^2
Shear Modulus	1.5e+11	N/m^2
Mass Density	3960	kg/m^3
Tensile Strength	300000000	N/m^2
Compressive Strength	3000000000	N/m^2
Yield Strength	----	N/m^2
Thermal Expansion Coefficient	7.4e-06	/K
Thermal Conductivity	30	W/(m·K)
Specific Heat	850	J/(kg·K)
Material Damping Ratio	----	N/A

This material was selected to match all typical traits of aluminum – strength, ductility, and comparative ease of design and machining. Furthermore, 1050 series aluminum has low risk of causing ocean pollution at sea. Furthermore, this frame chassis was simulated to determine the potential static strength of the structural design.

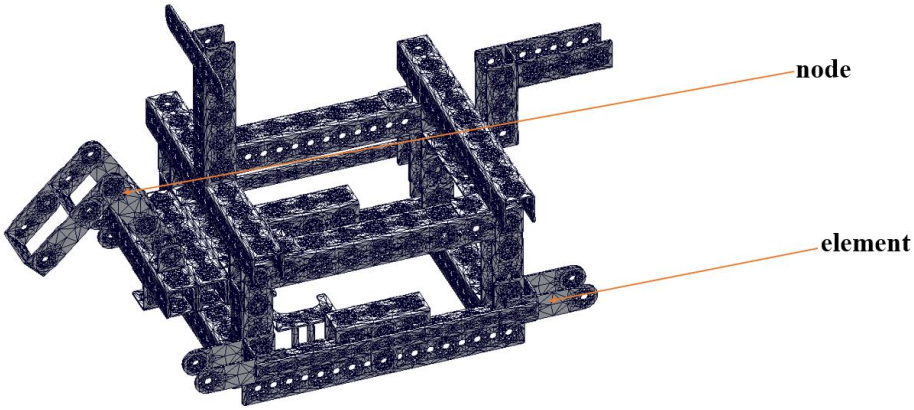

Figure 4.20: solid mesh of the structural frame for the EPRSDC's

Due to the harshness and unpredictable real-world application, the environmental forces should be considered in the certification of the preliminary design of the EPRSDC structure. This simulation deals with detecting different failures that are likely to compromise the structure of the robot. The mesh model of this as shown in Figure 4.20 draws a conclusive summary of the primary shell meshes which suggest the reference nodes as important items that relate to the chassis surfaces under compressional forces. These

also show the mesh spacing of shell model and structural variation. The nodes were used to coordinate location in the space where the DOFs are well defined in the aluminum. While the element found in the material are one specific node pointed out in the meshing.

Table 4.2: vendor's specification for the weight of components used for this analysis

Description	Size in (mm)	Weight in (g)
Channel	288	123.5
Channel	160	62.7
Channel	96	37.7
Flat	288	35
Inside connector C	--	8.4
Flat arm	--	11.2
Pivot	--	22

4.7 Calculation for the Static loaded force

Gravitational constant = 9.81m/s^2

4.7.1 First stage of static loading force

The force applied to this component caused the deformation as described using the alphabet A and B as seen in figure2.21 The distribution of the total weight acting on the specific structural components of the frame is calculated as:

= 62.7g + 123.5g (2) + 37.7g (2)

= 385.1g

= converting into kg $\frac{385.1}{1000}$ = 0.3851kg

9.81 x 0.388

= 3.773N

4.7.2 The pressure pump mount

Below is the calculated static load force applied to the pressure pump mount base as seen in the figure 2.22

- **Second layer**

  = 37.7g (2)

  = 75.4g

  = $\frac{75.4}{1000}$ = 0.0754kg

  = 0.0754 x 9.81 = 0.73N

4.7.3 Arm mount base

The weight of the components that makes up the arm was calculated and loaded to determine the static load acting on the boom arm base at its place of rest and during operation.

Third layer = 8.4g (6) + 6.27g (2) +11.2g (4) + 22g (3)

= 286.6g

= $\frac{286.6}{1000}$ = 0.2866kg

0.2866 x 9.81

= 2.808N

4.7.4 Four structural beam support

The four structural beams were responsible for taking the weight of the first layer, second layer, boom arm mount, and some other supporting structural components.

Fourth layer = 385.1g + 123.5g (2) + 75.4g + 286.6g

= 994.1g

= $\frac{994.1}{1000}$ = 0.9941

= 0.9941 x 9.81

= 9.74N

4.7.5 Final base structural support

The base support was responsible for carrying the total weight of the first to fourth layer structural frame with other sub-components that makes up the structure of the crawler. The weights were calculated and applied to the base support frame providing us with results to see the possible component(s) that are likely to deform under this static loading force.

994.1 + 35 (2) + 11.2 (8) + 37.7 (6)

= 1379.9g

= $\frac{1379}{1000}$ = 1.3799kg

= 1.399 x 9.81

= 13.52N

4.8 Simulated results for the structural frame made from 1050 aircraft grade aluminum

FEA was used to analyze the frame of the EPRSDC model to determine the strength of the frame using static loading force to illustrate likely real-world forces. The forces were applied at different components of the frame for the EPRSDC.

4.8.1 VonMises stress distribution

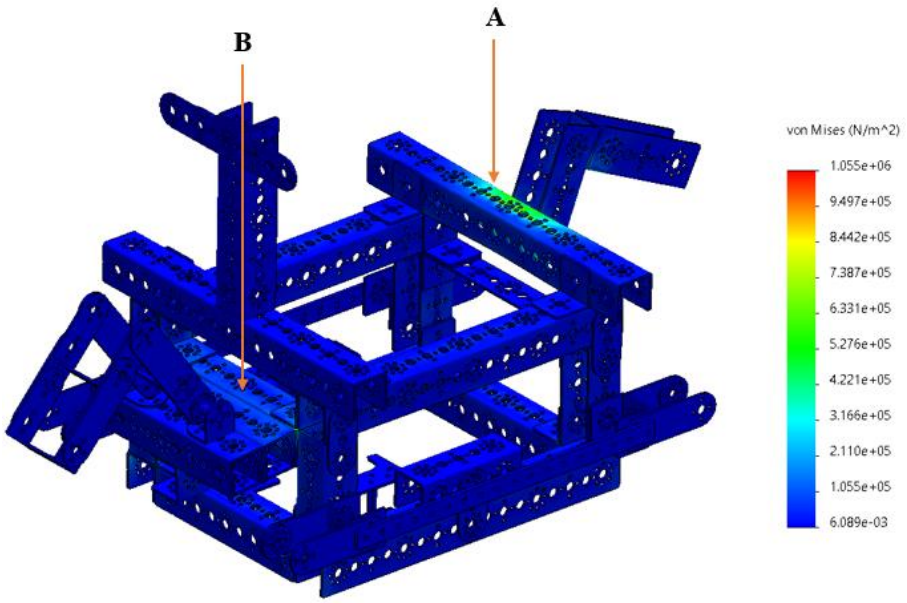

Figure 4.21: VonMises stress distribution on the EPRSDC

As presented in the figure 4.21 one of the most important parts of the analysis on this model is the VonMises stress distribution (active stress and residual stress) over the whole chassis of the EPRSDC. We can see that from the von mises stress distribution, the highest areas of concentration are in two positions A= pressure pump base and B the boom arm base. These stresses are seen to be in the region of 4.2 x 10^5N/m^2 and 7.38 x 10^5N/m^2 which are the pressure points as seen in green on the von Mises stress data table. This stress region is below the yield stress of the 1050 aircraft-grade aluminum. In conclusion, this material performed well under the loading conditions and has a low failure risk. This analysis shows that most of the components are within the blue region 6.08 x 10^3N/m^2 to 1.05 x 10^5N/m^2 which is safe for this model. Looking at this structural model from the Factor Of |Safety perspective, the FOS is above 3, which is acceptable. It is very important that the working stress of material should be 3 times lesser than its yield stress. The point of maximum stress concentration is below the yield stress which means that our model will not fail under the weight of its component.

4.8.2 Displacement

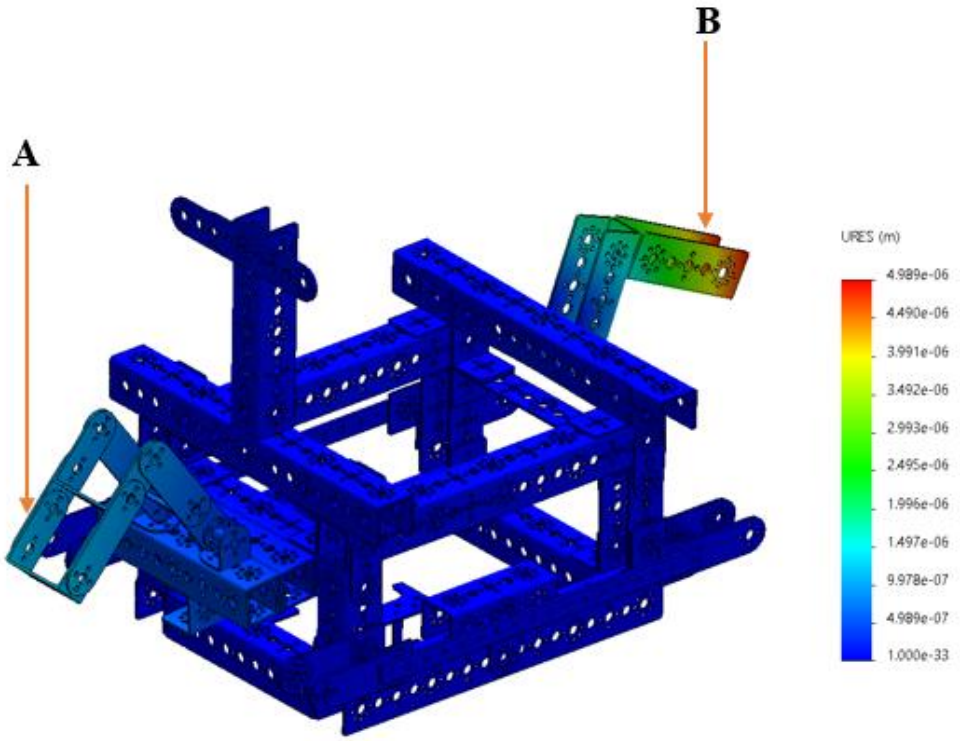

Figure 4.22: displacement on the structural frame of the EPRSDC

As seen in the above figure 4.22 the point of the maximum displacement was more visible on the boom arm(A) and pump mount base (B). The maximum displacement occurred at those points (A and B) because the moment of the force acting on the component is higher due to its longer perpendicular distance between the base point and the endpoint of the arm and the pump mount. It can be known that an increase in the distance between A and B, will lead to an increase in the maximum displacement of the structural frame. Based on this result, we recommend that the pump mount should be placed on the beam, and the arm will be supported with channels from under the base as seen in the design in our recommendation section (chapter 7). The point of maximum displacement is in the red region which is 4.9 x 10^{-6}m (0.0000498 mm). This result is acceptable considering that the displacement is significantly small and will have no effect on the performance of the crawler. In conclusion, the design can be improved or optimization to give us better performance. The range of displacement in the blue region is from 4.98 x 10^{-7}m to 1.0 x 10^{-33}m which shows that the vehicle can withstand its own weight under the expected operating conditions. This design can be improved by reinforcements or using a denser material.

4.8.3 Strain

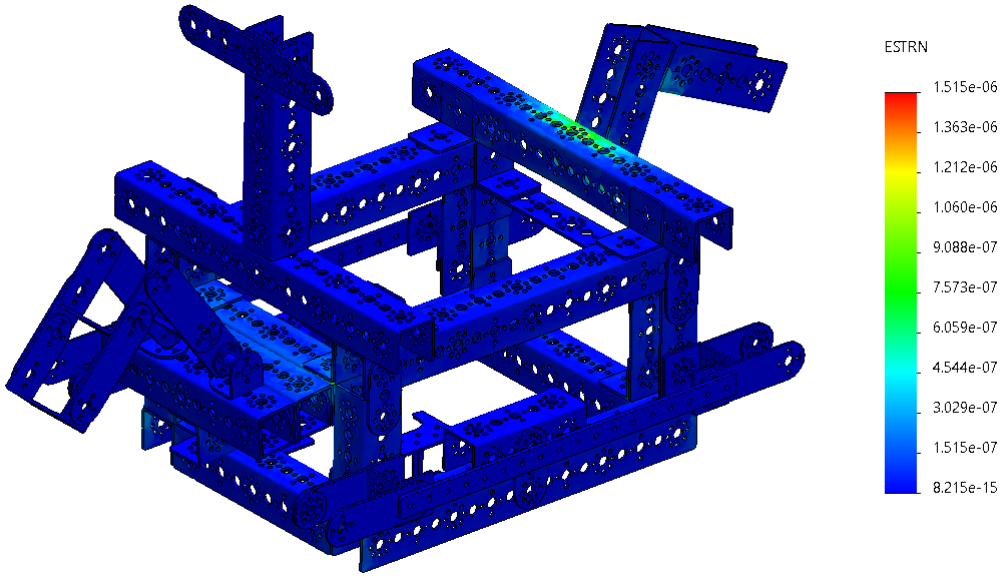

Figure 4.23: strain structural chassis of the EPRSDC

The strain as seen in the figure 4.23 shows us the deformation, physical change in size, and shape of the EPRSDC model under an applied force. Strain (ε) is the measure of the ratio of change in length to its original length of solid model material. We considered other strains during our observation; the metric is also known as the Cauchy strain. We should put into consideration that different materials have unique strain limits after which they will get into the point of failure which entails cracking and breaking. On our model as seen in the analysis, the maximum strain is 9.08 x 10^{-7}. We can also see that most of the material strain is around the blue region which is 1.5 x 10^{-7} which shows that most of the components used for the model are within their safe strain limits.

Medagedara & Chandra, (2012) discussed fatigue failures which are often initiated from points of stress on a model. The component used was designed in a complex geometrical way where it was subjected to alternating loads. The loads created multi-axial stress patterns. Furthermore, they presented a case study of fatigue analysis of industrial components. The industrial components included, structural chassis and their mode of deformation and cyclic pre behavior in its breaking stage. Such knowledge was said to be difficult to obtain when a non-proportional loading situation occurs. They concluded that notch simulations can be applied such as Neuber when analyzing models with higher frequency elements for different loading conditions present.

4.8.4 Plotted points of the affected part of the pressure pump mount

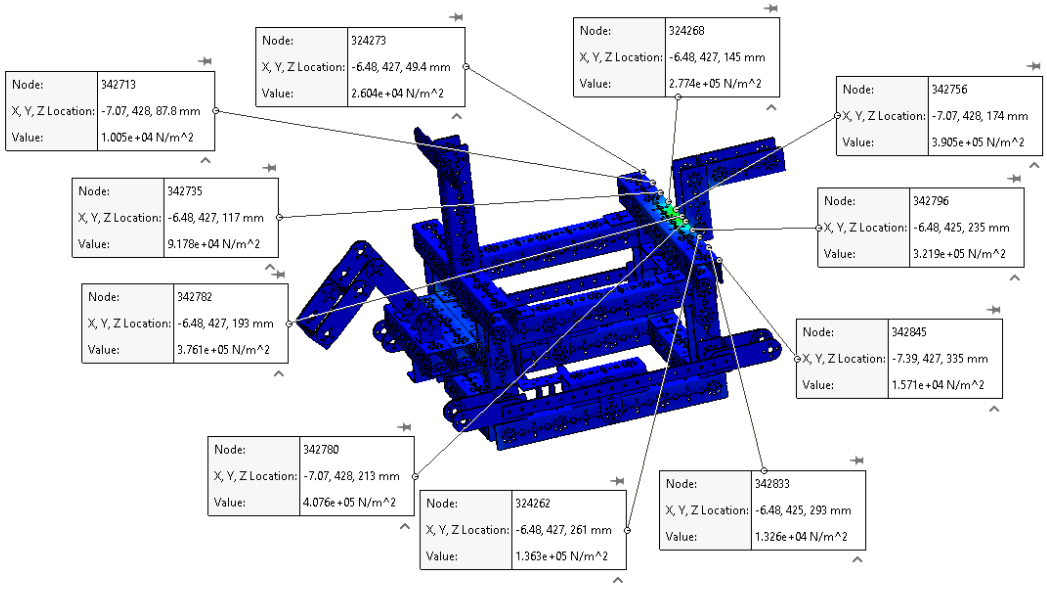

Figure 4.24: plotted point of the deforming part affected by the applied force on the pressure pump mount

The stress plots (N/m^2) at 11 characteristics points as shown in the X, Y and Z (mm) in table 5.6

Table 4.3:shows the result summary of the static nodal stress for the pressure pump mount

Description	Value	Unit
Sum	2.067e+06	N/m^2
Avg	1.879e+05	N/m^2
Max	4.076e+05	N/m^2
Min	1.005e+04	N/m^2
RMS	2.466e+05	N/m^2

4.8.5 Plotted points of the affected part of the boom arm base

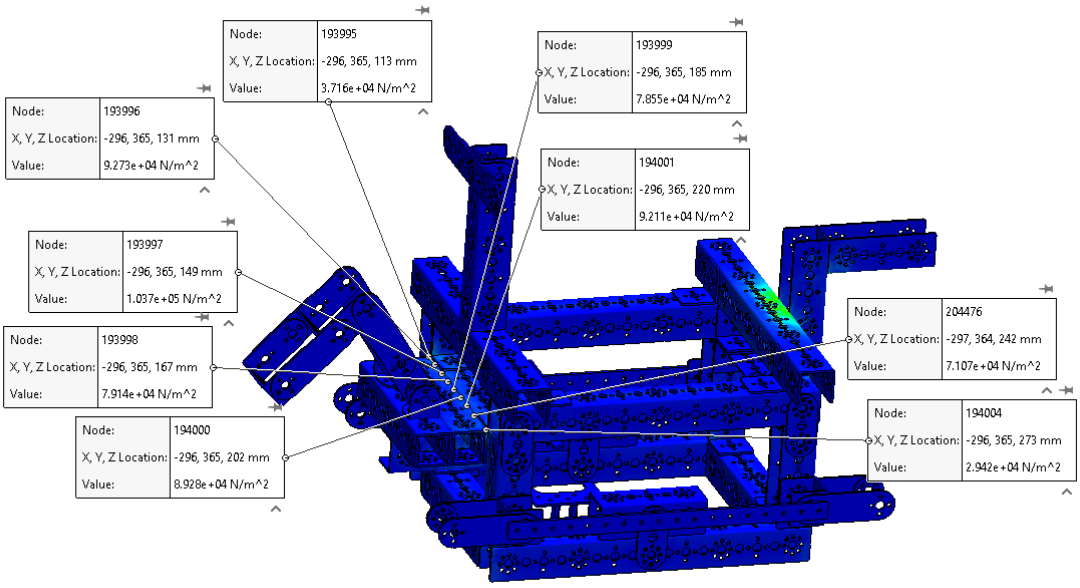

Figure 4.25: deforming part affected by the forces applied to the arm base

The stress plots (N/m^2) at 11 characteristics points as shown in the X, Y and Z (mm) in table 5.7

Table 4.4: shows the summary for the static nodal stress on the boom arm base

Description	Value	Unit
Sum	6.732e+05	N/m^2
Avg	7.480e+04	N/m^2
Max	1.037e+05	N/m^2
Min	2.942e+04	N/m^2
RMS	7.856e+04	N/m^2

Table 4.5: Final EPRSDC's Specifications

Name	Description
Crawler structural frame	5.67kg
Crawler total weight	8.173kg
Total voltage supply	12-volt
The total length of the frame	400mm x 310mm
The total length of the undercarriage track chain	440mm x 180mm
Structural frame	1050 aircraft-grade aluminium
2X SEAFLO pump	12-volt 1100 GPH
Communication type	Connect over Wi-Fi 100m
3x servo motors	6.7-volt each
motor controller	12-volt
motor controller	12-volt servo
NI-myRIO	12 to 24-volt
control relay module	12–240-volt
On and off switch	12-volt
2x DC motors	12-volt each
Dredging pipe	**Ø16** with the head of 1.4m
Total weight of 2DOF dredging arm	0.23kg
2x lighting	5-volt each
Battery 12V Nickel Metal Hydride (NiMH)	12-volt 3000mAh 10 cells
Assembled design run time	3 to 4 hours on a full charge

The above table 4.1 presents us with the overview technical report of the achieved preliminary design of the subsea crawler. This table brings us a summarized conclusion of the EPRSDC from its structural aspect which includes the drive system, frame, 2DOF arm, power consumption, communication system, camera system, dredging pumps, and power switch controlled by the LABVIEW program. In 2014 (Grandgirard et al.,) discussed extensively on tabulated approach to robotics components and their structural specifications. Robots are a set of computing systems that includes mechanical and software integration. Grandgirard et al., further outlined some important aspects that are to be tabulated when designing and programming a robot. Mechanical design, electronic component selection, software selection, data input, test data output, transfer, and feedback relationship, input data constraints, environmental constraints, knowledge data constraints, computing constraints, internal data representation, speed on connectivity, and response to the command, complexity of the response, benchmarking, robustness of design, noise, convergence, errors, reliability testing and analysis, application experience, upstream and downstream requirements, parallelizability and finally modularizability of the entire design. As indicated by the author, It is important to outline technical specifications that provide answers to our research objectives using well defined tables.

CHAPTER FIVE: DISCUSSION

This chapter briefly presents discussions on results shown in chapter four. The results are presented in data tables, graphs and corresponding correlations represented with quadratic functions.

One critical aspect of ocean driving technology is the relationship between the driving efficiency and torque at different angle of inclination. In this research, we carried out some experiments in which we recorded some data in a table. The data was used to plot graphs that helped us determine if electronic ocean dredging robots can efficiently drive under certain angular inclination. We considered experimental tests such as: maximum velocity versus different angles of inclination, torque versus velocity at 0^0angle of inclination, torque versus velocity at 20^0 angles of inclination, minimum torque versus different angle of inclination, and finally the efficiency versus torque at $0^0$and 20^0angle of inclination. Underwater robot propulsion is mainly achieved by the use of propellers, thrusters, and a tank tracking driving system which generates the moving motion of an object in the underwater environment. The efficiency of the drive system depends on the angle of inclination, and this affects the robot's maximum velocity. The drive system can be optimized using combined Genetic Algorithms (GA) and Hill-Climbing Algorithms (HCA). The GA are set of mathematical models created for optimal parameters set for input climbing functions of the ocean moving robots. It gives us expected results for real-world applications for its maximum climbing ability in an underwater environment (Tuong et al., 2009).

5.1 EPRSDC assumptions for the below discussions

1. There is no slip between tank tread chain link and the rubber placed on the ramp surface.
2. The system is ideal, i.e., there are no losses as all energy produced by the motor are converted into translational movement of the driving base.

5.2 Calculated specification of the TORQUENADO motor from vendor

N =100RPM (rotational speed)

$\omega = 22\pi N|60 = 10.47$rad/s (Angular speed)

Maximum torque = 4.94N/m (700 ozin)

For two motors used in the driving based

= 4.94 X 2

=9.88Nm

Power input = torque X ω

=9.88 X 10.47

Maximum power produced by two

= 103.44 watts

Efficiency = $\frac{\text{power output}}{\text{power input}}$

Power output = weight x Velocity

Weight = 81.73N

Table 5.1: maximum velocity versus different angles of inclination

Distance covered in meters	Time taken in (seconds)	Average time (seconds)	Maximum velocity (m/s)	Angle of inclination (In degrees)
1.8	6.05 6.17 5.76	5.9	0.305	0^0
1.8	7.09 6.96 6.98	7.01	0.256	15^0
1.8	7.1 7.3 7.3	7.2	0.250	20^0
1.8	7.93 7.71 9.91	8.5	0.211	25^0
1.8	9.29 10.2 10.3	9.93	0.181	30^0

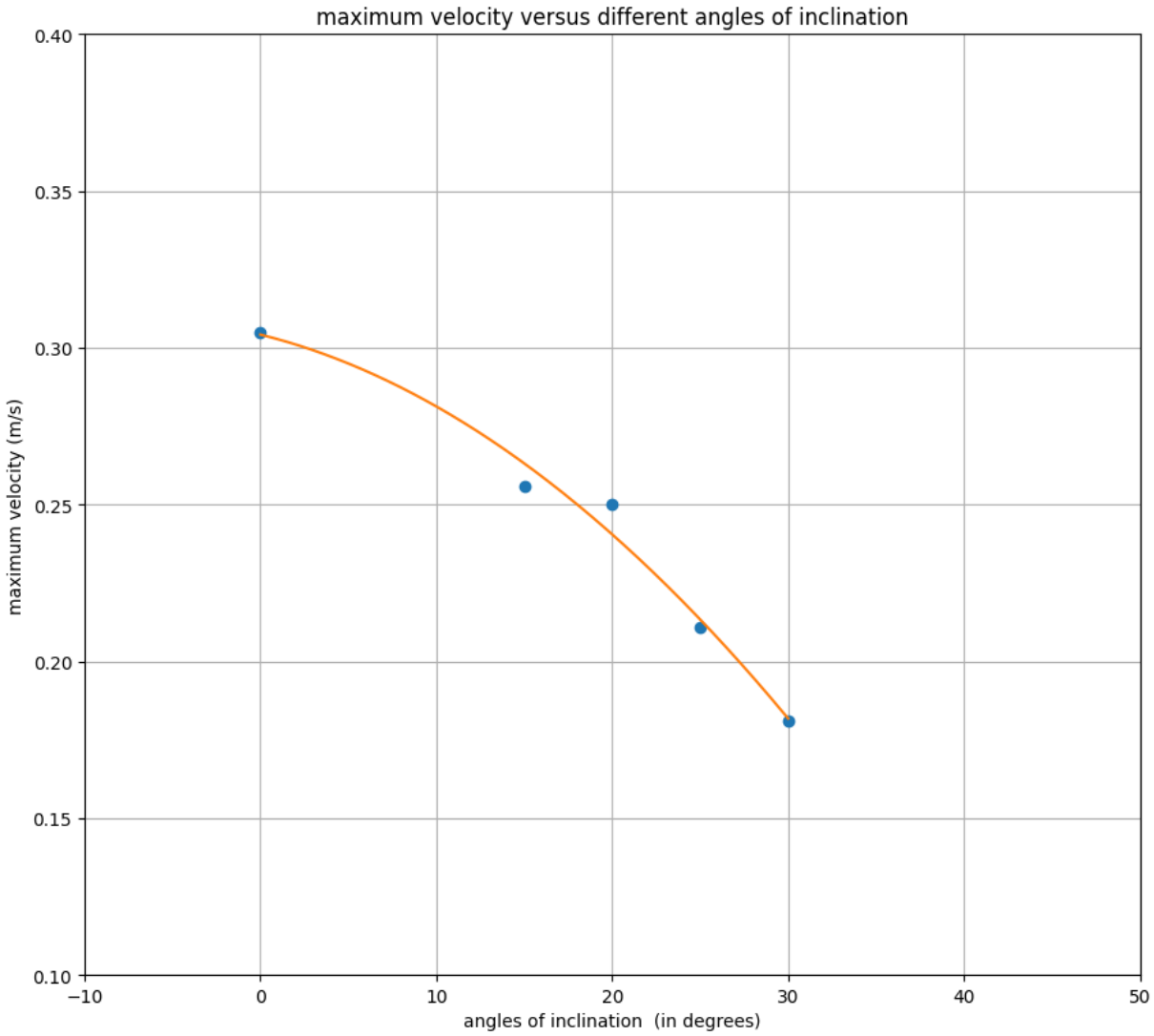

Figure 5.1: graph of maximum velocity versus different angle of inclination

We conducted an experiment to determine the maximum velocity versus the robotic crawler's different angle of inclination. This graph can be represented as a quadratic function and the equation for this function is:

$$-8.94714809e-05x^2-1.39638932e-03x+3.04207745e-01=0$$

This shows that the maximum velocity of the crawler reduces as the angle of inclination increases. These happen in an approximately quadratic fashion. As seen in table 4.6, at an angle of 30^0 the maximum velocity was 0. 181 (low) and at an angle of inclination 0^0 the maximum velocity was 0.305 (high).

Furthermore, python was used to generate a modelling graph that illustrated solutional results for our experimental formulas for solving quadratic equation.

Constant velocity is important in understanding the planning and slamming of sequential tank driving systems for marine vehicles or vessels. Ocean propelling vehicles are developed to drive wedge sections with end plate down sectional guides which are used for measuring continues velocity. The entry force and velocity are measured using analytical data that are identified as the wetting factor at the low deadrise (maximum angle). Tveitnes et al., (2008) performed some analytical experiments to determine and understand the relationship between planning and slamming of marine vessels. The author stated that during his observation, a wetting factor of about 1.6 at low deadrise angles are reduced nearly linearly at 1.3 to the angle of 45^0 deadrise. An additional mass was added which led to an increase quadratically with immersed depth until the chines became visibly wetted to show the angular increase.

Table 5.2: Torque versus velocity at 0^0 angle of inclination

Distance covered in meters	Time taken in (seconds)	Average time (seconds)	Torque	Maximum velocity (m/s)	Angle of inclination (In degrees)
1.8	0 0 0	0	20%	0	0^0
1.8	25.95 25.33 26.08	25.7	40%	0.07	0^0
1.8	12.19 12.03 11.97	12	60%	0.15	0^0
1.8	8.00 8.02 7.92	7.9	80%	0.227	0^0
1.8	6.05 6.02 6.07	6	100%	0.300	0^0

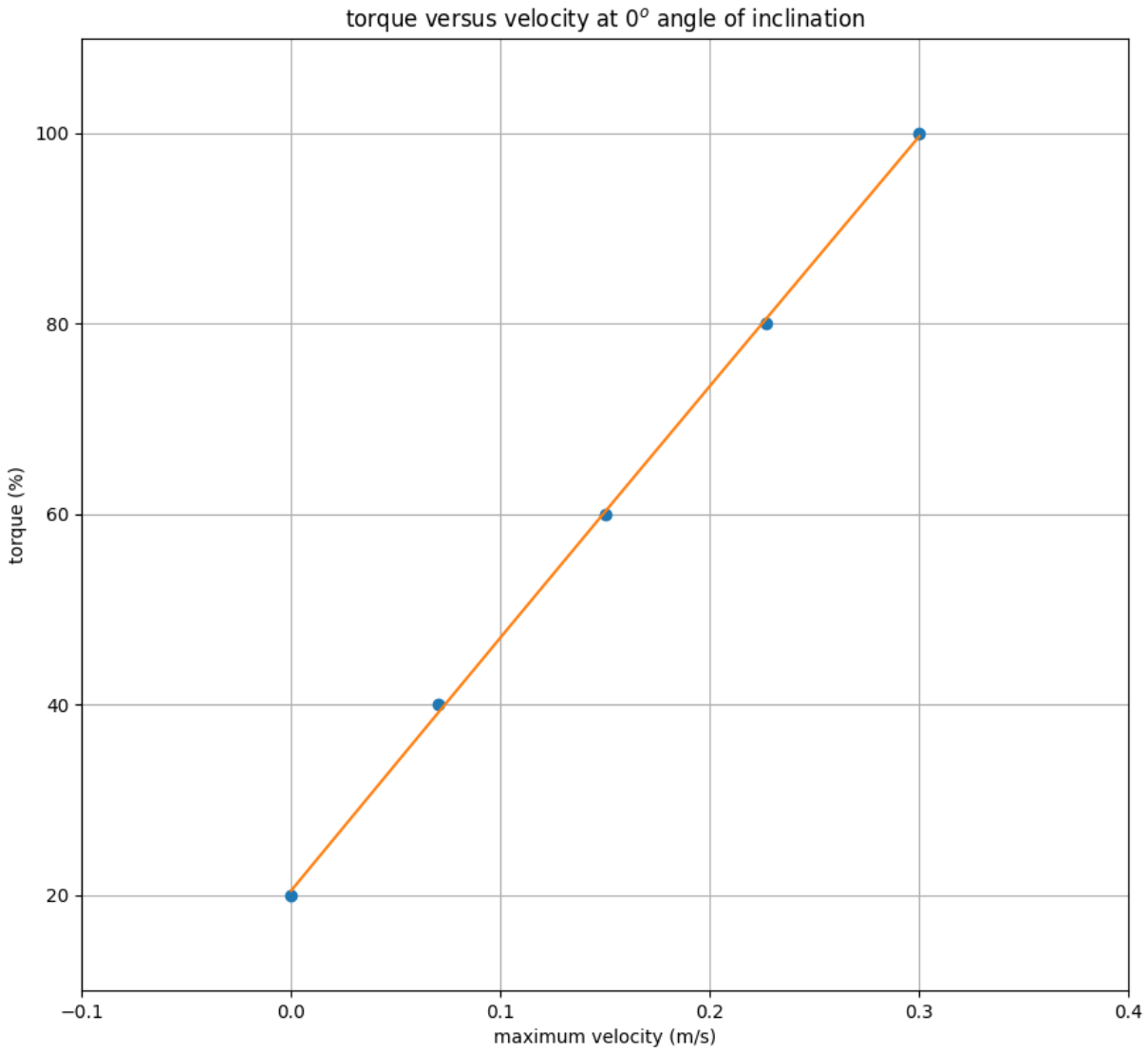

Figure 5.2: torque versus velocity at 0^0 angle of inclination

The torque versus velocity at 0^0 angle of inclination is presented in the graph above. The maximum torque is attained when both motors are fully powered (100%). Furthermore, the velocity obtained is 0.300 m/s. At the minimum velocity 0, 20% of the power was used. This above description simply means that for the subsea crawler to move its weight (8.73N) forward, the power utilized from the motor must be above 20%. The speed of the crawler can vary from 0 to 0.300m/s

The graph can be represented by the quadratic equation shown below:

$$-8.93975716\ x^2 + 266.77666129x + 20.44560365 = 0$$

Table 5.3: Torque versus velocity at 20^0 angle of inclination

Distance covered in meters	Time taken in (seconds)	Average time (seconds)	Torque	Maximum velocity (m/s)	Angle of inclination (In degrees)
1.8	0 0 0	0	20%	0	20^0
1.8	40.36 41.86 42.39	41.5	40%	0.043	20^0
1.8	15.76 15.54 15.65	15.7	60%	0.114	20^0
1.8	10.06 9.86 10.02	9.9	80%	0.181	20^0
1.8	7.35 7.29 7.46	7	100%	0.257	20^0

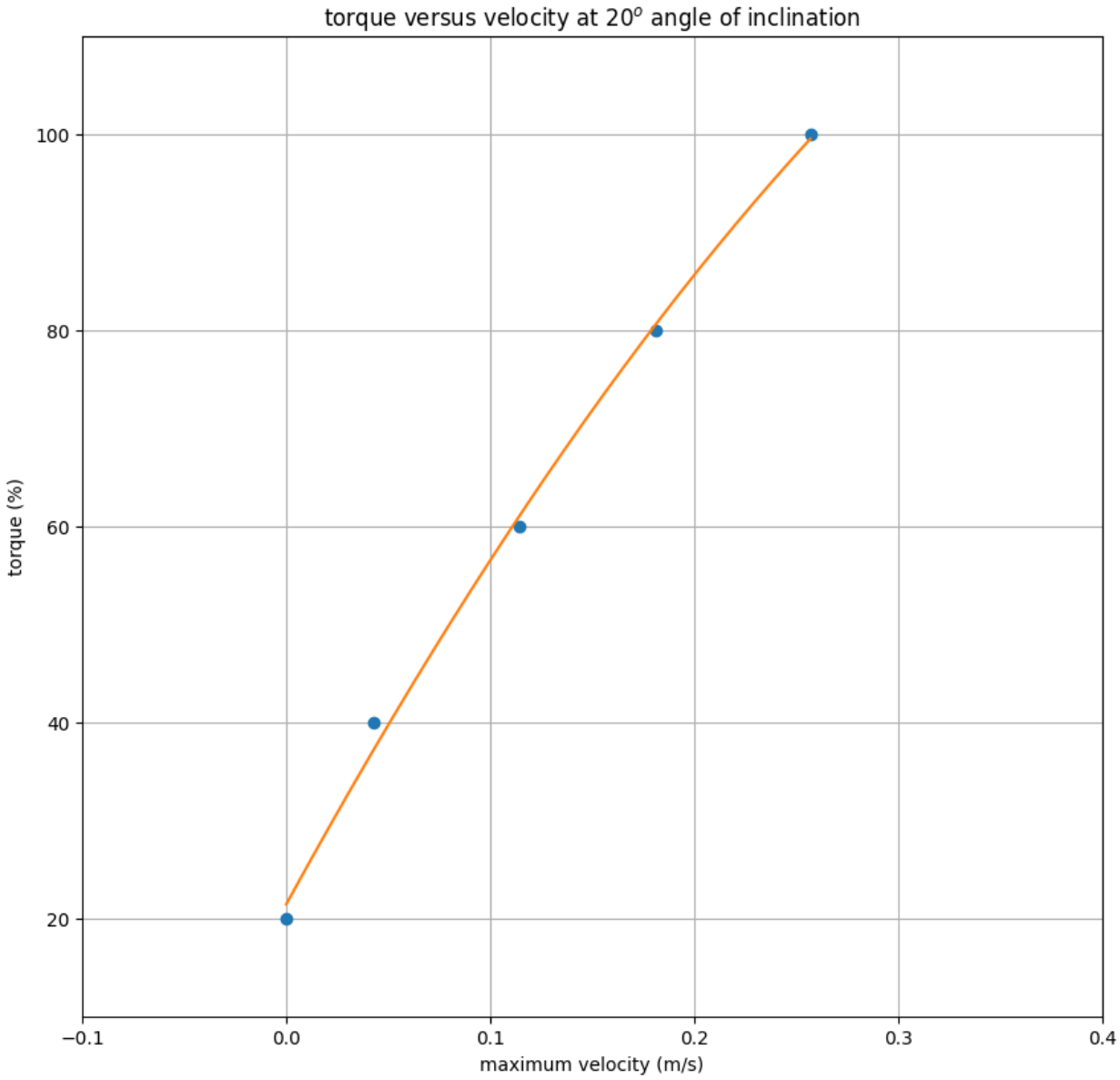

Figure 5.3: torque versus velocity at 20^0 angle of inclination

The above graph as shown in figure 5.3 presents us with the relationship between the torque and maximum velocity at 20^0 angle of inclination. We can see as shown in the graph that the maximum velocity of the crawler is 0.257m/s at 100% of its full power (torque). The minimum velocity was 0m/s at 20% torque. For the crawler to overcome its weight 8.73N, we need more than 20% of the maximum capacity of the motor to make the crawler move from its initial place.

The relationship between the torque and maximum velocity at 20^0 of inclination can be represented with the quadratic equation below:

$$\mathbf{-299.07208471\,x^2 + 380.67631735x + 21.49772579 = 0}$$

Table 5.4: minimum Torque versus different angle of inclination

Distance covered in meters	Minimum Torque at full power	Average Minimum Torque	Angle of inclination (In degrees)
1.8	29% 31% 30%	30.0%	0^0
1.8	32% 33% 33%	32.6%	15^0
1.8	34% 34% 35%	34.3%	20^0
1.8	35% 36% 36%	35.6%	25^0
1.8	37% 38% 37%	37.3%	30^0

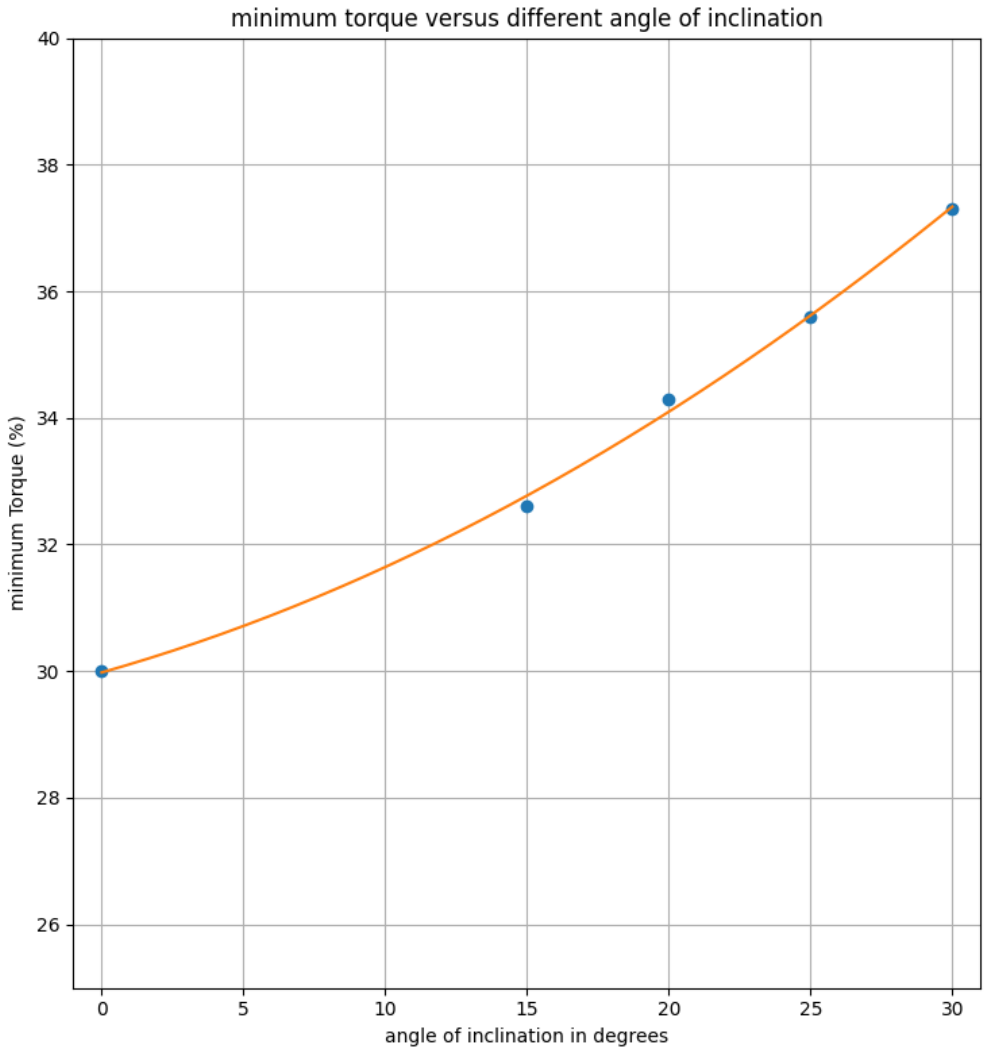

Figure 5.4: minimum torque in percentage versus different angle of inclination

The graph shown in figure 5.4 presents the minimum torque in percentage of the crawler versus different angles of inclination. As seen in the graph, the minimum torques required to move the crawler from its initial position at 0^0 angle of inclination was 30% in this experiment. The minimum torque required to move the crawler from its place of rest at an angle of 30^0 inclination is 37.3%. in this illustration, the minimum torque required to move the crawler under different angles of inclination varies from 30% of the total torque to about 37.3% of its total torque. this shows that at least 30% of the torque is required to move the weight of the crawler at different angles.

The quadratic equations showing the relationship between the minimum torque and the angle of inclination in degrees can be represented with the formula below:

$$\mathbf{3.93720565e-03}\ x^2 + \mathbf{1.27095761e-01}x + \mathbf{2.99792779e+01} = \mathbf{0}$$

Table 5.5: graph of efficiency versus torque at 0^0 and 20^0 angle of inclination

5.2.1 Efficiency versus torque at 0^0

Torque (%)	Average velocity	Useful power output (watts)	Power input	Efficiency (%)
20%	0	0	20.688	0
40%	0.07	5.721	41.376	0.138
60%	0.15	12.255	62.064	0.197
80%	0.227	18.54	82.752	0.224
100%	0.300	24.51	103.44	0.237

5.2.2 Efficiency versus torque at 20^0

Torque (%)	Average velocity	Useful power output (watts)	Power input	Efficiency (%)
20%	0	0	20.688	0
40%	0.043	3.514	41.376	0.085
60%	0.114	9.317	62.064	0.150
80%	0.181	14.793	82.752	0.179
100%	0.257	21.00	103.44	0.203

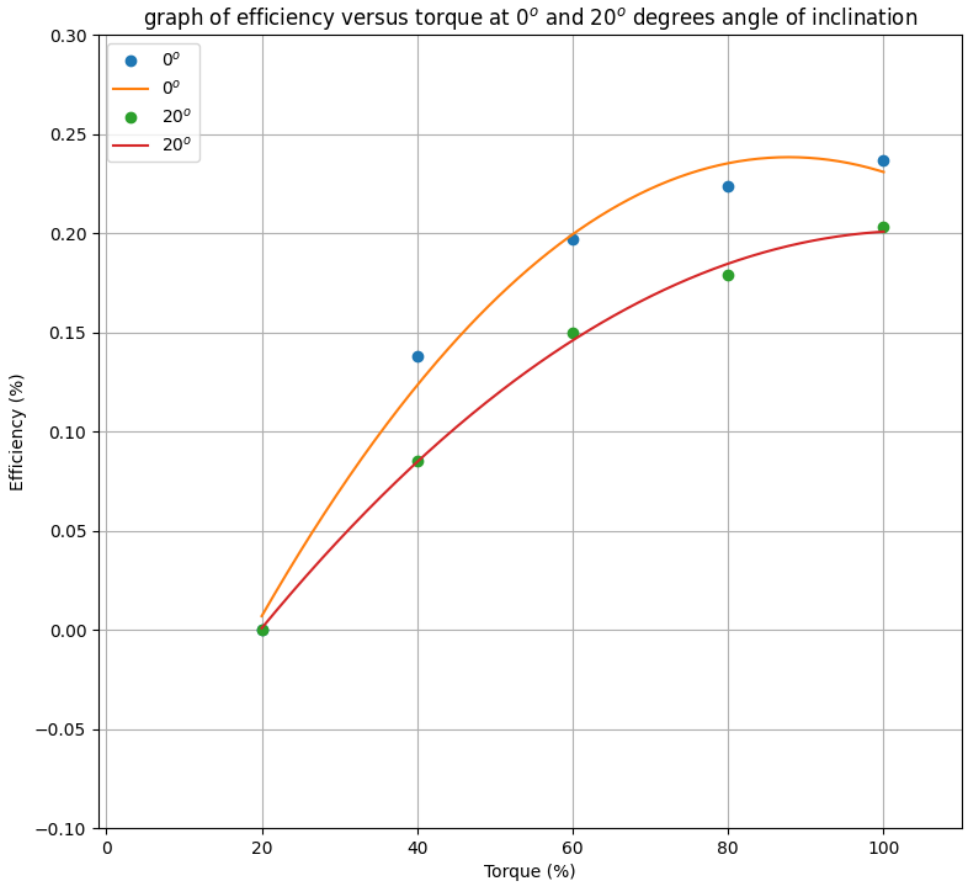

Figure 5.5: graph of efficiency versus torque at 0^0 and 20^0 degrees angle of inclination

As presented in figure 5.5, the graph shows us the relationship between efficiency and the torque at $0^0$and 20^0 angle of inclination. We can see from the graph that the efficiencies were relatively low at 20% and higher at 100%. The crawler had better efficiency at 0^0 compared to the efficiency at 20^0. Driving the crawler at an angle of inclination 20^0 creates more energy losses than at an angle of 0^0. As seen in the graph at 0^0 at 80% torque, the efficiency stopped increasing and the curve started declining. This implies that from 80% up to 100% torque, the efficiency does not increase. Furthermore, at that range, increasing the power input (torque) does not guaranty more the efficiency. The efficiency can only increase from 20^0 to 80^0 angle of inclination after which it starts to decline.

The quadratic equation below shows the relationship between the efficiency and torque at 0^0 and 20^0

a) **First formula**

$$\mathbf{5.03571429e-05}\ x^2 - \mathbf{8.84285714e-03}x - \mathbf{1.49800000e-01} = 0$$

b) **Second formula**

$$\mathbf{-2.82142857e-05}x^2 + \mathbf{5.88571429e-03}x + \mathbf{-1.05600000e-01} = 0$$

Table 5.6: shows the static nodal stress for the pressure pump mount

Node	Value (N/m^2)	X (mm)	Y (mm)	Z (mm)	Components
324273	2.604e+04	-6.48292446	426.77896118	49.41464996	39068_txm-288 mm channel (3)-1
342713	1.005e+04	-7.06871080	428.19320679	87.81465912	39068_txm-288 mm channel (3)-1
342735	9.178e+04	-6.48292446	426.77896118	116.61465454	39068_txm-288 mm channel (3)-1
324268	2.774e+05	-6.48292446	426.77896118	145.41465759	39068_txm-288 mm channel (3)-1
342756	3.905e+05	-7.06871080	428.19320679	174.21464539	39068_txm-288 mm channel (3)-1
342782	3.761e+05	-6.48292446	426.77896118	193.41465759	39068_txm-288 mm channel (3)-1
342780	4.076e+05	-7.06871080	428.19320679	212.61465454	39068_txm-288 mm channel (3)-1
342796	3.219e+05	-6.48292446	425.43426514	235.06993103	39068_txm-288 mm channel (3)-1
324262	1.363e+05	-6.48292446	426.77896118	260.61465454	39068_txm-288 mm channel (3)-1
342833	1.326e+04	-6.48292446	425.43426514	292.55935669	39068_txm-288 mm channel (3)-1
342845	1.571e+04	-7.39072990	427.17266846	335.41384888	39068_txm-288 mm channel (3)-1

5.3 FEA Graph for 1050 aircraft grade aluminium static loading simulation for pressure pump base mount

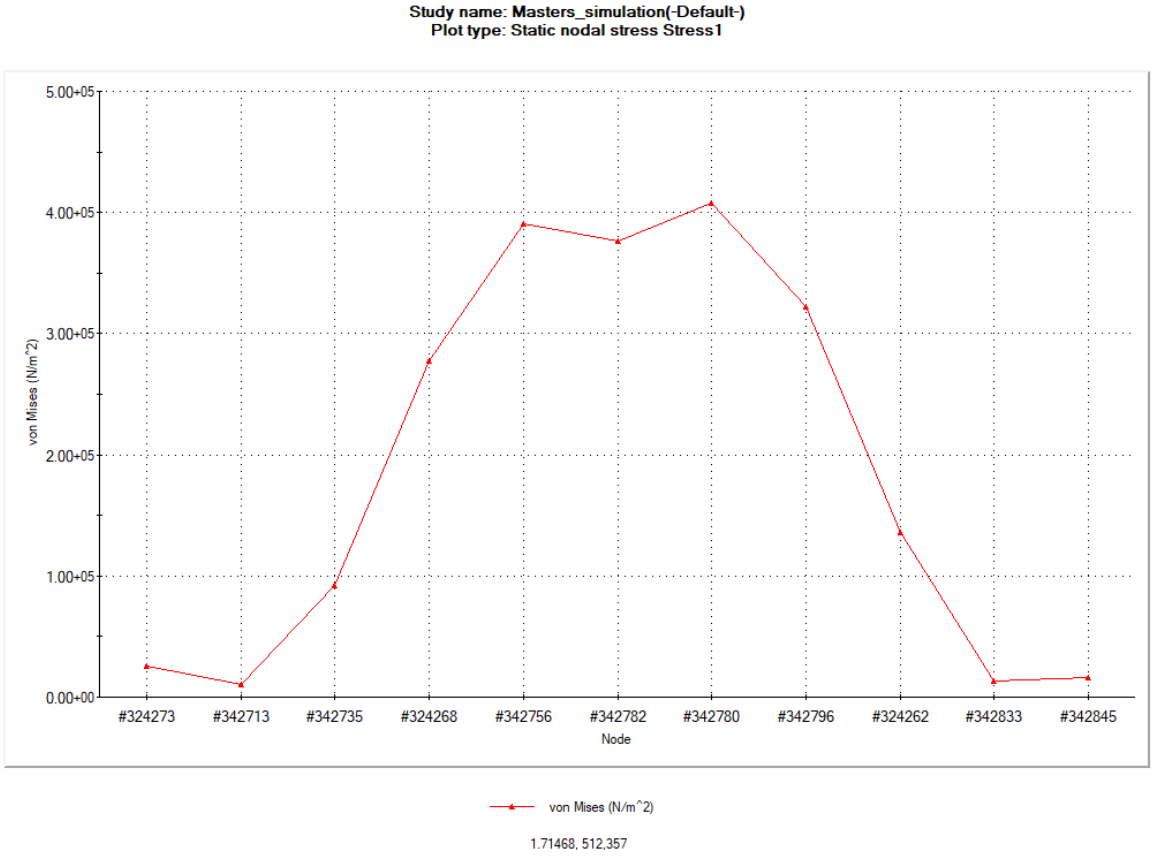

Figure 5.6: Von Mises stress distribution at selected nodes on the pressure pump base mount

The above graph figure 5.6 presents us with the von mises stress at some selected nodes. The graph further gives us an idea of the stress distribution along the 288mm channel during the simulated process, under static loading conditions for the structural frame chassis. After a load of 0.73N was applied to 39068_txm-

288mm channel (3)-1, the von mises stress increased at node #342713 to 2.6 x 10^4 N/m^2 which later dropped to its lowest minimum 1.0 x 10^4 N/m^2 at node #324273. The stress further surged up to 9.1 x 10^4 N/m^2 which progressively increased to 2.77 x 10^5 N/m^2. The stress point got to its first maximum stress 3.9 x 10^5 N/m^2 and then dropped to 3.7 x 10^5N/m^2 at node #342782. The stress further pushed to its highest maximum stress 4.0 x 10^5N/m^2 at node #342780. The maximum stress started to drop to its minimum at 3.2 x 10^5 N/m^2 until it got to its final minimum at 1.5 x 10^5 N/m^2. As seen on the graph the 288-channel base mount which the pump is fixed on has two critical points of maximum stress. These points are at the middle of the 228mm channel which is shown on the graph as the maximum stress points 3.9 x 10^5 N/m^2 and 4.0 x 10^5 N/m^2.

Table 5.7: shows the result static nodal stress for the static nodal stress on the boom arm base

Node	Value (N/m^2)	X (mm)	Y (mm)	Z (mm)	Components
193995	3.716e+04	-296.48291016	364.77899170	113.41464996	39067_txm-160 mm channel (2)-1
193996	9.273e+04	-296.48291016	364.77899170	131.19242859	39067_txm-160 mm channel (2)-1
193997	1.037e+05	-296.48291016	364.77899170	148.97019958	39067_txm-160 mm channel (2)-1
193998	7.914e+04	-296.48291016	364.77899170	166.74798584	39067_txm-160 mm channel (2)-1
193999	7.855e+04	-296.48291016	364.77899170	184.52575684	39067_txm-160 mm channel (2)-1
194000	8.928e+04	-296.48291016	364.77899170	202.30354309	39067_txm-160 mm channel (2)-1
194001	9.211e+04	-296.48291016	364.77899170	220.08131409	39067_txm-160 mm channel (2)-1
204476	7.107e+04	-297.05371094	364.48873901	242.00335693	39067_txm-160 mm channel (2)-1
194004	2.942e+04	-296.48291016	364.77899170	273.41464233	39067_txm-160 mm channel (2)-1

5.4 FEA Graph for 1050 aircraft grade aluminium static loading simulation for the boom arm base

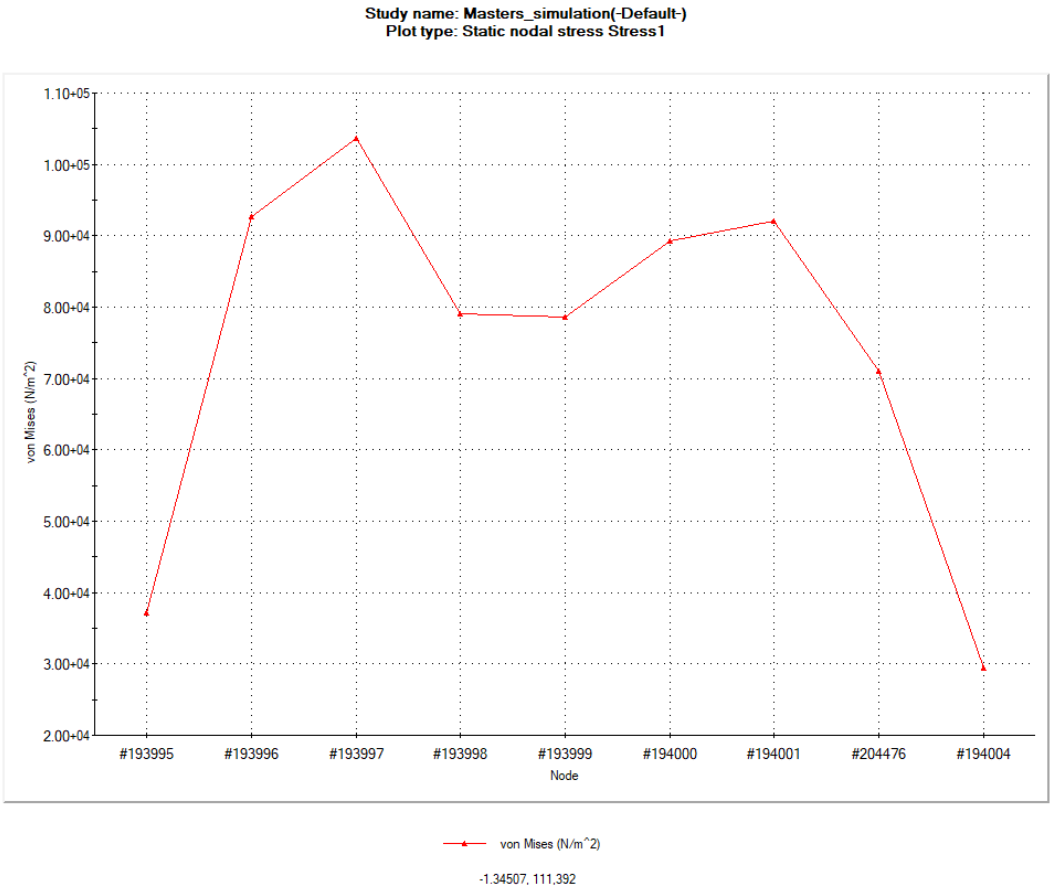

Figure 5.7: Von Mises stress distribution at selected nodes on the boom arm base

As presented in figure 5.7 nine points were selected on the boom arm base. The base arm is responsible for carrying the weight of the entire arm. The base and arm weight were measured as 2.808N. The von mises stress distribution across the cross-sectional area was plotted for the base 160 mm channel beam. The software plotted some points which started at its minimum 3.7 x 10^4 N/m^2 at node #193995. The stress increased rapidly to 9.2 x 10^4 N/m^2 and finally approached its maximum stress of 1.0 x 10^4 N/m^2. We had a slight drop in the stress on the beam from 7.9 x 10^4 N/m^2 to 7.8 x 10^4 N/m^2. From 8.9 x 10^4 N/m^2 to 9.2 x 10^4 N/m^2 we experienced a surge which led to our second maximum stress and then it dropped to 7.1 x 10^4 N/m^2 and finally 2.9 x 10^4 N/m^2. In conclusion, it can be seen that the stress acting on the material has two maximum points which are 1.0 x 10^4 N/m^2 and 9.2 x 10^4 N/m^2. The result did not show significant deformation during our experiment. More improvements were made and recorded on our recommendations section (chapter seven).

CHAPTER SIX: CONCLUSION

This chapter briefly presents the research conclusions, applications and future prospects for the EPRSDC.

This research successfully demonstrated the feasibility of an electric powered robotic subsea dredging crawler for ocean applications. The system developed is projected to be a key factor in the advancement of ocean operations such as mining, ocean oil and gas pipeline laying and exploration technology. Considering the exponential growth of computer vision, machine learning and computing technology, the subsea dredging crawler can become simpler and easier to implement for exploration. These technological developments can also help reduce ocean pollution and high energy consumption for ocean dredging application making the process safe and reliable. As a result, it will find applications in the following areas:

6.1 Ocean mining and extraction of natural resources

Scott, (2011) stated that ocean covers about 71% of the earth's surface, these areas are almost twice the area of the surface of the moon and mars combined. Scott further indicated that the Pacific Ocean covers a larger area on the earth's surface than all the continents. His research indicated that marine mining is currently gaining more traction though it has been in existence since the 20th century. This paper disclosed some challenges faced by the ocean mining industry which are inadequate subsea driving and extraction technology. (Cuyvers et al., 2018) also pointed out some problems faced by ocean excavation such as hydraulic pollution and heavy machine operation which disturbs aquatic habitats in the sea floor. It further elaborated on some technological considerations when developing ocean technology. Modern deep-sea technology are being developed for operation such as cable-laying, offshore diamond mining, dredging, and offshore oil, and gas extraction. The aim of the paper was to identify recent technology that could reduce ocean disturbance such as pollution caused by hydraulic leakages.

The author further discussed some recent hydraulic powered ocean mining technology. Mining was successfully performed at a depth of 1600m which was tested in waters of Kinawa. The system was designed by Japan oil, and metal national corporation in adjoined to the Japanese ministry of economy. This research identified certain operations performed using ocean dredging crawlers and considered what depth these dredgers operate using their respective excavation tools such as Auxiliary cutter (AC), Bulk cutter (BC) and collection machine (CM).

As discussed in our problem statement, hydraulic crawlers such as the MK 3 ROST have been used for so many years for ocean excavation of diamonds. These machines are propelled by hydraulic fluid which can cause ocean pollution. It also consumes high energy due to their heavy duty parts and method of operation. Fluids, (2017) identified that mineral oils are the main components of hydraulic oil which belongs to a larger class of chemicals called the distillates. In this paper it was indicated that the Environmental Protection Agency (EPA) United States identified one of the most hazardous waste sites which make up the National Priorities List (NPL) requiring long term ocean and inland cleanup. They indicated that among the most hazardous chemicals found on earth, hydraulic fluid was ranked number 10 out of 1,428 on the list. The authors further disclosed that when exposure to hydraulic fluid can harm both aquatic life and humans. It can cause pneumonia and bleeding in the intestines which can lead to death. Some tests were conducted on an animal that was exposed to hydraulic fluid. The effect as observed by the health agency included skin and eyes turned red and swollen, very heavy breathing, drowsiness, and congestion of lungs, and possibly cancer indicated in blood stream of animal. The development of the electric powered robotic subsea dredging crawler eliminates the health risks associated with hydraulic crawlers in the mining industry. They also contribute to the reduction of hydraulic fluid pollution in the ocean environment. The hydraulic control system powering the drive system and boom arm are replaced with electronic actuators such as electric motors and servo motor. The EPRSDC will have a much lighter weight compared to its hydraulic counterpart. For our scaled down model, the EPRSDC was powered with a 12V Nickel Metal Hydride (NiMH) 3000mAh 10 cells battery which has an endurance of 3 to 4 hours on full charge. Our design is cost effective with regards to manufacturing and maintenance.

6.2 Conclusion based on the outlined objectives

6.2.1 3D structural design of the crawler

After designing and modelling the EPRSDC parts using SOLIDWORKS student version, we assembled the parts into our full structural model. This process assisted us in understanding the respective position and orientation of all mechanical and electronic components in our system. Using this software, we were able to explore different design ideas before manufacturing and implementation on hardware. Researchers such as Sam et al., (2012) have successfully demonstrated some structural designs of robotic arms using SOLIDWORKS. Sam et al., disclosed that this software was used to design a cartesian robot and an articulated industrial robotic arm with different grippers. The result of this project indicated that the simulation Xpress study and motion study were used to model the articulated robot arm parts and move it to demonstrate pick and place robotic system. This software enabled easy simulation and error detection in

designed parts. This research identified certain key point such as analysis and detection of some engineering design errors before hardware manufacture of our scaled down models.

6.3 Hardware manufacturing of the EPRSDC

6.3.1 Manufacturing of the structural frame

the chassis components were manufactured from 1050 aircraft grade aluminum and assembled using the design measurements. Three fundamental parts of the vehicle were assembled which include: undercarriage structure, dynamic driving base and the boom arm. After successfully assembling the structural components, the electronic components were assembled on the structural assembly. Nazaruddin & Gunawan, (2015) mentioned in our literature review section, described crawler undercarriage systems with their electronic layout. These systems were said to be critical to oceans excavators. These parts consist of several components which supports the movement of the excavator. The drive system consists of sprockets, final drive unit, track shoe, track link, track frame, track roller and front idler. This research helped us identify the important mechanical parts for the structural design for our ocean crawler. Furthermore, their research allowed us to better understand experiments around driving on inclined planes.

6.3.2 Electronic communication system

the electronic system such as: NI myRIO, motor controller, servo motor controller, 12-volt seaflo pump, 12 to 240-volt relay module, Logitech camera, servo motor, lighting and 12-volt motor were all carefully placed on the assembled crawler considering the 3D model. As discussed in our methodology, before assembly, the specifications of all electronic parts were analyzed. The purpose and function of each component were also stated accordingly.

Nazaruddin & Gunawan, (2015) discussed the use of electronic system in driving excavators. The authors further stated that electric motors are the major devices used in driving systems such as electric cars, industrial fan, compressors, and dredging pumps. In the design of their excavator, bevel gears were used for transmitting motion between intersecting shafts. Rafiq et al., (2018) stated that NI myRIO hardware platform can be used in designing the operational software, physical system design of mechanical and electronic applications software, and implementation of controller for real-world application. This paper helped us in identifying the right controller for controlling the crawler over 100m using Wi-Fi.

6.3.3 Designed software algorithm using a Graphical User Interface (GUI) to control the EPRSDC

we were able to control our crawler through a GUI over 100m using wireless IP address connectivity. On this control platform, a live stream of the camera was displayed which allowed us to see the environment

of the crawler. The GUI was used to control the drive units, boom arm, headlights, and pumps. All these were achieved on a touch screen laptop computer. Using LabVIEW software was efficient because of its graphical programming interface which uses blocks called the Virtual Instruments (VIs) thereby making the programming process easier and quicker.

The VI for controlling the crawler can be viewed from:

a. The front panel: which includes knobs, push buttons, graphs and other inputs and outputs. This made the GUI user-friendly.
b. The block diagram: included the blocks or VIs for each control. We further connected wires between the blocks to indicate the dataflow. The system front panel object has corresponding terminals on the block design diagram to allow the user to interact with the VIs.
c. The sub-VIs: which were used to create a modular system where blocks of VIs were saved into one sub-VI

6.3.4 The test ramp for experimenting with the crawler's climbing inclination

The test ramp was used to create different angular inclinations to determine the climbing characteristics of the crawler. Each test was performed three consecutive times and the driving length distance covered was 1.8 meters. The ramp was designed to be adjusted during the experiment. This adjustment was within the range of inclination angles: 0^0, 15^0, 20^0, 25^0, 30^0. This experiment helped us in understanding the performance of the drive system under uneven terrains or sloppy environments.

6.3.5 Demonstration of the crawler's climbing characteristics for five different angles

The angular inclination experiments reported in chapter four and five show the feasibility of the scaled down concept for the EPRSDC. The experimental data provided useful information for the future development of our EPRSDC.

We recorded and tabulated the experiments and further used graphs to illustrate the performances recorded by the driving system. The following are the practical experiments below:

6.3.5.1 Maximum velocity versus different angles of inclination

This experiment showed the change in maximum velocity of the crawler as the angle of inclination increases. This furthered showed that increasing the angle of inclination reduces the maximum velocity of the crawler. The crawler performance can be improved by installing more powerful motors that will overcome higher angles of inclination.

6.3.5.2 Torque versus velocity at 0^0 angle of inclination

This experiment shows the minimum power (20% of maximum power) required by the crawler to enable it to just start to move. The weight of the crawler (8.73N) could not be moved with any power less than 20% of maximum power on an angle of 0^0.

6.3.5.3 Torque versus velocity at 20^0 angle of inclination

This experiment showed that for the crawler to overcome its weight (8.73N), we needed at least than 34.3% of maximum power.

6.3.5.4 Drive minimum Torque versus different angles of inclination

This experiment showed that the minimum torque required to move the crawler at an 30^0 inclination is 37.3%.

6.3.5.5 Efficiency versus torque at 0^0 and Efficiency versus torque at 20^0

The results show that the drive efficiency at 0^0 angle of inclination was higher than the drive efficiency at 20^0 angle of inclination.

6.4 FEA results for static loading test

The static loading analysis using FEA was successfully conducted to determine the maximum deformation and von-Mises stresses on the structural frame of the crawler. The final result of the simulation shows the vulnerable areas with regards to maximum stresses and displacements. Based on this result, it is recommended that future versions of the crawler will be reinforced at the vulnerable areas. we obtain two graphs from the simulation, one for the pump mount base and the second for the arm base mount. Our selected material 1050 aircraft grade aluminum performed decently, hence it will help us make better material selection for future developments.

CHAPTER SEVEN: RECOMMENDATIONS FOR FUTURE DEVELOPMENT

This chapter briefly presents recommendations for the EPRSDC design, waterproofing, driving system, CFD simulations and FEA simulations.

Our EPRSDC design provided us with useful data and validation for our design process available in chapter three, four, and five. It also presents some possible solutions to the elimination of hydraulic pollution and high energy consumption in ocean mining operations. Some experimental data was obtained for the drive performance and structural frame. The experiments on different angles of inclination helped us to reliably characterize driving parameters of the EPRSDC. We noticed our tank tread chain link was slipping over the sprocket, during the operation of our model, we therefore recommend an adjustable system for tensioning our chain link system to avoid slippage. We also recommend that a guarding rail should be designed around the tracks to always keep it in position. Underwater test should be carried out on future models to understand the impact of hydrostatic and hydrodynamic forces on the model. The underwater tests can be conducted at a depth of 1.8m for the future prototype.

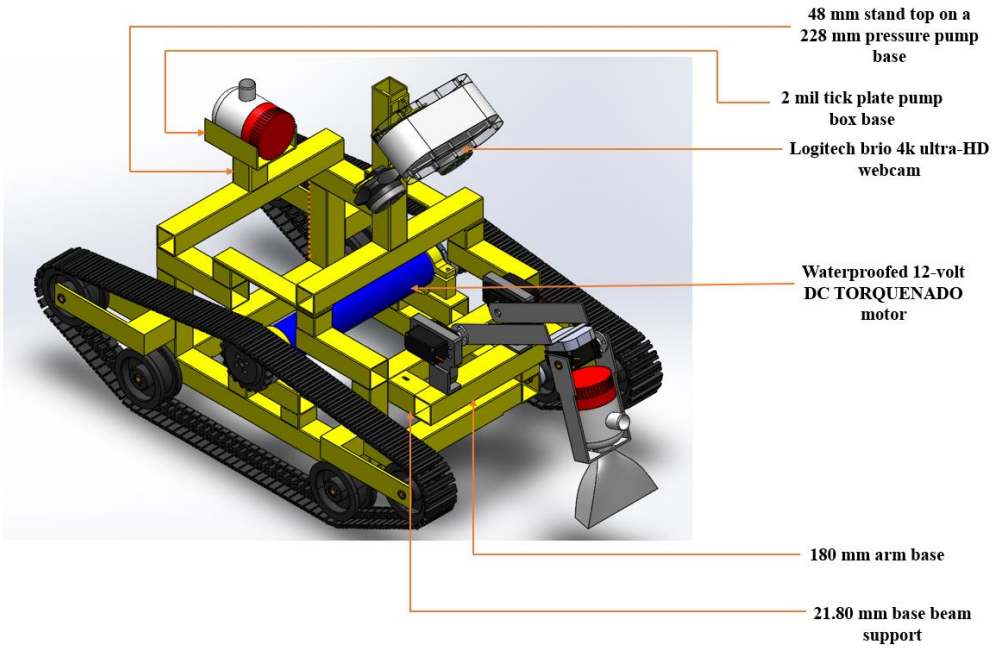

Figure 7.1: Improved concept design made after the results in chapter three, four and five

As seen in the above figure, we have concluded the final conceptual design which we recommend for future developments of the EPRSDC to be tested underwater at a depth of 1.8m. This will enable us to determine the possible outcomes and characteristics for the scaled-up design for industrial use. We further recommend that the below four concepts should be put to consideration.

7.1 Design recommendation for material selection

The model frame as presented in chapter four was made of aircraft grade aluminum with the series rating of 1050. In the beginning of our research, we considered and selected every component carefully, making sure that no component will cause ocean pollution. We recommend using mild steel 25mm x 25mm tube pipes for the structural chassis design in future versions. This mild steel is a type of steel with a low amount of carbon and wall thickness of 2mm. It also has very low amount of vast chromium, molybdenum, and other alloying element in mild steel. It can withstand hydrodynamic effects and hydrostatic effects expected in real-world applications. As seen in our recommended concept design, we made some improvement in the arm frame and the pressure pump mount base. We recommend further structural improvement if need be.

7.2 Recommendation for waterproofing for the electronic systems

As discussed in our methodology figure 3.21 the 12-volt DC TORQUENADO motor was waterproofed using high density plastics and PVC pipes. We recommend that the electronic drive system performance should be tested after waterproofing to detect if the waterproofing affected the performance of the motors. Due to the waterproofing of the electronic components several changes were made on the design which affected the motor mount, track tensioner and camera position. We recommend while making these changes careful consideration should be taken to ensure that the center of mass for the robot is at a central position making the robot balanced during movement. The camera (Logitech brio 4k ultra-HD webcam) can be improved with some image processing techniques to stabilize the images. We recommend that control software can be improved to get more functionalities such as image tracking, ultra-zoom and object detection. The high-density waterproofing system used on the cameras can be tested before deployment to determine if the thickness of the plastic significantly affects the clarity of the images from the camera.

7.3 Recommendation on driving system in different environments

After the successful development and result obtained in the preliminary test, we recommend that the waterproofed EPRSDC tank tread driving system should be tested under the following condition:

a. On the ramp submerged in a water pool under a depth of 1.8m,
b. On uneven terrains with wet grass, pebbles, stones,
c. On different smooth surfaces such as wood, and glass.

This will help in characterising the driving performance for the scaled-up crawler at sea. We also recommend considering that an increase torque will automatically enhance our climbing capabilities on higher slopes especially in uneven environment.

7.4 Recommendation for CFD and FEA analysis

We recommend using ANSYS software to simulate the system under hydrostatic and hydrodynamic forces. Due to the non-negligible forces acting on vehicle by the surrounding water when submerged, the analysis of the underwater based pressure is imperative. C.F.D simulations for the vehicle is recommended for the straight line and steering motions. Yu et al., (2020) analyzed a blade stress using ANSYS to determine the effect of hydrodynamics. This research was conducted to determine the effect of fluid pressure, temperature, and fluid velocity distributions around the blade. In their result, the maximum equivalent stress was shown in the blade near the hub and the tip position of the blade which had the largest stress. We recommend using the simulation tool to determine the possible stresses caused by hydrodynamics on our design. These results will be used to improve the structural design, increase the motor torque, decrease the deformation before hardware manufacture.

REFERENCES

1. Adam Stager. 2019. Robots on the farm | UDaily. https://www.udel.edu/udaily/2019/february/robots-agriculture-monitor-plants-roots-growth/ 1 August 2021.
2. Aggressive hydraulics & fluidpower. 2021. Fluid Power Journal June 2021 by Innovative Designs & Publishing, Inc. - Issuu. : 1–60. www.Aggressive hydraulics.com 28 July 2021.
3. Airline. 2019. Airline Hydraulics | Products and Solutions to Power Your Ideas. https://www.airlinehyd.com/pages/industries/mining-and-driller#tab-1 1 August 2021.
4. Andy Arendt. 2020. Amsoil, Hydraulic Power: Common Problems and Solutions – AMSOIL Blog. : 1–1. https://blog.amsoil.com/hydraulic-power-common-problems-and-solutions/#:~:text=Telltale signs of hydraulic problems,most expensive component to replace. 28 July 2021.
5. Arcangeletti, G., Mattioli, M., Ausborn, M., Matskevitch, D. & Marcotulli, A. 2021. Autonomous Subsea Field Development - Value Proposition, Technology Needs and Gaps for Future Advancement. *Day 3 Wed, August 18, 2021*: 1–1. https://onepetro.org/OTCONF/proceedings/21OTC/3-21OTC/D031S031R003/466758 16 August 2021.
6. De Beer Group. 2017. De Beers Group. : 1–8. https://www.debeersgroup.com/ 28 July 2021.
7. Bhaskar, P. & Sudheer, L. 2012. Design & Development of Real Time MATLAB-GUI Based Fuzzy Logic Controllers for DC Motor Speed Control System. *semantic scholar* : 1–3. https://www.semanticscholar.org/paper/Design-%26-Development-of-Real-Time-MATLAB-GUI-Based-Bhaskar-Sudheer/d652d7cfe6f1f69fb3b5d168036d96feb122bf71#references 6 September 2021.
8. Van Bloois, Willem, J. & Frumau, J. 2009. SS. Ocean Mining: Deep Sea Mining: A New Horizon for Dredging Technology. *OTC Offshore Technology Conference*: 1–1. https://onepetro.org/OTCONF/proceedings-abstract/09OTC/All-09OTC/OTC-20047-MS/35927 15 August 2021.
9. Cervantes, A., Garcia, P., Herrera, C., Morales, E., Tarriba, F., Tena, E. & Ponce, H. 2018. A Conceptual Design of a Firefighter Drone. *2018 15th International Conference on Electrical Engineering, Computing Science and Automatic Control, CCE 2018*. https://www.researchgate.net/publication/329116722_A_Conceptual_Design_of_a_Firefighter_Drone 29 July 2021.
10. Christensen, L., Fritsche, M., Albiez, J. & Kirchner, F. 2010. USBL pose estimation using multiple responders. *OCEANS'10 IEEE Sydney, OCEANSSYD 2010*, (May 2014): 1–10. https://www.researchgate.net/figure/Scaled-multipurpose-sub-sea-working-unit-of-the-project-ISUP-founded-by-the-German_fig1_236847585.
11. Chutia, S., Kakoty, N.M. & Deka, D. 2017. A review of underwater robotics, navigation, sensing techniques and applications. *ACM International Conference Proceeding Series*, Part F132085: 1–6. https://www.researchgate.net/publication/321237107_A_Review_of_Underwater_Robotics_Navigation_Sensing_Techniques_and_Applications 30 July 2021.
12. Ciszewski, M., Buratowski, T., Giergiel, M., Małka, P. & Kurc, K. 2014. Virtual prototyping, design and analysis of an in-pipe inspection mobile robot. *Journal of Theoretical and Applied Mechanics (Poland)*, 52(2): 417–429. https://www.researchgate.net/publication/269108982_Virtual_prototyping_design_and_analysis_of_an_in-pipe_inspection_mobile_robot.
13. CNN Correspondent Mary. 2010. *Blowout preventer control leaked hydraulic fluid, BP executive says - CNN.com*. http://edition.cnn.com/2010/US/07/20/gulf.oil.investigation/index.html 1 August 2021.
14. Corinna Kanzog. 2015. (PDF) ROBEX - Robotic Exploration of Extreme Environment and

Unmanned System Technology. *ResearchGate Journal of Unmanned System Technology*: 1–6. https://www.researchgate.net/publication/284022266_ROBEX_-_Robotic_Exploration_of_Extreme_Environment 30 July 2021.
15. CPV Manufacturing. 2015. How Does a Hydraulic System Work? O-Seal Trusted by the Navy | CPV. https://www.cpvmfg.com/news/how-does-a-hydraulic-system-work/ 28 July 2021.
16. Crawler, M. & seascape BV. 2017. Seascape developed a small electrical mini-crawler for subsea survey, inspection and cleaning. : 1. https://www.seascapesubsea.com/downloads/Seascape-Mini-crawler-R1.1.pdf 25 August 2021.
17. Cuyvers, L., Berry, W., Kristina, G., Torsten, T. & Caroline, W. 2018. *Deep seabed mining: a rising environmental challenge*.
18. Daanen, H. 2017a. *Mobility of Subsea Tracked Equipment*. delf. http://repository.tudelft.nl/.
19. Daanen, H. 2017b. Mobility of Subsea Tracked Equipment. : 1–63. Expected progress rates of the vehicle are to be determined to make a more realistic assessment%0Aof the expected project durations in the pre-execution stages . This can only be done if specific knowledge regarding the interaction between seabed soils an.
20. Dai, Y., Yin, W. & Ma, F. 2019. Nonlinear Multi-Body Dynamic Modeling and Coordinated Motion Control Simulation of Deep-Sea Mining System. *IEEE Access*, 7: 86242–86251. https://www.researchgate.net/publication/334102401_Nonlinear_Multi-Body_Dynamic_Modeling_and_Coordinated_Motion_Control_Simulation_of_Deep-Sea_Mining_System.
21. Deepak, B.B.V.L., Bahubalendruni, M.V.A.R. & Biswal, B.B. 2016. Development of in-pipe robots for inspection and cleaning tasks Survey, classification and comparison. : 1–29. www.emeraldinsight.com/2049-6427.htm 29 July 2021.
22. Djordje Vukcevic, Paul Gerhard Plöger & Sven Schneider. 2018. *(PDF) Extending a constrained hybrid dynamics solver for energy-optimal robot motions in the presence of static friction*. https://www.researchgate.net/publication/325405313_Extending_a_constrained_hybrid_dynamics_solver_for_energy-optimal_robot_motions_in_the_presence_of_static_friction.
23. Dr Thomas Peacock. 2015. Plume modelling … can be used to help drive the design of a collector vehicle and Minerals in Depth - This is the Story of Seabed Minerals. : 5–5. https://mineralsindepth.org/?gclid=CjwKCAjwzruGBhBAEiwAUqMR8OXLJ5-z5F_NMKfncdhq6saqsT_Ughq2WX_q9snbM44nQFHsVkb0vhoCJHkQAvD_BwE#page-top 29 July 2021.
24. Ehsan, M., Rampen, W.H.S. & Salter, S.H. 2000. Modeling of Digital-Displacement Pump-Motors and Their Application as Hydraulic Drives for Nonuniform Loads. *Journal of Dynamic Systems, Measurement, and Control*, 122(1): 210–215. https://asmedigitalcollection.asme.org/dynamicsystems/article-abstract/122/1/210/460194/Modeling-of-Digital-Displacement-Pump-Motors-and 6 September 2021.
25. Erin Sparks, Pete Moore, Burt Tanner, Adam Stager, Teclemariam Weldekidan & Randy Wisser. 2019. Robots on the farm | UDaily. https://www.udel.edu/udaily/2019/february/robots-agriculture-monitor-plants-roots-growth/ 1 August 2021.
26. Fedderke, J. & Pirouz, F. 2002. The Role of Mining in the South African Economy. *Agrekon*, 2(4): 5–34. https://www.researchgate.net/publication/334794446_The_role_of_mining_in_the_South_African_economy.
27. Feng, H., Du, Q., Huang, Y. & Chi, Y. 2017. Modelling study on stiffness characteristics of hydraulic cylinder under multi-factors. *Strojniski Vestnik/Journal of Mechanical Engineering*, 63(7–8): 447–456. https://web.a.ebscohost.com/ehost/detail/detail?vid=0&sid=1a6040ac-43f9-4ecf-a118-60d9bf03167f@sdc-v-sessmgr03&bdata=JnNpdGU9ZWhvc3QtbGl2ZQ==#AN=124307718&db=aph 6 September 2021.

28. FlowFit. 2019. What Are The Benefits Of A Hydraulic Tank | Hydraulic Components | Flowfit. : 31–36. https://www.flowfitonline.com/blog/hydraulic-components/what-are-the-benefits-of-a-hydraulic-tank 29 July 2021.
29. Fluids, H. 2017. Hydraulic fluids 1 1. *PUBLIC HEALTH STATEMENT*: 1–8. https://www.atsdr.cdc.gov/ToxProfiles/tp99-c1.pdf.
30. Gafurov, S.A. & Klochkov, E. V. 2015. Autonomous Unmanned Underwater Vehicles Development Tendencies. *Procedia Engineering*, 106: 141–148. www.sciencedirect.com 1 August 2021.
31. Grandgirard, J., Poinsot, D., Krespi, L., Nénon, J.P. & Cortesero, A.M. 2014. Costs of secondary parasitism in the facultative hyperparasitoid Pachycrepoideus dubius: Does host size matter? *Entomologia Experimentalis et Applicata*, 103(3): 239–248.
32. Haga, M., Hiroshi, W. & Fujishima, K. 2001. Digging control system for hydraulic excavator. *Mechatronics*, 11(6): 665–676. https://www.sciencedirect.com/science/article/pii/S095741580000043X.
33. Hanafi, D., Qetkeaw, M., Ghazali, R., Than, M.N.M., Utomo, W.M. & Omar, R. 2013. Simple GUI Wireless Controller of Quadcopter. *International Journal of Communications, Network and System Sciences*, 06(01): 52–59. https://www.scirp.org/pdf/IJCNS_2013012916540708.pdf.
34. Hose assembly tips. 2019. Where is a hydraulic hose used? - Hose Assembly Tips. : 1–1. https://www.hoseassemblytips.com/hydraulic-hose-used/ 12 September 2021.
35. Hou, L., Zhou, F., Kim, K. & Zhang, L. 2021. Practical model for energy consumption analysis of omnidirectional mobile robot. *Sensors*, 21(5): 1–18.
36. Hu, W. & Meng, Z. 2020. Study on Design of Working Device and Hydraulic System of Hydraulic Excavator Based on Computer Aided Technology. *Journal of Physics: Conference Series*, 1574: 1–7. https://iopscience.iop.org/article/10.1088/1742-6596/1574/1/012028/pdf 21 August 2021.
37. Hunter & Richard Joseph. 2007. Investigation of the application of mechanical mining of ocean floor polymetallic sulphide deposits. : 1–154. https://open.library.ubc.ca/soa/cIRcle/collections/ubctheses/24/items/1.0067064 24 August 2021.
38. Hyvärinen, J., Karlsson, M. & Zhou, L. 2020. Study of concept for hydraulic hose dynamics investigations to enable understanding of the hose fluid–structure interaction behavior. *Advances in Mechanical Engineering*, 12(4): 1–18. https://journals.sagepub.com/doi/pdf/10.1177/1687814020916110.
39. IMDH Group. 2016. Team | IMDH Group International Mining & Dredging Holding Ltd. : 1–3. https://www.imdhgroup.com/team.php 28 July 2021.
40. Jia, Y.Z., Li, J.S., Guo, N., Jia, Q.S., Du, B.F. & Chen, C.Y. 2019. Design and Research of Small Crawler Fire Fighting Robot. *Proceedings 2018 Chinese Automation Congress, CAC 2018*: 1. https://ieeexplore.ieee.org/document/8623538 29 July 2021.
41. john E. Flise. 1985. Ocean mining-1985. *IEEE Xplore Full-Text PDF:*: 1–3. https://ieeexplore.ieee.org/stamp/stamp.jsp?tp=&arnumber=1160278 14 August 2021.
42. Khan A. Arbab, Shayinda Khan, Zadan Khan & Syed Adil Mizan. 2015. (PDF) Marine Mineral Resources: A Newfangled Treasure to Explore. *Research Journal of Marine Sciences ISSN 2321–1296*, 3(2): 1–5. https://www.researchgate.net/publication/320147128_Marine_Mineral_Resources_A_Newfangled_Treasure_to_Explore 14 August 2021.
43. Kim, B.C., Lee, D.H. & Ahn, J.W. 2005. Performance of SR drive for hydraulic pump. *ICEMS 2005: Proceedings of the Eighth International Conference on Electrical Machines and Systems*, 1: 659–663. https://ieeexplore.ieee.org/stamp/stamp.jsp?tp=&arnumber=1574846.
44. Kim, K.Y., Jang, D.S., Cho, Y.L. & Jang, J.H. 2009. Development of electro-hydraulic control valve for intelligent excavator. *ICCAS-SICE 2009 - ICROS-SICE International Joint Conference 2009, Proceedings*: 2212–2216. https://ieeexplore.ieee.org/stamp/stamp.jsp?tp=&arnumber=5335261.

45. Lee, Y.H. & Kim, H.S. 2014. Digital Controller Design to Control the Direct Current Motor System. *International Journal of Control and Automation*, 7(9): 283–288. http://article.nadiapub.com/IJCA/vol7_no9/24.pdf.
46. Li, Y., Zhang, H., Wang, H., Li, J., Zhai, X. & Xu, J. 2019. Design of a Variable Buoyancy System for the Hybrid Crawler-Flyer Underwater Vehicle. *Proceedings - 2019 Chinese Automation Congress, CAC 2019*: 5335–5339. https://ieeexplore.ieee.org/stamp/stamp.jsp?tp=&arnumber=8997045&tag=1.
47. Lloyd-Smith, M. & Immig BAppSc, J. 2018. OCEAN POLLUTANTS GUIDE TOXIC THREATS TO HUMAN HEALTH AND MARINE LIFE PREPARED BY. *The National Toxics Network (NTN)*: 1–108. www.ipen.org 31 July 2021.
48. Lozano, C. & Dutra, M. 2014. ROV Design for Pluvial Applications. *Ciencia y tecnología de buques*, 8(15): 69.
49. Lumen physics. 2021. Bernoulli's Equation | Physics. : 1–1. https://courses.lumenlearning.com/physics/chapter/12-2-bernoullis-equation/ 1 August 2021.
50. Manager, P. & Ç Yavuz, A. 2009. *KINEMATIC ANALYSIS FOR ROBOT ARM*. file:///D:/my masters papers for research/KINEMATICANALYSISFORROBOTARMThesis.pdf.
51. mathworks. 2021. Modeling Inverse Kinematics in a Robotic Arm - MATLAB & Simulink. https://www.mathworks.com/help/fuzzy/modeling-inverse-kinematics-in-a-robotic-arm.html 31 July 2021.
52. Medagedara, N.T. & Chandra, P.D.S. 2012. Study on FEM and theoretically predicted Hysterisis loops. , 01(06): 1–9. https://www.researchgate.net/publication/313504104_Comparing_the_theoretical_and_Finite_Element_stress-strain_analysis_for_axial_and_torsion_loading.
53. Minerals and Energy Laws Amendment Act, N. 11 of 2005. 2013. MINERAL AND PETROLEUM RESOURCES DEVELOPMENT ACT NO. 28 OF 2002. : 1–69. https://cer.org.za/wp-content/uploads/2013/09/MPRDA-as-amended.pdf 28 July 2021.
54. Mooney, J.G. & Johnson, E.N. 2014. A Comparison of Automatic Nap-of-the-earth Guidance Strategies for Helicopters. *Journal of Field Robotics*, 33(1): 1–17. http://onlinelibrary.wiley.com/doi/10.1002/rob.21514/abstract.
55. Naidoo, R.N. 2013. Global Health Action Mining: South Africa's legacy and burden in the context of occupational respiratory diseases. *Global Health Action*: 1–4. http://dx.doi.org/10.3402/gha.v6i0.20512 14 August 2021.
56. Nazaruddin Nazaruddin & Gunawan. 2015. (PDF) Undercarriage Design of Excavator Model in Application of Various Track Drive. *Researchgate*: 1–7. https://www.researchgate.net/publication/320557845_Undercarriage_Design_of_Excavator_Model_in_Application_of_Various_Track_Drive 30 July 2021.
57. Pawlus, W., Choux, M. & Hansen, M.R. 2016. Hydraulic vs. electric: A review of actuation systems in offshore drilling equipment. *Modeling, Identification and Control*, 37(1): 1–17. researchgate.net/publication/301331439_Hydraulic_vs_Electric_A_Review_of_Actuation_Systems_in_Offshore_Drilling_Equipment 28 July 2021.
58. Poomphochana, K., Pratumsuwan, P. & Po-ngaen, W. 2013. Energy Saving in Electro-Hydraulic System Using Impedance Sensing. *Proceedings of the 3rd International Conference on Electric and Electronics*, 69: 1–5. https://www.researchgate.net/publication/266643730_Energy_Saving_in_Electro-Hydraulic_System_Using_Impedance_Sensing 29 July 2021.
59. Pro-hydrp, omport export. 2016. Hydraulic Cylinders | Johannesburg | South Africa - Pro Hyd. *Pro-Hyd Import & Export (Pty) Ltd*: 1–1. https://www.pro-hyd.co.za/hydraulic-cylinders.php 7 September 2021.
60. probably interactive. 2019. How Does A Vacuum Cleaner Work: Guide & Tips. : 1–1. https://probablyinteractive.com/vacuum-cleaner/ 28 July 2021.
61. Rafiq, A.A., Yusuf, M. & Pujono. 2018. Implementation of Digital Image Processing Using NI

myRIO and Arduino Mega 2560 as Controller on Rover Bogie Robot. *Proceedings - 2018 International Conference on Applied Science and Technology, iCAST 2018*: 210–215.
62. Ray Bohacz & successful farming. 2019. Know the Difference Between Mechanical and Hydraulic Valve Lifters | Successful Farming. : 1–1. https://www.agriculture.com/machinery/repair-maintenance/know-the-difference-between-mechanical-and-hydraulic-valve-lifters 12 September 2021.
63. Roger Billingham & Department of Natural Resources, Q. 2004. MINERALS EXPLORATION safety guidance note. *Queensland Goverment natural resources and mine* : 1–74. https://www.resources.qld.gov.au/__data/assets/pdf_file/0005/240566/qld-guidance-note-exploration-safety.pdf 1 August 2021.
64. Roman Mikhailiuk, Kajornyotwildlifr & Drawii. 2021. The Causes And Effects Of Ocean Pollution - WorldAtlas. https://www.worldatlas.com/articles/what-causes-ocean-pollution.html 28 July 2021.
65. Sam, R., Arrifin, K. & Buniyamin, N. 2012. Simulation of pick and place robotics system using solidworks softmotion. *Proceedings of the 2012 International Conference on System Engineering and Technology, ICSET 2012*.
66. Schmidt, L., Groenkjaer, M., Pedersen, H.C. & Andersen, T.O. 2017. Position Control of an Over-Actuated Direct Hydraulic Cylinder Drive. *Control Engineering Practice*, 64(March): 1–14. http://dx.doi.org/10.1016/j.conengprac.2017.04.003.
67. Scott, S.D. 2011. Marine minerals: Their occurrences, exploration and exploitation: Introduction to session 6.8 marine resources. *OCEANS'11 - MTS/IEEE Kona, Program Book*.
68. Seabed dredger & seascape BV. 2017. Seascape developed the seabed dredger as a multipurpose bottom tracking vehicle with the main feature of deepwater dredging. : 1–1. https://www.seascapesubsea.com/downloads/Seascape-Seabed-dredger-R1.1.pdf 25 August 2021.
69. seabed dredging excavator & seascape technology BV. 2017. SBDE - Seabed dredger excavator. : 1–1. https://www.seascapesubsea.com/downloads/Seascape-Seabed-dredger-excavator-R1.3.pdf 26 August 2021.
70. seascape BV. 2017. Seabed dredger excavator seascape seabed technology BV technology. : 1–1. https://www.seascapesubsea.com/downloads/Seascape-Seabed-dredger-excavator-R1.3.pdf 29 July 2021.
71. Shaera training system. 2021. Hydraulic Systems. http://www.sphaera.co.uk/hydraulic.htm 1 August 2021.
72. Sousa, A., Madureira, L., Coelho, J., Pinto, J., Pereira, J., Sousa, J.B. & Dias, P. 2012. *LAUV: The man-portable autonomous underwater vehicle*. IFAC. http://dx.doi.org/10.3182/20120410-3-PT-4028.00045.
73. Srinivas, P. & Rao, P.D.P. 2012. Comparative Analysis of Conventional Pid Controller and Fuzzy Controller with various Defuzzification Methods in a Three Tank Level Control System. *International Journal of Information Technology, Control and Automation*, 2(4): 75–86. https://www.academia.edu/36678088/COMPARATIVE_ANALYSIS_OF_CONVENTIONAL_PID_CONTROLLER_AND_FUZZY_CONTROLLER_WITH_VARIOUS_DEFUZZIFICATION_METHODS_IN_A_THREE_TANK_LEVEL_CONTROL_SYSTEM.
74. Su, D.H. & Bao, G.W. 2012. Simulation Study of the Effect of Hydraulic Hose Parameters on Hydraulic Impact. *Applied Mechanics and Materials*, 184–185: 465–468. https://www.scientific.net/AMM.184-185.465 12 September 2021.
75. Suhas, Y. & Prof.S.S.Patil. 2014. ISSN: 2277-9655 Impact Factor: 1.852. *international journal of engineering science and reaserch technology*, 3(4): 6. https://d1wqtxts1xzle7.cloudfront.net/33659084/131.pdf?1399607829=&response-content-disposition=inline%3B+filename%3DFuzzy_PID_Controllers_Using_Matlab_GUI_B.pdf&Expires=1630792784&Signature=G1S7bPrWi1XuWeAU~vF40zok8AaeHTj6ojr13R1iOJEoP2ecs2ls9wpq~M07FVSp.

76. swire seabed. 2008. SEABED EXCAVATOR. : 1–2. www.swireseabed.com 24 August 2021.
77. Tae-Kyeong Yeu, Suk-Min Yoon, Chang-Ho Lee & Jong-Su Choi and Ki-Young Sung. IEEE Xplore Full-Text PDF: *MOERI/Korea Ocean Research & Development Institute*: 1–6. https://ieeexplore.ieee.org/stamp/stamp.jsp?arnumber=6107056 15 August 2021.
78. Tehrani, N.H., Heidari, M., Zakeri, Y. & Ghaisari, J. 2010. Development, depth control and stability analysis of an underwater Remotely Operated Vehicle (ROV). *2010 8th IEEE International Conference on Control and Automation, ICCA 2010*: 814–819. https://ieeexplore.ieee.org/stamp/stamp.jsp?tp=&arnumber=5524051.
79. Tič, V. & Lovrec, D. 2012. Design of modern hydraulic tank using fluid flow simulation. *International Journal of Simulation Modelling*, 11(2): 77–88. http://ijsimm.com/Full_Papers/Fulltext2012/text11-2_77-88.pdf.
80. TONDOLO, N.L. 2012. QUANTITATIVE INVESTIGATION OF HYDRAULIC EQUIPMENT FAILURES WITHIN THE ORIGINAL EQUIPMENT MANUFACTURER STANDARD. *creative common*: 1–75.
81. Toyin Akinosho & Africa oil +gas. 2020. Hydraulic Workover Rig Catches Fire on Ororo Well - Africa's premier report on the oil, gas and energy landscape. - Africa's premier report on the oil, gas and energy landscape. : 1–1. https://africaoilgasreport.com/2020/05/oil-patch-sub-sahara/hydraulic-workover-rig-catches-fire-on-ororo-well/ 29 July 2021.
82. Tuong, Q.V., Hyoung, S.K., Hyo, S.C., Doan, N.D. & Byung, R.L. 2009. A study on optimization of fish robot maximum velocity using the combination of genetic - Hill climbing algorithm. *ICCAS-SICE 2009 - ICROS-SICE International Joint Conference 2009, Proceedings*, (link 3): 2280–2285.
83. Tveitnes, T., Fairlie-Clarke, A.C. & Varyani, K. 2008. An experimental investigation into the constant velocity water entry of wedge-shaped sections. *Ocean Engineering*, 35(14–15): 1463–1478.
84. Upalanchiwar, T. & Sakhare, P.A. V. 2014. Design and implementation of the fuzzy PID controller using MATLAB / SIMULINK model. *International Journal of Research in Computer and Communication Technology*, 3(3): 369–372. https://nanopdf.com/download/design-and-implementation-of-the-fuzzy-pid-controller-using_pdf.
85. Urrea, C. & Saa, D. 2020. Design and implementation of a graphic simulator for calculating the inverse kinematics of a redundant planar manipulator robot. *Applied Sciences (Switzerland)*, 10(19): 1–18. https://www.researchgate.net/publication/344398856_Design_and_Implementation_of_a_Graphic_Simulator_for_Calculating_the_Inverse_Kinematics_of_a_Redundant_Planar_Manipulator_Robot 31 July 2021.
86. Venter, J. & Sabunet. 2017. Hydraulic valve lifters. *jake venter*, (January): 2017. https://journals.co.za/doi/abs/10.10520/EJC-4d0eea0c7.
87. Vijay, S. & Site, D.M./ P.-B. 2019. Hydraulic Gagging of the Hydro-Electric Safety Valve (Make : Sempell GmbH) for Valve Closure during Hydro Test in RH Circuit Hydraulic Gagging of the Hydro-Electric Safety Valve (Make : Sempell GmbH) for Valve Closure during Air Tightness Test and Hyd. *ResearchGate*, (April): 1–10. https://www.researchgate.net/publication/332383341_Hydraulic_Gagging_of_the_Hydro-Electric_Safety_Valve_Make_Sempell_GmbH_for_Valve_Closure_during_Hydro_Test_in_RH_Circuit.
88. Woma karcher Group. 2015. HigH pressure water jetting in tHe oil and gas industry. : 1–20. https://s3.kaercher-media.com/asset/12990/1453665724/brochurewomagas.pdf 29 July 2021.
89. Wood, S., Harris, W., Ismail, T., Malone, J.M., Nanney, M., Ojeda, J., Pugatch, B. & Vandedrinck, S. 2013. Hybrid robot crawler / flyer for use in underwater archaeology. *OCEANS 2013 MTS/IEEE - San Diego: An Ocean in Common*: 1–11. https://ieeexplore.ieee.org/stamp/stamp.jsp?tp=&arnumber=6741185&tag=1.
90. Yang, C., Huang, K., Li, Y., Wang, J. & Zhou, M. 2012. Review for Development of Hydraulic

Excavator Attachment. *Energy Science and Technology*, 3(2): 93–97. https://core.ac.uk/download/pdf/236300336.pdf.
91. Yi-Cun, N. 2020. Development of High Pressure and Constant Low Flow Test System for Hydraulic Support Safety Valve. *IOP Conference Series: Earth and Environmental Science*, 610(1): 1–9. https://iopscience.iop.org/article/10.1088/1755-1315/610/1/012014/pdf.
92. Yoon, S.-M., Hong, S., Park, S.-J., Choi, J.-S., Kim, H.-W. & Yeu, T.-K. 2012. Track velocity control of crawler type underwater mining robot through shallow-water test †. *Journal of Mechanical Science and Technology*, 26(10): 3291–3298. www.springerlink.com/content/1738-494x 15 August 2021.
93. Yu, K., Yan, P. & Hu, J. 2020. Numerical Analysis of Blade Stress of Marine Propellers. *Journal of Marine Science and Application*, 19(3): 436–443.
94. Zhao, X., Zhang, S., Zhou, C., Hu, Z., Li, R. & Jiang, J. 2015. Experimental study of hydraulic cylinder leakage and fault feature extraction based on wavelet packet analysis. *Computers and Fluids*, 106: 33–40. http://dx.doi.org/10.1016/j.compfluid.2014.09.034.
95. Zhong, J., Zhang, S.Y., Wang, X.M., Yusheng, Z., Qun, X., Wescott, T., Vaishnav, S., Khan, Z., Upalanchiwar, T., Sakhare, P. a V, Tomizuka, M., Isaka, S., Teknologi, J., Shakya, R., Rajanwal, K., Patel, S., Dinkar, S., Santos, M., Dormido, S., Cruz, J.M. De, Sanchez, E., Becerra, H., Vélez, C., Proportional-integral-derivative, I.I., Preeti, D., Beniwal, N., Kumar, V., Rana, K.P.S., Gupta, V., Krass, M., Khalifah, A., Kaur, A., Farouk, N., Chopra, V., Singla, S.K. & Dewan, L. 2014. Design and Simulation of PD , PID and Fuzzy Logic Controller for Industrial Application. *IEEE Transactions on Systems, Man, and Cybernetics*, 3(8): 1–5. http://team358.org/files/programming/PIDControlTheory_rev3.pdf%5Cnhttp://www.ijsrp.org/research-paper-0812/ijsrp-p0863.pdf%5Cnhttp://ieeexplore.ieee.org/xpls/abs_all.jsp?arnumber=1548540%5Cnhttp://ieeexplore.ieee.org/lpdocs/epic03/wrapper.htm?arnumber=260.
96. Zhu, D., Fu, Y., Han, X. & Li, Z. 2020. Design and experimental verification on characteristics of electro-hydraulic pump. *Mechanical Systems and Signal Processing*, 144: 106771. https://doi.org/10.1016/j.ymssp.2020.106771.
97. Wood, S., Harris, W., Ismail, T., Malone, J.M., Nanney, M., Ojeda, J., Pugatch, B. & Vandedrinck, S. 2013. Hybrid robot crawler / flyer for use in underwater archaeology. *OCEANS 2013 MTS/IEEE - San Diego: An Ocean in Common*: 1–11.

APPENDICES

APPENDIX A: LabVIEW program for the dynamic drive system (motor controllers), arm control, pump control (servo motor controllers), live camera display, lighting switch, and User Interface (UI).

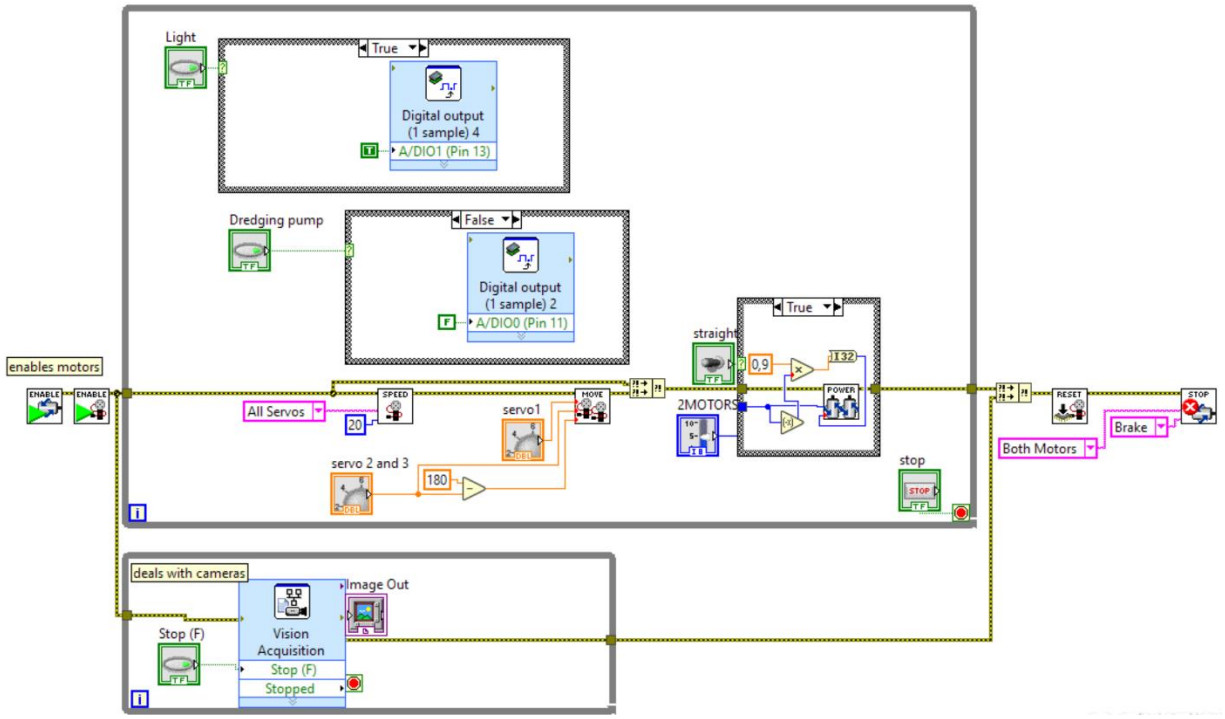

APPENDIX B:

Using python to plot graphs showing the angles of inclination.

```
# graph of Maximum velocity versus different angles of elevation
import matplotlib.pyplot as plt
import numpy as np
fig = plt.figure(figsize=(6,6))

ax = fig.add_subplot(autoscale_on=False, xlim=(-10, 50), ylim=(0.1, 0.4))
ax.grid(True)
# values
x = [0, 15, 20, 25, 30]
y = [0.305, 0.256, 0.250, 0.211, 0.181]
# polyfit
p = np.poly1d(np.polyfit(x, y, 2))
print(np.polyfit(x, y, 2))
t = np.linspace(0, 30, 250)
# title of graph
ax.set_title("maximum velocity versus different angles of inclination")
ax.set_xlabel('angles of elevation (in degrees)')
```

```
ax.set_ylabel('maximum velocity (m/s)')
ax.plot(x, y, 'o', t, p(t), '-')
plt.show()

# graph of Torque versus maximum velocity at 0 angle of inclination
import matplotlib.pyplot as plt
import numpy as np
fig = plt.figure(figsize=(6,6))
ax = fig.add_subplot(autoscale_on=False, xlim=(-0.1, 0.4), ylim=(10, 110))
ax.grid(True)
# values


x = [0, 0.07, 0.15, 0.227, 0.300]
y = [20, 40, 60, 80, 100]
# polyfit
p = np.poly1d(np.polyfit(x, y, 2))
print(np.polyfit(x, y, 2))
t = np.linspace(0, 0.3, 250)
# title of graph
ax.set_title("torque versus maximum velocity at $0^{o}$ angle of inclination")
ax.set_xlabel('maximum velocity (m/s)')
ax.set_ylabel('torque (%)')
ax.plot(x, y, 'o', t, p(t), '-')
plt.show()

# graph of Torque verses maximum velocity at 〖20〗^0 angle of inclination.
import matplotlib.pyplot as plt
import numpy as np
fig = plt.figure(figsize=(6,6))
ax = fig.add_subplot(autoscale_on=False, xlim=(-0.1, 0.4), ylim=(10, 110))
ax.grid(True)
# values

x = [0, 0.043, 0.114, 0.181, 0.257]
y = [20, 40, 60, 80, 100]
# polyfit
p = np.poly1d(np.polyfit(x, y, 2))
print(np.polyfit(x, y, 2))
t = np.linspace(0, 0.257, 250)
# title of graph
ax.set_title("torque versus maximum velocity at $20^{o}$ angle of inclination")
ax.set_xlabel('maximum velocity (m/s)')
ax.set_ylabel('torque (%)')
ax.plot(x, y, 'o', t, p(t), '-')
plt.show()

# graph of minimum Torque versus different angle of inclination.
import matplotlib.pyplot as plt
import numpy as np
fig = plt.figure(figsize=(6,6))
ax = fig.add_subplot(autoscale_on=False, xlim=(-1, 31), ylim=(25, 40))
```

```
ax.grid(True)
# values

x = [0, 15, 20, 25, 30]
y = [30.0, 32.6, 34.3, 35.6, 37.3]
# polyfit
p = np.poly1d(np.polyfit(x, y, 2))
print(np.polyfit(x, y, 2))
t = np.linspace(0, 30, 250)
# title of graph
ax.set_title("minimum torque versus different angle of inclination")
ax.set_xlabel('angle of inclination in degrees')
ax.set_ylabel('minimum Torque (%)')
ax.plot(x, y, 'o', t, p(t), '-')
plt.show()

# graph of efficiency vs torque at 0 and 20 degrees angle of inclination.
import matplotlib.pyplot as plt
import numpy as np
fig = plt.figure(figsize=(6,6))
ax = fig.add_subplot(autoscale_on=False, xlim=(-1, 110), ylim=(-0.1, 0.3))
ax.grid(True)
# values

x = [20, 40, 60, 80, 100]
y = [0, 0.138, 0.197, 0.224, 0.237]
y2 = [0, 0.085, 0.150, 0.179, 0.203]
# polyfit
p = np.poly1d(np.polyfit(x, y, 2))
print("first formula", np.polyfit(x, y, 2))
t = np.linspace(20, 100, 250)

p2 = np.poly1d(np.polyfit(x, y2, 2))
print("second formula", np.polyfit(x, y2, 2))
t2 = np.linspace(20, 100, 250)
# title of graph
ax.set_title("graph of efficiency versus torque at $0^{o}$ and $20^{o}$ degrees angle of inclination")
ax.set_xlabel('Torque (%)')
ax.set_ylabel('Efficiency (%)')
ax.plot(x, y, 'o', t, p(t), '-',  label='$0^{o}$')
ax.plot(x, y2, 'o', t2, p2(t2), '-', label='$20^{o}$')
ax.legend(loc='upper left')
plt.show()
```